UNIVERSITY OF LIVERPOOL

Department of Electrical Engineering and Electronics

Plasma Diagnostic Study of Bipolar HiPIMS Discharges

Thesis submitted in accordance with the requirements of the University of Liverpool for the degree of Doctor in Philosophy by

Marcus Andrew Law

March, 2023

Abstract

Bipolar high power impulse magnetron sputtering (bipolar HiPIMS) is a relatively new technique used in magnetron sputtering devices, where a positive voltage pulse is applied to the to the target shortly after termination of the main negative pulse. Using this technique, ion energies incident on a substrate can be controlled without the need for substrate biasing. In this research, a temporal diagnostic study of bipolar HiPIMS discharges was performed using a circular planar unbalanced magnetron with tungsten target operating in argon. Incoherent laser Thomson scattering (LTS) was used to measure the electron temperature T_e and density n_e. An emissive probe measured the plasma potential V_p. Optical emission spectroscopy (OES) and 2D broadband imaging captured the optical emission of plasma species.

The study revealed that reverse discharges with similarities to plasma fireballs formed during the positive pulse and were excited for positive pulse voltages V_{pp} ranging from 20 to 340 V. They sat primarily on the discharge centre-line and their establishment was delayed relative to the initiation of the positive pulse, with the delay time shortening with increased V_{pp}. Dramatic electron heating (T_e rises from < 1 up to 3 eV) both on the discharge centre line and above the racetrack was found during the fireball event, with greatly reduced election densities (by a factor of 5) in the magnetic trap compared to the unipolar pulse case. A reappearance of argon line intensities was measured, which followed the profile of the elevated T_e. Emission lines of tungsten in the discharge were also found which were not present in the unipolar afterglow, but their intensities diminished during the pulse duration. The measured V_p was raised rapidly at all positions along the centre line and above the racetrack, closely matching the applied V_{pp} throughout the positive pulse.

The phenomena of plasma electron heating, intense light emission and wall sputtering in the positive pulse is discussed. This is done in terms of the existence of a reverse (fireball-like) discharge, in which the vessel walls become an effective cathode, providing a source of energetic secondary electrons. These electrons are accelerated through the wall sheath potential into the bulk plasma, with magnetic field lines guiding their path. For high V_{pp} magnitudes, re-sputtering of deposited materials from the grounded vessel walls may provide an additional source of metal species in the deposition process. The existence of such anodic fireballs is a possible unwanted effect in bipolar HiPIMS.

Publications and Conferences

The research presented in this thesis, completed throughout the time as a PhD student has thus far, led to the following peer-reviewed publications:

1. **M. A. Law**, F. Lockwood Estrin, M. D. Bowden, and J. W. Bradley, "Diagnosing asymmetric bipolar HiPIMS discharges using laser thomson scattering," Plasma Sources Science and Technology, vol. 30, no. 10, p. 105019, 2021. [1]

2. **M. A. Law**, F. Lockwood Estrin, P. M. Bryant, M. D. Bowden, and J. W. Bradley, "Evidence for fireballs in bipolar HiPIMS plasmas," Plasma Sources Science and Technology, vol. 32, no. 2, p. 025015, 2023. [2]

The research has also been presented at multiple conferences in both poster and oral form:

1. **M. A. Law**, M. D. Bowden, and J. W. Bradley. Time resolved electron properties measured by laser Thomson scattering in a HiPIMS plasma. 17^{th} Technological Plasma Workshop, Ricoh Arena, Coventry, UK, October 2019. **Poster**.

2. **M. A. Law**, M. D. Bowden, and J. W. Bradley. Electron property measurements in a Bipolar HiPIMS discharge by laser Thomson scattering. Eleventh International Conference on Fundamentals and Industrial Applications of HIPIMS (Virtual), June 2021. **Oral presentation**.

3. **M. A. Law**, M. D. Bowden, and J. W. Bradley. Racetrack electron property measurements in a Bipolar HiPIMS discharge by laser Thomson scattering. 48^{th} Annual Plasma Physics Conference, April 2022, Liverpool, UK. **Poster**.

4. **M. A. Law** and J. W. Bradley. Diagnosing Bipolar HiPIMS Plasmas Using Laser Thomson Scattering. 48^{th} International Conference on Metallurgical Coatings and Thin Films. San Diego, USA, May 2022. Invited virtual **Oral presentation**.

5. **M. A. Law**, M. D. Bowden, and J. W. Bradley. Electron heating during the positive pulse of a Bipolar HiPIMS discharge measured by laser Thomson scattering. 12^{th} International Conference on Fundamentals and Industrial Applications of HIPIMS, Sheffield, UK, June 2022. **Oral presentation**.

Acknowledgements

Firstly, I must thank my PhD supervisor, Professor James Bradley, and express my gratitude for his continual support, guidance, patience and wisdom throughout the progression of my PhD studies. I would like to thank ESPRC and the University of Liverpool for the funding provided to undertake this research project and, also to all staff and students who were involved in the Fusion CDT programme.

I would like to thank Mark Burnley for his technical assistance throughout the years, building the positive polarity pulsing unit (for the bipolar HiPIMS system) and most importantly for our chats in the corridor. Another thanks is to Gareth Blacoe for the hours spent deciphering and building equipment/parts for my experiments. I would like to show my appreciation to Dr Francis Lockwood Estrin for our combined work, using the emissive probe and for our many technical chats regarding plasma physics. Thanks to Dr Paul Bryant for the use of the iCCD camera and emissive probe circuitry. A massive thank you must be given to Dr Peter Ryan for his expertise and patience when I first started my PhD, and for his remaining friendship to this day.

I am very grateful for all the friends I have made during my time at the University of Liverpool that made my experience as a PhD student thoroughly enjoyable. The next person I must thank is my wonderful partner, Grace, who has provided continuous love and support through the highs and lows of my studies - I truly could not have done this without you. To all my friends and family back home, I must express my gratitude for all you have done for me throughout.

Contents

List of Figures

List of Tables

Chapter 1

Introduction

This thesis is focused on plasma property measurements in asymmetric bipolar HiPIMS discharges. Bipolar HiPIMS is a relatively new technique for deposition and thin film coatings, where a positive (reverse) voltage pulse is delivered to the target cathode, directly after the initial negative (HiPIMS) pulse. It has received great interest in the HiPIMS community due to it's capacity to tailor ion energies incident on a growing film. In this work, four diagnostic methods were used to measure different plasma properties and characteristics: Laser Thomson Scattering (LTS) was used to measure time-resolved electron density (n_e) and electron temperatures (T_e), Optical Emission Spectroscopy (OES) was used to to determine the temporal evolution of the important metal and gas species in the plasma, an Emisive Probe (EP) was used to track the spatial and temporal evolution of the plasma potential and finally, 2D broad band optical imaging was used to temporally image the plasma and it's evolution throughout the bipolar HiPIMS waveform. This chapter gives a brief introduction to plasmas, introduces sputtering devices and highlights the research aims and content of the thesis. It is organised as follows: (1) introduction to plasmas and plasma definition, (2) introduction to gas discharge plasmas and DC glow discharge sputtering, (3) the importance of free electrons in a plasma and why electron property measurements are essential in characterising plasma discharges, (4) details the scope of this thesis, introducing the research topics and aims of the study, (5) the content of subsequent thesis chapters are outlined.

1.1 Plasma

Plasma is often referred to as the fourth state of matter, in which enough energy has been provided to a gas, to release electrons from atoms, leaving a mixture of ions, neutrals and free electrons. In 1928, Langmuir [3] first used the word plasma to describe an ionised gas with balanced ion and electron densities. The approximate equivalency in the number of positive and negative charge carriers in a plasma is referred to as quasineutrality, whereby a plasma maintains equal numbers of oppositely charged particles, remaining in an overall net neutral charge. Plasmas are the predominant contributor to the observable matter in the universe, commonly stated to make up approximately 99% of what we see and can interact with. Naturally occurring examples of plasmas include; stars, the Aurora Borealis (northern lights) and lightening bolts. Terrestrial, man made plasmas include everyday items such as fluorescent lamps and plasma display panels, and are used today in industrial and scientific settings with applications in the medical sector, space exploration, semiconductor industry and in energy production, in the case of nuclear fusion devices, such as the tokamak.

Plasmas can be defined separately from a gas (and weakly ionised gases) due to the fact that they exhibit collective behaviour, where long range electromagnetic forces dominate over the gaseous processes. Plasmas are able to screen a perturbation of charge in it's volume such that it is overall neutral, reducing the length of induced electric fields. If one considers a plasma consisting of (positive) ions, electrons and neutrals in contact with a surface, for example a plasma created in a vacuum vessel, a plasma "sheath" forms at the boundaries. Initially, due to the high mobility of electrons (compared to the heavier ions) the walls charge negatively due to the flux of the electrons. This leaves behind a net positive charge, and an electric field between the bulk and the vessel walls forms, accelerating ions towards the wall and repelling electrons away. This results in a space-charge layer around the walls, known as the sheath, with predominant ion concentration, shielding the potential at the wall from the bulk plasma. The bulk plasma is then situated slightly positive relative to the walls, at the plasma potential, V_p.

The length scale in which charge perturbations are screened is characterised by the Debye length (λ_D). This gives rise to the aforementioned term; quasi-neutral, where quasi comes from the Latin "as if", meaning that the plasma resembles a neutral form. Indeed, on length scales $\gg \lambda_D$, the ion and electron densities are close to equal and quasi-neutrality holds, however for length scales $\leqslant \lambda_D$, space-charge effects become significant. The Debye

length has the form:

$$\lambda_D = \sqrt{\frac{\epsilon_0 k_B T_e}{ne^2}} \tag{1.1}$$

which depends on the density (n) and electron temperature (T_e) of the plasma and is derived by solving Poisson's equation in one dimension [4, p. 9]. ϵ_0 is the permittivity of free space, k_B is the Boltzmann constant and e is the charge of an electron. Equation 1.1 is given in SI units with $k_B T_e$ given in joules however, in plasma physics, electron temperature is commonly stated in electron Volts (eV). The relation is:

$$T_e(eV) = \frac{k_B T_e(K)}{e} \tag{1.2}$$

The sheath region can be further separated in to two parts: the sheath and pre-sheath. In the sheath, quasineutrality fails due to the predominant ion concentration[1], with only a small number of high energy electrons able to overcome the potential barrier. In the pre-sheath, quasinuetrality roughly holds, but there exists a small electric field that must accelerate ions to a minimum of the Bohm velocity [4, p. 272], $V_B = \sqrt{\frac{k_B T_e}{M_i}}$, to enter the sheath. The combination of sheath and pre-sheath regions result in electron and ion currents to the wall equalising, with no net current flow out of the plasma.

Plasmas can be separated into thermal (hot) and non-thermal (cold). Thermal plasmas have electron and ion temperatures approximately equal ($T_e \approx T_i$), and usually have very high temperatures, as is often the case of fusion plasmas, where $T_e >$ keV. Non thermal plasmas (the case in this study), have electron temperatures $T_e \gg T_i$, with T_e of the order of several eV, where as the ions are situated close to room temperature. This type of plasma is said to be low temperature. One can further classify experimental laboratory or industrial plasmas into two further categories: low pressure (the case in this study) and atmospheric plasmas. Low pressure plasmas are created inside vacuum vessels, where the background air is evacuated and a backing gas is used to ignite the discharge. Atmospheric plasmas usually operate at $\sim 10^5$ Pa, with relatively simple set ups in comparison to low pressure experiments. Greater detail of atmospheric plasmas can be found in the review [5] but is beyond the scope of this thesis. The focus of the rest of the chapter will be on relevant low pressure, low temperature plasmas.

[1] Electron sheaths also exist if the plasma is in contact with a surface biased more positive than V_p

A final, summarising definition of a plasma, modified from the definition given by Chen [4] is:
"A plasma is an ionised gas which is quasi-neutral and displays collective behaviour."
Where:

- The dimensions of the plasma (L) is sufficiently larger than λ_D to ensure quasi-neutrality. $L \gg \lambda_D$ (where L is a characteristic length scale of the plasma)
- The plasma is sufficiently dense such that there are many charged particles, N_D, in a Debye sphere to shield the potential. $N_D = \frac{4\pi}{3} n_e \lambda_D^3 \gg 1$ [2](where n_e is the electron density)
- The frequency of long range, collective electromagnetic interactions dominate over the frequency of one-to-one collisional interactions of ions and neutrals such that the charged particles remain charged. $\frac{\omega_{collective}}{\omega_{collisions}} \gg 1$ (where ω represents the frequency and the subscript denotes the interaction)

1.2 Gas Discharge Plasmas

The review [6], details numerous gas discharge plasmas and their various applications. This section aims to discuss relevant low pressure electrical discharge systems. One common way of creating terrestrial plasmas is by applying an electric field to a gas or gas mixture until electrical breakdown occurs in the gas, creating a mixture of electrons, ions and neutrals. The way in which the power is delivered to the plasma can be placed into two distinct categories, where either a conduction or displacement current is driven in the discharge. The former utilises a DC or pulsed DC electric fields, where as the latter uses radio frequency, through inductive or capacitive coupling of the plasma to the electrodes. Typical low pressure discharges are considered to be non-thermal as the electrons have a much larger temperature compared to the ionic contributors. The electric field readily accelerates the lightweight electrons whilst the ions can be considered relatively immobile, making the electrons the dominant energy transfer species in the discharge.

A simple discharge to consider is one consisting of two electrodes with a DC potential across them - the DC diode discharge (figure 1.1 shows an example of this type of device

[2]This is often called the plasma parameter

- a glow discharge). With enough potential between the plates (in the range 2 - 5 kV for glow discharge regime [7, p. 23]), electrical breakdown can occur and current begins to conduct between the plates. Paschen's law [8] describes the relation between this breakdown voltage, the distance between the two plates and the pressure of the specific gas. A seed electron, usually created from cosmic ray photoionisation, starts off the process. This electron travels to the anode, undergoing collisions with the background gas, creating further free electrons, ions and excited gas/ion species. These highly mobile electrons undergo further collisions, ionising the background gas, producing an electron avalanche. The less mobile ions drift slowly towards the cathode and create a secondary source of electrons, released from the cathode surface, which again contribute to further impact ionisation events. The discharge will be self sustaining if there are enough secondary electrons created so further avalanches occur [9] (i.e one electron created in an ionisation event goes on to create at least one more ionisation event).

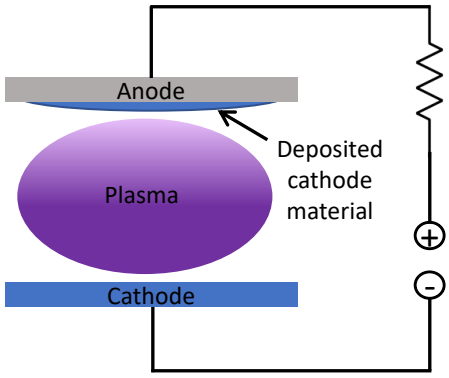

Figure 1.1: A schematic of a DC glow discharge used for sputtering. Here the cathode material is sputtered by energetic ions bombarding the cathode surface and condenses on the anode surface, as indicated by the blue film layer on the surface.

At a certain condition (current densities in the range 10^{-3} - 10^{-5} Acm^{-2} [10]), the configuration shown in figure 1.1 produces what is called a "glow discharge", named because of its characteristic glow, as excited species dexcite and release photons. Sheath regions form near the cathode and anode surfaces which accelerate ions and electrons across the space charge layers. The sheath near the cathode has the highest potential drop, accelerating ions towards the cathode and secondary electrons away. The acceleration of electrons

through the electric field provides them with enough energy to reach the bulk plasma, where they ionise the background gas and thermalise with the bulk electrons, increasing the plasma electron temperature. The formation of the cathode sheath with a strong electric field means that ions accelerated over this potential, incident on the cathode surface, expel cathode atoms in a process called sputtering [11].

This simple design produces a basic sputtering system where cathode atoms can be deposited onto surfaces. In the case in figure 1.1, the cathode will be eroded, with its material deposited on the anode and chamber walls. This type of sputtering device however, creates low density discharges and requires relatively high gas pressure (commonly stated to be between 2 - 4 Pa [7, p. 23]). The high pressure ensures enough collisions occur to self sustain the plasma before the energetic particles are lost to the walls/anode but results in low deposition rate [10]. The size of the cathode sheath, or "dark space" extends about 1 -2 cm in this regime and is typically larger than the ion mean free path of < 1 cm [12], resulting in a collisional sheath. The ions incident on the target/cathode surface, therefore exhibit a broad range of energies instead of falling through the full cathode potential. The plasma densities in these devices results in a low number of sputtering events and the relatively high pressures used to sustain the discharge cause frequent collisions between the sputtered material and background gas, lowering the sputtered atoms kinetic energy. This results in a poor quality of deposited coating.

It is therefore clear that modifications to this device that would allow operation at lower pressure and higher current densities are needed. A way to achieve this is to confine the electrons near the cathode using a magnetic field. This is the design principle of the magnetron, which uses permanent magnets, located behind the cathode surface (the device used in this work) and will be detailed further in section 2.1.2. The device is considered to be weakly magnetised, trapping the electrons close to the target, maintaining a region of dense plasma where many sputtering events occur. The heavier ions are not confined in this regime.

1.3 Free Electrons

As previously mentioned, electrons inside a plasma are much more mobile than the heavier ionic species due to their much lower mass. For a discharge created with an argon atmosphere (a typical inert gas used for industrial plasmas) the electrons are ~ 70000 times lighter. In a uniform electric field, the acceleration of charged particles scales inversely

with its mass and therefore, in a plasma created by an external electric field, the electrons will be more readily accelerated. This means that the kinetic energy gained by the electrons is much greater than the ions, making them the dominant energy dissipation and transfer mechanism inside the plasma, responsible for ionisation and excitation. Energy losses from the plasma are also governed by the electrons, as energetic particles are lost to the surfaces housing the plasma. Ionic losses to the walls of a vacuum vessel, arise from sheath acceleration, related to the electron temperature through the Bohm criteria. Electron losses to the wall arise from the high energy tail of the electron energy distribution function (EEDF), able to overcome the sheath potential and leave the plasma.

A group of electrons in thermodynamic equilibrium will have a three dimensional EEDF, following the Maxwellian energy distribution [10, p. 36], with the form:

$$f(E) = 2n_e \left(\frac{E}{\pi}\right)^{\frac{1}{2}} \left(\frac{1}{k_B T_e}\right)^{\frac{3}{2}} \exp\left(\frac{-E}{k_B T_e}\right), \tag{1.3}$$

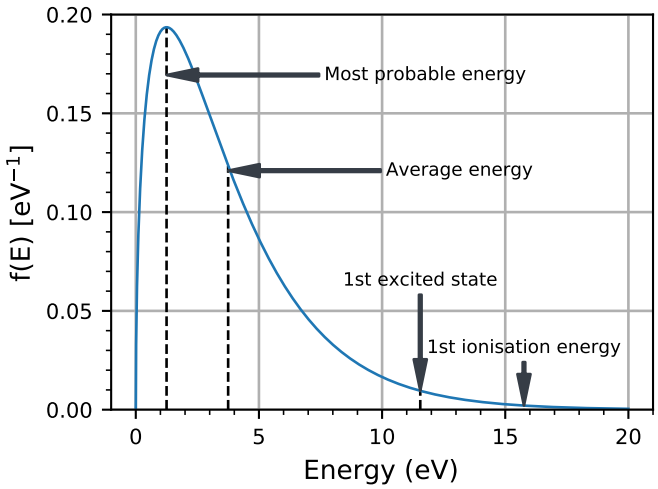

Figure 1.2: An electron energy probability distribution for a population of electrons at 2.5 eV. labelled is the most probable energy (1.25 eV) the average energy (3.75 eV), 1st excited state of argon (11.55 eV) and the 1st ionisation energy of argon (15.76 eV)

Figure 1.2 shows an example EEDF for an electron temperatures of 2.5 eV which is a typical electron temperature measured in this work. Labelled is the first ionisation energy and first excited state of argon, which is the working gas used throughout the

subsequent work. Highlighted also, is the average and most probable energy of the electrons in this distribution. The large mass difference between argon and electrons means that elastic collisions between the two, account for a minuscule amount of electron energy loss (electron - electron elastic collisions efficiently transfer energy - thus thermalisation of the population), whereas inelastic collisions allow greater transfer/losses. As one can see from figure 1.2 the threshold for inelastic collisions (above 11.55 eV for argon) is much higher than the most probable electron energy, and thus the main loss channel comes from the higher energy electrons of the EEDF.

In summary, the EEDF of a plasma is therefore a very important characteristic aspect of a plasma and is a function of electron temperature T_e and electron density n_e. Energy losses from the plasma are related to the EEDF, with T_e being related to the ionic losses and high energy electrons responsible for electron loss. All of this considered, it is clear that T_e and n_e are crucial parameters in characterisation of a plasma. The work performed for this thesis used the non-invasive incoherent Laser Thomson scattering technique to measure electron properties.

1.4 Thesis Objectives and Direction

This thesis presents the diagnostic work performed as a PhD student on bipolar HiPIMS discharges. The use of a positive bias delivered to the target following the negative pulse of a HiPIMS discharge has been a prevalent area of interest in the HiPIMS community and many reports on its beneficial use for film production and ion energy control have been produced. Diagnosis of HiPIMS and bipolar HiPIMS plasmas is challenging due to the dynamic evolution of T_e and n_e, the spatially in-homogeneous plasma, strongly magnetised electrons, deposition of target material onto invasive diagnostics, and the highly elevated plasma potential during the delivery of the positive pulse. Initially, the research objective was to perform a diagnostic study of bipolar HiPIMS discharges using the non invasive LTS technique, to measure electron properties without disturbing the discharge. However, interesting results required a deeper study of phenomena found.

The Laser Thomson Scattering (LTS) system, developed at the University of Liverpool, allowed time resolved measurements throughout the bipolar HiPIMS waveform, both in the active-glow, positive pulse delivery and after-glow to be made. The system enabled high fidelity electron temperature and density measurements, without perturbing the plasma. The study looked into how different operating parameters affected the electron properties

measured by LTS. Namely, positive pulse magnitude, length and and operating pressure. This study led to the finding of elevated electron temperatures during the positive pulse delivery in the bulk plasma, which were deemed to be a signature of a secondary discharge.

The research direction then became diagnosing the reverse discharge further. Since the LTS study was limited to electron property measurements (T_e, n_e and EEDF), other diagnostic tools that could probe other plasma parameters were used. Optical emission required little experimental alterations and allowed excited species in the plasma to be measured. An emissive probe was used to track the spatial and temporal plasma potential during the positive pulse. 2D Imaging of the plasma during the positive pulse was also performed, revealing the shape and extent of the secondary discharge inside the magnetron system.

This thesis provides plasma diagnostic characterisation of the reverse discharge, present during the positive pulse of bipolar HiPIMS operation. This was later deemed to be that of a plasma fireball (see section 2.2). Bipolar HiPIMS was a relatively new addition to the HiPIMS community and diagnostic studies were imperative to it's understanding. The ignition of a fireball discharge, during the positive pulse delivery, may well be an unwanted side effect in bipolar HiPIMS configuration and may be detrimental in industrial thin film production since its effect on the sputter disposition process is yet unclear.

1.5 Thesis Outline

The subsequent chapters in this thesis are organised as follows: Chapter 2 is the literature review, introducing the relevant background information needed to understand the work performed. It introduces the fundamentals of sputtering devices, magnetrons, both HiPIMS and bipolar HiPIMS operation, typical diagnostic tools used to measure and characterise magnetron discharges. Plasma fireballs are introduced and Laser Thomson scattering and emissive probe operation and practical aspects is provided. Chapter 3 highlights the theory behind electron property determination from Laser Thomson scattering performed in this work. Chapter 4 details the experimental arrangement, plasma source and diagnostics used, providing the reader with the procedures for data acquisition and analysis. Chapter 5 is the first results chapter, showing Laser Thomson scattering and Optical emission spectroscopy results. Chapter 6 shows the results from emissive probe and 2D imaging and is a direct extension of the previous chapter. Chapter 7 discusses the findings from chapters 5 and 6, summarising the results and some suggested further work is given.

Chapter 2

Literature Review

The aim of this section is to provide the reader with the relevant background knowledge and context to understand the work in the subsequent chapters. It provides: (1) a comprehensive literature review of the fundamentals of sputtering devices, magnetron systems, HiPIMS, typical diagnostics used to characterise magnetron discharges and bipolar HiPIMS. (2) An introduction to plasma fireballs, which is necessary to understand the subsequent result chapters in this thesis. And finally introduces, (3) incoherent Thomson scattering and (4) emissive probes, which were two diagnostics used in this work, reviewing the relevant history and practical aspects of the diagnostic.

2.1 Review of Magnetron Sputtering, Unipolar and Bipolar HiPIMS Physics

This section is organised as follows: (1), gives a description of the fundamentals of technological sputtering devices; (2) introduction to the magnetron sputtering source; (3) review of HiPIMS physics; (4) examples of diagnostics used in magnetron sputtering devices; and finally (5) an introduction and review of bipolar HiPIMS.

2.1.1 Fundamentals of Technological Sputtering Devices

2.1.1.1 Sputtering

Sputtering is the physical process of removing surface atoms from a target material by means of particle bombardment. These particles can be energetic, heavy neutrals, or ions,

but typically in a technological plasma sputtering system, the sputtering particle is an ion. These ions are accelerated through the target sheath potential and bombard the target, ejecting atoms. Target material will be ejected if the collisions provide enough energy to overcome the surface binding energy, this can be from a single collision or from multiple collision cascades. The sputtering particle may be back scattered or implanted into the target and can be released through further sputtering or from out-gassing. The ejected atoms can move to a surface (substrate) and condense to create a film or coating, this is categorised as a Physical Vapour Deposition (PVD) [13].

The sputtering yield (Y) is a measure of the removal rate of ejected particles compared to the number of incoming incident particles:

$$Y = \frac{\text{Number of ejected particles}}{\text{Number of incident particles}} \tag{2.1}$$

and is dependant upon the type of sputtering particle, it's energy, mass and trajectory, and the surface binding energy of the target [11]. For typical technological plasmas, (incident energies of $\sim$ 0.5 - 1 keV) the sputtering is dominated by the "knock-on" regime, described by a sequence of binary collisions between the ions and target atoms. In this regime, the collisions can be modelled by simple (Newtonian) conservation of momentum to give the maximum energy (E_{max}) delivered to a target atom of mass M_t from a ion of mass M_i with energy E_i to be :

$$E_{max} = E_i \frac{4M_tM_i}{(M_t + M_i)^2}. \tag{2.2}$$

Here it is assumed the ion is incident normal to the target surface. For ejection of target atoms, E_{max} must exceed the binding energy of the target material. Furthermore, equation 2.2 reaches a maximum when the masses of target and incident ions are equal. For this reason argon is the usual process gas for non reactive processes as it's mass is comparable to most materials of technological importance and is a cheaper alternative to other noble gases such as krypton or xenon.

In technological plasmas, the incident ion energy (E_i) is $\gg$ the binding energy (E_b) of the target material and thus the threshold for sputtering has been met. The ejected particles follow an energy distribution described by Thompson theory [14] and is often called the Sigmund-Thompson distribution function. This has the form:

$$f(E) \propto \frac{E}{(E + E_b)^3} \tag{2.3}$$

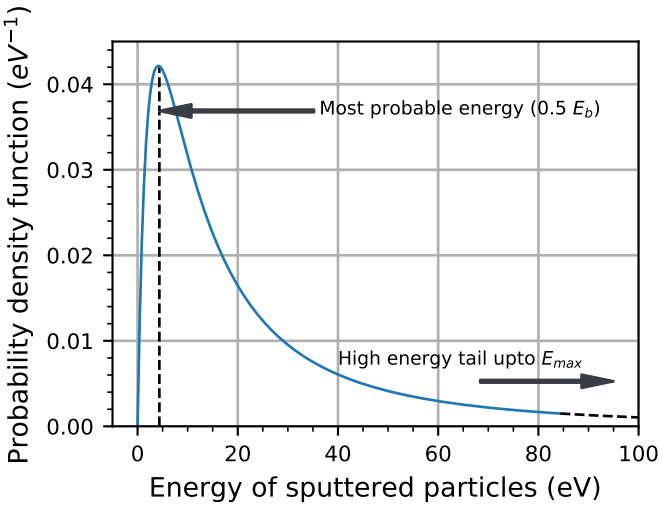

Figure 2.1: PDF following the Thompson distribution for argon ions of energy $E_i = 800$ eV, normally incident on a tungsten target of surface binding energy 8.7 eV. Labelled is the most probable sputtered energy of $E_b/2 = 4.35$ eV.

Where E is the energy of the sputtered particle and E_b equal to 8.7 eV for a tungsten target [15]. The normalised Thompson energy distribution has the shape shown in figure 2.1, following a probability density function (PDF) of the form presented in [16, 17]. For this figure, argon ions with energy $E_i = 800$ eV are normally incident on the target. The maximum occurs where $E = E_b/2$ such that, the most probable energy of sputtered metal targets are of the order of several eV. With higher incident ion energy, a greater proportion of high energy sputtered particles are created. For the case of a tungsten target, atoms with energies near the peak of the PDF will have a velocity of $v(\frac{E_b}{2}) \approx (\frac{E_b}{M_t})^{1/2} \approx 1500\ ms^{-1}$ and thus would leave the target vicinity very quickly, with low ionisation probabilities, unless a sufficiently high background gas pressure is used as in the case described in section 1.2. As aforementioned, high gas pressure results in a reduction of sputtered atom energy and is counter productive to film deposition. Devices that can extend the mean free path of sputtered particles using lower gas pressure is required. The magnetron (see section 2.1.2) is such a device.

2.1.1.2 Secondary Electron Emission

Along side sputtered atoms and ions, electrons can be released into the plasma from the target and these electrons, known as "secondary" electrons play an important role in sustaining the discharge. These electrons are accelerated by the target sheath into the bulk plasma and can become highly energetic, able to directly ionise atoms. Additionally, secondary electrons collide and transfer energy to the bulk plasma, providing a further heating mechanism that increases the electron temperature, this in turn produces more energetic collisions that further increase ionisation.

In the context of low pressure, low temperatures discharges (as in this study), the predominant secondary electron mechanism is Auger emission (potential emission) [18,19]. In short, emission occurs due to the fact that when an ion approaches the target surface, there is a finite probability that an electron (from the conduction band) will quantum tunnel across the vacuum and neutralise. The neutralisation process releases energy, which in turn, can be transferred to another conduction band electron with the potential of releasing it into the plasma. The secondary electron yield was found to experimentally follow a least squares fit [20], which leads to the condition for the energy of the incoming primary ion (E_{pot}) in relation to the work function of the metallic surface (ϕ) to be:

$$E_{pot} > \frac{2\phi}{0.78} \tag{2.4}$$

E_{pot} is the ionisation energy of the incoming ion and as such, the condition is fulfilled by singly charged argon ions of ionisation energy 15.76 eV but not for singly charged metal ions of typical target materials used in magnetron sputtering [21]. For context, the work function of tungsten is 4.55 eV and has a first ionisation energy of 7.98 eV.

2.1.1.3 Ion Bombardment of the Substrate

Ions play an important role in the production of films at a substrate [22] and the energies of the ions arriving at the substrate, can be tailored by applying a bias to the substrate or alternatively, by reversing the polarity of the cathode in some systems, for example [23,24]. Generally speaking, ions bombarding a substrate can effect film microstructures either on the surface of the film or in the film bulk, depending on the ion energies incident [25]. Low energy ions (typically below 100 eV) bombarding the substrates growing film affect the surface by increasing the mobility of adatoms, resulting in: reduced grain structures,

smoothing of the film surfaces, improved density, a decrease of nucleation density and changes in film crystallographic orientation [26, 27], [28, p. 337]. Higher energy ions (typically above 100 eV) can effect the bulk of the film through implantation deep in the growing film, causing lattice defects and compressive stress [25], [28, p. 337]. Increasing bombarding ion energy even further can re-sputter the deposited film reducing the efficiency and the quality of the films produced [25].

It should be noted that the process of ion bombardment minimises the need to raise the temperature of the substrate, thus being beneficial for sensitive, delicate samples or substrates. However, the biasing of a substrate can often be very complex and unachievable for dielectric substrates, insulating films and in some cases limited by chamber design, where the substrate is grounded. A way to counter these limitation is the reversal of cathode voltage. This raises the plasma potential, accelerating ions away from the cathode, providing a potential difference between the plasma and substrate. Allowing energetic ion bombardment to the growing film, with the possibility to tailor ion energies, depending on the reverse voltage magnitude. This type of system is explored in section 2.1.5.

2.1.2 The Magnetron and Magnetron Sputtering

The introduction of the magnetron sputtering source can be traced back to the 1960s [29,30] and has been the most widely used process for deposition of thin films ever since. The devices allowed discharges to be produced at lower pressure and lower discharge voltage (when compared to DC diode sputtering) by trapping electrons. This reduces the number of collisions in the plasma and consequently increases the energy of the sputtered particles. This lower pressure plasma is enabled by utilising the electrons in the discharge that in turn, produce the primary ions for sputtering. A short review of magnetron sputtering history is given by Bräuer et al [31]. The most popular and simple configuration was the planar magnetron, developed by Chapin in 1974 [32] (patented in August of 1979 [33]), utilises a set of ferromagnets behind the planar cathode target with either the walls of the chamber acting as the anode or a grounded ring. This traps the secondary electrons in the vicinity of the target surface, increasing the electron lifetime, yielding a greater level of ionisation concentration of the process, and thus a denser plasma is created.

In a typical magnetron, the magnetic field ($\mathbf{B}$) results in the electrons being magnetised such that their gyration radius is small in comparison to the dimensions of the sputtering device, whereas the heavier, lower energy ions are deemed unmagnetised. Calculations per-

formed by Krüger et al [34] show that for typical ion and electron energies in a magnetron system, the gyro orbits are in the range 1-10 mm for electrons and 10-1000 mm for (argon) ions. The electric field (**E**) in the cathode sheath accelerates electrons away from the negatively biased target, and the **B** field confines the electrons close to the target surface. The **B** field is designed such that there is a region where the field lines are perpendicular to the target surface normal. This combination of orthogonal **B** and **E** fields results in a closed $\mathbf{E} \times \mathbf{B}$ drift and produces a hall current that can be much larger than the discharge current itself [35]. In the planar configuration, arched **B** fields extend to the cathode surface and electrons orbiting these field lines will be reflected back by the cathode sheath, bouncing back and fourth, extending their lifetime for ionisation. These effects produce a region of magnetic trap, where energetic electrons are stuck, the plasma is most dense and the greatest target erosion occurrs due to the higher number of sputtering collisions from the now ionised process gas. This region is referred to as the racetrack.

Ultimately, the use of an external magnetic field, allows a dense region of plasma to be created, resulting in a higher deposition rate and a greater flux of energetic particle flux to the substrate compared to the non magnetised case [32, 36]. The two most common planar magnetrons are rectangular or circular, the latter being the type used in this work. The magnetic confinement of electrons creates a non uniform plasma distribution over the target surface and a localised region of erosion occurs, known as the racetrack. Efforts to maximise the transport of ions towards the substrate have been made by experimenting with the magnetic field structure. This led to the development of the unbalanced magnetron (see section 2.1.2.1). The author refers to the reviews [37, 38] for further details of the magnetron sputtering discharge.

2.1.2.1 Magnetic Field Configurations

Generally speaking, magnetron magnetic field configurations can be classified into two categories: balanced and unbalanced. A schematic of both these configurations is shown in figure 2.2. In this description, focus will be on the circular planar magnetron. The difference occurs in the strength of the central and outer magnets. The former of the two has equal strength outer and central magnets producing closed field lines (shown in figure 2.2 (c)), which electrons must escape to travel to the substrate. The later, introduced by Windows and Savvides [39, 40] still requires electrons to cross field lines, but once this occurs, the electrons are guided away from the target region (figures 2.2 (a,b)). This is

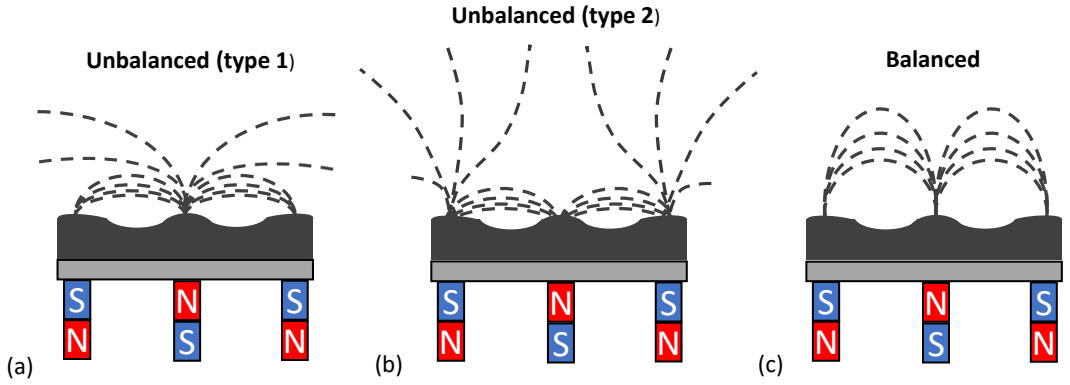

Figure 2.2: Cross sections of the commonly used magnetic field configurations in magnetron sputtering devices. (a) is the unbalanced type 1 configuration, where magnetic field lines extend outward to the chamber, (b) is the unbalanced type 2 configuration, where field lines extend outward towards a substrate and (c) is the balanced configuration where all field lines are closed. Inspiration for this figure was taken from [7].

achieved by the central and outer magnets having differing strengths.

Depending on the level of unbalancing, there are two further classifications of an unbalanced magnetron, the most common being the type-2 (as depicted in the figure 2.2 (b)), where the outer magnets are stronger than the central magnet. Here, the field lines now extend outward from the target and ion flux to the substrate is improved. The less common configuration is the type-1 (figure 2.2 (a)), where the inner magnet is stronger than the outer, meaning the field lines extend to the chamber walls rather than to a substrate. All configurations have a common magnetic null, however, in the balanced configuration, this is often far away from the target in comparison to the unbalanced configuration. The result of this is that, in the balanced configuration, electrons have to travel further (and cross many field lines) to reach the substrate and thus the plasma is local to regions near the target. The advantage of the unbalanced configuration is the greater number of electrons able escape the target region and are directed to the substrate [1]. Hence, through quasi-neutrality, a greater ion flux extends from the target as plasma is generated and is allowed to flow outward to a substrate. A further note is, due to the static, permanent magnetic field in the devices described here, erosion of the target can be highly localised

[1]This may not always be beneficial, as is the case for delicate, heat sensitive samples that would be damaged by the higher ionic flux

and the efficiency of the process is low as only a relatively low proportion of the target surface is utilised ($\leq 30\%$ [31]). Efforts have been made to increase this utilisation such as the rotating magnetron [41], where target utilisation can be as high as 90%.

2.1.2.2 Modes of Operation

Magnetrons can be used in many different power regimes but the most common are DC (Direct Current), pulsed DC, RF (radio frequency) and high power pulsed (impulsed) sputtering. In DC sputtering, a negative voltage is applied to the target continuously and this works well for metallic or metallic compound targets but fails for insulating materials and in reactive sputtering. Insulating targets can result in a build up of charge at the cathode, both reducing the ion bombardment and causing arcs. Similarly, in reactive sputtering, the reactive gas causes a compound film to be created on the target which again can lead to charge build up and arcs [42]. To counter this, pulsed DC or RF can be employed [37], with the former being the most common as it is simpler and less expensive in comparison. In the off time of pusled DC operation, the build up of charge dissipates due to the mobility of electrons in the plasma, this is sometimes aided by the uses of an added reversed target pulse after the initial negative pulse. The positive bias facilitates neutralisation as electrons are attracted to the target. Sellers [43], provides more detail of the working mechanisms that allow this type of film production.

A Novel pulsing technique was introduced in 1999 in a seminal paper by Kouznetsov et al [44], which increased the ionisation of sputtered material vastly. The technique involved applying large magnitude, negative voltage pulses to the target that facilitates high target power densities. Consequently, the pulses are kept short, with low duty cycles to stop the target from melting. This is known as high power impulse magnetron sputtering (HiPIMS) and was used throughout this study. HiPIMS is explored further in section 2.1.3.

2.1.3 High Power Impulse Magnetron Sputtering (HiPIMS)

High power impulse magnetron sputtering HiPIMS [45], boasts a large (instantaneous) power density and much higher plasma density than that of DCMS, with the important consequence of increased concentration of target ions in the discharge. An advantage of this is that by biasing the substrate, the direction and energy of these ions can be controlled and hence the films created are superior, as they are harder, denser and smoother in comparison to DC operation [46–48]. In the case of this study, the target material used is

tungsten (W) with argon process gas and as such, this section focuses on the non-reactive configuration (the reader is referred to the tutorial [16] for details on reactive HiPIMS). HiPIMS works by applying a large magnitude, negative voltage pulse to a sputtering target with typical amplitudes of 500 - 2000 V and frequencies ranging from 50 - 5000 Hz [49]. During the pulse, high instantaneous power is created, which can reach powers of up to several kWcm^{-2} (as is the case of [44]), producing very dense plasmas, up to the order of $10^{18} - 10^{20}$ m^{-3}. Consequently, a large fraction of sputtered target material is ionised and a metal rich plasma develops that enters the domain of Ionised Physical Vapour Deposition (IPVD) [50]. To stop the target from melting, the pulses are short and of the order 10 - 100s μs with low duty cycles of about 1 %. Anders [51] offers a quantitative definition of HiPIMS where they state, in the pulsed magnetron regime, the time averaged power is typically two orders of magnitude below the peak power. It should be noted that HiPIMS does however, suffer from a lower deposition rate than that compared to DCMS due, in part, to the loss of ionised target material to the target surface.

The reader is referred to the reviews on HiPIMS and its associated discharge physics written by Gudmundsson [49] *et al* and Anders [51] and the recent book [45] for a full overview of HiPIMS physics and applications. In the following section, the important, dominant discharge processes are explored and ways in which the plasma can be measured through the use of diagnostics will be introduced. It should be noted, that in the following sections, the focus is sputtering systems comprised of metal target and non-reactive discharges.

2.1.3.1 Discharge Physics

The most instructive way to introduce discharge physics comes from looking at a typical current-voltage characteristic. Figure 2.3 shows the voltage and current as a function of time for a typical discharge (in this study). The target was made from tungsten and the process gas was argon of pressure 1.6 Pa. Taking 0 μs to be the start of the pulse, as can be seen in figure 2.3, a delay in the rise of the discharge current of a few microseconds is present before the plasma ignites. This is due to the low pressure of the backing gas and the delay can be even more pronounced at an even lower pressure [44]. It has been suggested that the use of a pre-ioniser DC power supply can remove or reduce this delay [52]. Now, as the current rises, sputtered flux increases due to more argon ion bombardment on the target. Neutral and ionic species collide, heating the background gas and reduces the gas density

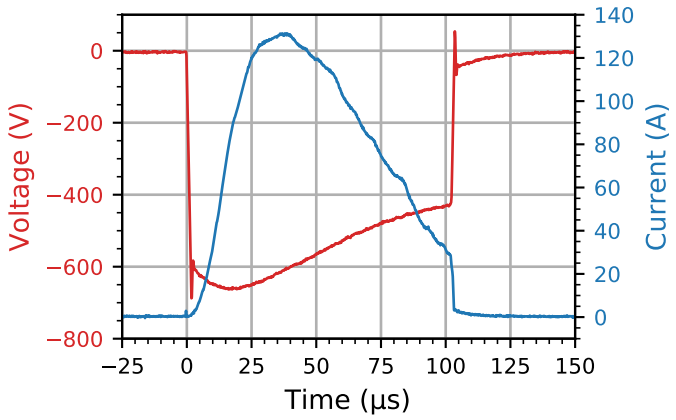

Figure 2.3: Current-Voltage-Time waveforms for discharge condition with peak power density of 450 Wcm^{-2} (normalised to the target area), pulse width of 100 μs, frequency of 50 Hz and an argon pressure of 1.6 Pa. The red line shows the applied target voltage (left y-axis) and the blue shows the corresponding current (right y-axis).

near the target. As the current increases further, the abundance of metal ions increases due to increased sputtering and increased ionisation. These ions contribute to sputtering in a process called self sputtering [53] and the target material can become the dominant sputtering material. Several factors determine whether the current continues to rise, fall or plateau: the sputtering rate of either the background gas or self sputtering of target material, the electron energy distribution and secondary electron generation and ultimately, power supply limitations. In the case of figure 2.3, the current reaches a maximum and then begins to fall due to the power supply producing non square like voltage waveforms. At pulse termnination, the plasma enters the afterglow period, where the current returns back to zero and the plasma decays, awaiting re-ignition upon the next pulse.

The important processes occurring in the discharge are discussed further in the following text, namely: Metal ionisation as the plasma transitions into a metal dominated discharge. Gas rarefaction as the density of the background process gas is denuded near the target. Self sputtering as sputtered ions contribute to target sputtering. Gas recycling as the implanted gas atoms on the target are reused, contributing to the sputtering process once more.

Metal Ionisation

The most appealing attribute of HiPIMS is the large degree of ionised sputtered species present in the discharge, ranging in concentration from 20 - 90% [54][2]. In direct current magnetron sputtering, this is usually of the order 1% or less [12]. In a magnetron sputtering system, many avenues contribute to the ionisation of sputtered material, for example: ion charge exchange, electron impact ionisation and penning ionisation. With respect to HiPIMS, electron impact ionisation is the dominant process during the on-time of the pulse, this was found through a time-dependant global model by Gudmundsson [55]. A high electron density alongside the relatively low first ionisation energies of metals, results in large proportions of ionised metal inside the plasma. After termination of the pulse, charge exchange and Penning ionisation, [56] become the dominant processes of metal ionisation due to the electron density drop off and temperature decrease. This in turn, reduces the fraction of ionised metal atoms and analogies can be drawn to DCMS operation in which ionised metal concentration is low.

Gas Rarefaction

It is well know that in magnetron sputtering, the density of neutral gas particles close to the sputtering target vicinity is reduced during plasma operation. This is known as gas rarefaction [57] and reduces the density of gas atoms available for ionisation. There are several main contributors to gas rarefaction. One of which arises from an increase in local gas temperature near the target due to: heat transfer from the sputtering target, energetic secondary electrons (see section 2.1.1.2) accelerated in the sheath and Ohmic heating in the presheath [58]. Ionisation of the process gas directly lowers the gas density as the concentration of gas species decreases as atoms are ionised. A significant sputter wind [59] is also present, where sputtered target material collides with the process gas atoms, transferring energy to either further heat, or physically eject atoms near the target surface, depleting this region of gas atoms. Gas rarefaction has been measured and first reported by Hoffman [59] for the DC magnetron case and simulations reported in [60] by Kadlec show that in HiPIMS the gas becomes rarefied by an order of magnitude. HiPIMS has a more pronounced rarefaction due it's greater energetic distribution of sputtered material, large sputter rate in the on-time, denser plasma and the fact that large fractions of the

[2]There is many differing ways the fraction has been found, with discrepancies between methods. See [54] for further details regarding the techniques used to measure the ionised fraction and the different methods used to quantify the ionised fraction.

process gas is ionised. A further point to mention is that, gas rarefaction can result in a lower discharge current and the discharge transitions into a plateau regime [61] comparable to a DC discharge. This is because the discharge is dominated by metal ions and these do not meet the requirement for secondary electron emission (see section 2.1.1.2), thus the discharge is limited in current.

Self Sputtering and Gas Recycling

During the on-time of the pulse, following electron impact ionisation of the sputtered material, a fraction of ions created are attracted to the target through the cathode fall potential (sheath) rather than travelling to a substrate due to their low energy. These ions contribute to the sputtering process and can sputter further target material in a process called self sputtering (SS) [53]. Following gas rarefaction, ionised metal becomes the main source of sputtering but as aforementioned, the required threshold for electron emission is not readily achieved with singularly ionised metals and as such, the discharge can be limited by self sputtering. This is thought to contribute to the lower deposition rate of HiPIMS when compared to similarly powered DCMS (see section 2.1.3.2). However, it was shown that self sputtering could negate the need for a process gas in certain applications, as self sputtering can sustain the discharge solely [62, 63]. Doubly ionised metal in the discharge can contribute to secondary electron emission, however Ohmic heating was found to be the dominant electron energisation mechanism over the sheath accelerated secondaries [58], such that, secondary electron yield is not imperative to sustaining the discharge. Another factor that plays a role in the discharge, and thus the deposition, is the recycling of the process gas. The process gas can be trapped in a repetitive loop [64] and for low sputter yield materials, the recycling can become the dominant factor of the discharge current, that cannot simply be explained by SS. Basically, background gas ions can be implanted below the target surface and some of these can diffuse to the surface, out-gassing and contributing to the discharge once again, ionising and contributing to secondary electron emission.

2.1.3.2 Deposition Rate

It is well known in the HiPIMS community, that the deposition rate to a substrate in a HiPIMS discharge is generally lower than the comparable averaged powered DC sputtering system, with rates typically ranging from 25-35% of the DC systems [65]. The target

material atoms are ionised close to the cathode surface and can be lost to the target through back attraction as they return to the negatively biased target [65,66]. This results in a comparably lower deposition rate when compared to similar power DC magnetron discharges. Therefore, the same benefit of HiPIMS is also it's downfall. This is referred to as the HiPIMS compromise and efforts to find the optimum balance between the deposition rate and ionised flux fraction have been performed [67]. Attempts to understand and counter the low deposition rates have been made over the years, experimenting with: magnetic field structure, pulse width variation and the mixing of different pulsing regimes.

Decreasing the magnetic field strength is known to increase the deposition rate [68–71] and the use of a tripack configuration, where 3 zones of electron confinement are present with extending open field lines [72], has shown to enhance deposition rates compared to the standard B-field configuration. The use of an external auxiliary magnetic field has also shown enhancements to deposition rates, compared to standard operation [73]. Shortening of the on-time pulse has also shown to increase the deposition rate [74,75], due to the quicker elimination of back attraction of ions through the potential drop over the ionisation region. A further way to increase the deposition rate is the combination of two differing operating regimes, where secondary power is delivered to the target in the afterglow. Examples of this include: HiPIMS coupled with medium frequency magnetron sputtering [76] and HiPIMS coupled with a DC-like pulse [77]. This enhances the amount of target neutrals available for deposition.

Another pulsing regime used in literature to alleviate the back attraction is the use of a positive pulse immediately after the negative HiPIMS pulse, known as asymmetric bipolar HiPIMS. This is explored in section 2.1.5. The philosophy of bipolar HiPIMS is to repel ions away from the target vicinity by raising the plasma potential, accelerating them to a substrate. Furthermore, bipolar HiPIMS can eliminate the need for substrate biasing as the incident ion energies to the growing film can be tailored.

2.1.3.3 Summary

HiPIMS utilises very high power densities with relatively short pulses and duty cycles to create a dense plasma that has significant ionised target material fractions. Due to the large fraction of ionised target material in the discharge, HiPIMS belongs to the family of depositions known as ionised physical vapour deposition (IVPD). It is characterised with very high plasma densities up to 10^{20} m^{-3}. The energy of the ionised target atoms

bombarding a substrate can be controlled by applying a bias to a substrate [78, p. 64], where the ions fall through the formed sheath potential. Films formed using HiPIMS have been shown to be denser, smoother and harder than DC magnetron sputtering.

It is imperative to point out that up to this point, all of the above descriptions have depicted a plasma that is homogeneous, with uniform plasma distribution in the magnetic trap. However, this has been found to not be the reality. Localised regions of brighter (and thus denser) plasma emission has been found above the racetrack, these localised regions are known as spokes and were first observed by Kozyrev et al [79]. They are present in both DC and HiPIMS discharges and travel in the $\mathbf{E} \times \mathbf{B}$ direction with regions of the plasma increasing and decreasing in density such that they travel with a group velocity of the order of kms^{-1}. The electric fields created azimuthly by the formation of spokes have been found to have a resultant effect on the sputtered ion energy and deposition rate in a HiPIMS discharge. Further descriptions of spokes can be found in the review [80] but are beyond the scope of this thesis.

There exists a double edged sword scenario in HiPIMS, where the advantages levels of ionised target material in the discharge, hinders the deposition rate of such systems, when compared to DC magnetron sputtering. This is attributed to the back attraction of ions that cannot escape the ionisation region. Changes to the magnetic field structure, pulsing regimes and shortening of the pulse length have all shown to improve the deposition rate. A promising alternative avenue to improve the deposition rate, is the use of bipolar pulsing, in which a positive pulse is delivered to the target in the afterglow in an attempt to repel the ions away from the target - towards the substrate.

2.1.4 Plasma Diagnostic Techniques used for Magnetron Discharge Characterisation

This section aims to give the reader background of some of the diagnostics that have been used to measure plasma properties in magnetron sputtering devices. For a more comprehensive overview, the reader is referred to the review by Britun et al [81], which focuses on diagnostic techniques used to determine plasma properties in HiPIMS discharges. Diagnostics are imperative in any plasma study, allowing one to access the fundamental properties of the discharge. Plasma properties are directly related to substrate growth, thus, knowledge of discharge processes allows one to improve and tailor film production. Magnetron discharges provide a very harsh and often transient environment for plasma diagnostics

but over the years there has been copious amounts of diagnostic studies performed in both DC magnetron sputtering and HiPIMS discharges. Generally speaking, plasma diagnostics can be separated in to two categories, with invasive and non-invasive techniques. Invasive techniques involve immersion of apparatus inside the plasma, which may perturb the local plasma properties due to plasma interaction with the instrument. Non-invasive techniques typically involve externally measuring the plasma parameters through, for example, the use of optical diagnostics.

The classic example of an invasive technique is the use of electrical probes, where a metallic electrode is placed inside the discharge. The most common method is the single tipped Langmuir probe (LP), first introduced in 1926 by by Mott-Smith and Langmuir [82], where a voltage bias sweep is applied to the tip. The probe collects either the ion current, electron current or, a mixture of both depending on the bias, creating a characteristic I-V curve in which plasma parameters can be determined. An example characteristic curve is shown in figure 2.4. Analysis of the I-V curve yields information on the plasma potential (V_p), floating potential (V_f), electron temperature (T_e), electron energy distribution function (EEDF) and the density of electrons and ions (n_e, n_i).

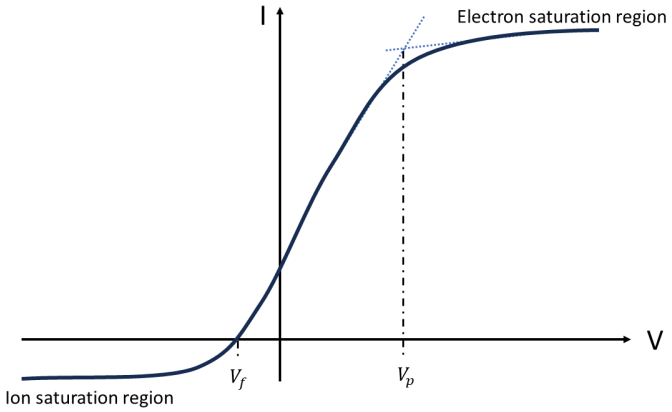

Figure 2.4: Ideal I-V curve of a single tipped Langmuir probe

Due to gated electronics and the commercial availability of LP acquisition equipment, such as the ESPion device manufactured by Hiden Analytical, (see for example a relevant study in the context of this thesis [83]), time resolved measurements can be made throughout the HiPIMS discharge evolution, with time resolutions below 1 μs. However, LP's do have several draw backs. Firstly, since the probe tip is in contact with the plasma,

sputtered target material can be deposited on the tip and cause contamination. Secondly, the probe perturbs the local measurement area of charged particles through collection of either ion current or electron current. Thirdly, interpretation of the I-V characteristic can often prove difficult, with many differing theories that can be applied to extract plasma properties. Finally, unique to the magnetron, the added presence of magnetic field further complicates the interpretation of LP results.

Several other probe configurations have been used in magnetron devices, which extend the singled tipped LP, exist which include double [84, 85] and triple probes [86, 87]. The former has two tips inside the plasma, separated in space so the tip sheaths don't overlap, which are isolated from ground and are biased. Each tip receives equal but opposite polarity biases and by performing a bias sweep, a characteristic I-V curve is produced from which plasma parameters can be found. The latter uses 3 tips inserted in the plasma, and does not require a voltage sweep. One of the three tips sits at the floating potential of the plasma, whilst the other two work similarly to the double probe, where the tips are biased with the same voltage, with opposite polarities but at a fixed voltage. Emissive probes have also been used to track the plasma potential in magnetron discharges (see for example [35]), involving heating of a probe tip to release electrons. At a certain heating current (applied voltage), the probe releases electrons and will float at the plasma potential, able to quickly track potential changes in pulsed magnetron discharges. Ion energy distribution functions (IEDF) have also been measured in magnetron discharges by the use of a (gridded) retarding field energy analyser (RFEA) (for example, [88, 89]), by the use of several separate grids, one of which acts to repel electrons and another which collects the ions, by sweeping the voltage similarly to an LP. Example IEDF's are shown in figure 2.5 from a relevant study in the context of this thesis for several bipolar HiPIMS pulses. The species of ions arriving at the analyser cannot be distinguished as this technique is not mass resolved.

Mass spectroscopy techniques have been applied, allowing time and mass-resolved measurements of ionic energy distribution functions (IEDF's) as well as neutrals. As this technique can separate the masses of incoming projectiles, it allows detailed understanding of the individual species in the plasma and can provide details of plasma chemistry associated with reactive plasmas [90]. An example of this technique is the quadrupole mass spectrometer (QMS) that uses a series of magnetic lenses to focus the ions through the instrument. The ions are directed into the electrostatic energy analyser, separating them by energy, before feeding them into the quadrupole mass analyser which separates the ions

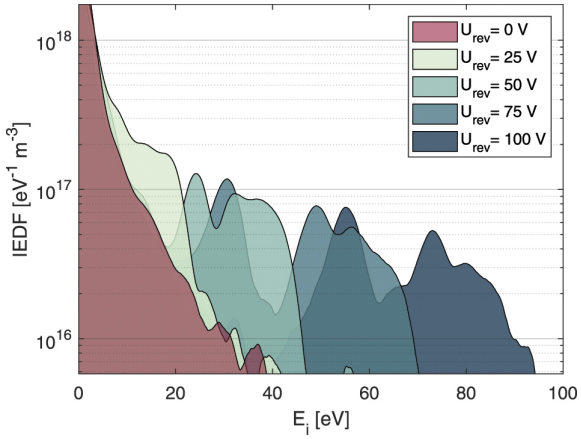

Figure 2.5: Time averaged IEDF's examples for bipolar HiPIMS pulsing, taken from [89]. The negative and positive pulses had duration of 70 μs and 100 μs respectively and U_{rev} denotes the positive pulsing voltage.

based on their mass-to-charge ratios. Due to the equipment sensitivity and the need for unobstructed ion paths through the system, the device needs to be held at vacuum. An example of it's use in literature for DC, pulsed, HiPIMS and bipolar HiPIMS discharges are given in [91–94] respectively. Typically in MS, only a small amount of ions are needed for detection, making the technique very sensitive (ideal for lower density discharges) and virtually unperturbing to the plasma. However studies are usually limited to far away regions of the plasma and are space-integrated.

Optical techniques have been used to measure plasma parameters and are mostly considered non-intrusive. The most popular being optical emission spectroscopy (OES). Light is generated inside a plasma when spontaneous relaxation (de-excitation) of an excited species occurs, releasing a photon with energy related to the transition between states. A spectrometer separates the wavelengths and from a given spectrum, determination of the transition that caused the peak can be found, and thus used to identify the species present in the plasma. A typical experimental arrangement for time-resolved OES measurements are shown in figure 2.6, where an external trigger provided by the power supply allows the detector to synchronise light detection. Details of the experimental arrangement for this work is given in section 4.2 and an example OES spectrum is provided in figure 4.12. OES is a line-of-sight measurement, resulting in poor spatial resolution.

To extract plasma parameters, such as plasma density and electron temperature, a

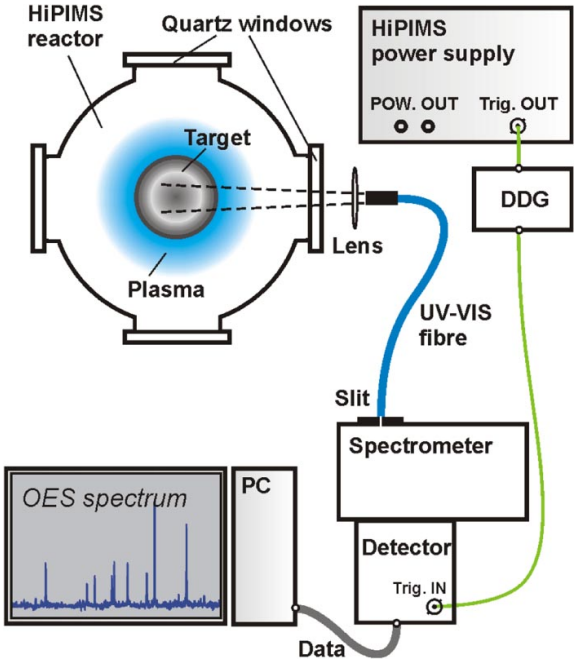

Figure 2.6: A typical experimental arrangement for time-resolved OES measurements of HiPIMS pulses, taken from [81].

complex model is required. Due to the spherical symmetry usually found in magnetron discharges however, space-resolved information can be determined following Abel inversion [95, 96]. OES is inherently non intrusive and non perturbing to the plasma and has been used copious times to measure plasma properties of magnetron discharges. The reader is again referred to the review [81] for further information on OES and it's applications in magnetron sputtering, for which there have been many.

Laser based diagnostics have been used for plasma diagnostic studies of magnetron discharges with various degrees of intrusiveness. Two examples of such techniques are Laser-Induced Fluorescence (LIF) and laser Thomson scattering (LTS). The former uses a laser to excite species in the plasma and the corresponding emitted photons from relaxation is captured by a detector. The principle of the technique is shown in figure 2.7 for both LIF and two photon absorption LIF (TALIF) where either one or two photons are absorbed. TALIF is used when excitation of the selected transition is not achievable using conventional lasers and instead the absorption of two photons is required to achieve the excitation. Further details of the use of LIF (TALIF) and the required experimental

arrangement are given in [81]. LIF has been used in magnetrons to measure the velocity distribution function of sputtered particles [97,98] and can be used for 2D density imaging (see for example [99]).

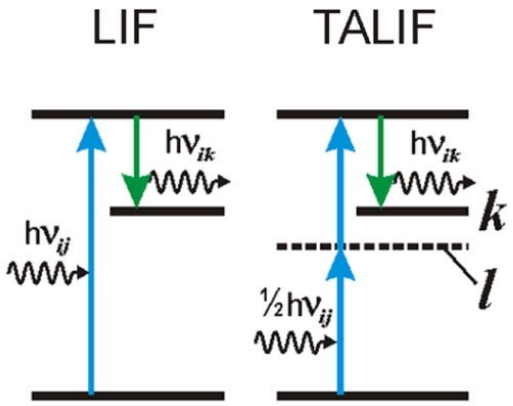

Figure 2.7: Schematic of the LIF (left) and TALIF (right) principle, with incoming photon in blue and emiited photon in green. Taken from [81].

The latter technique uses a laser source incident on the plasma, where the incoming beam scatters upon interaction with charged particles in the plasma. The resultant scattering spectrum is typically separated using a spectrometer and collected by a detector. In the incoherent regime, the technique relies on the Doppler shift of scattered laser photons to infer information about the electron velocity distribution function (EVDF), from which T_e can be found. The intensity of the scattering signal is related to the density (n_e), but requires a further calibration which can either be done by Rayleigh or Raman scattering. LTS provides local measurements of electron properties with excellent spatial and temporal resolution (mm and μs scale respectively) and has straightforward data interpretation and, unlike the LP, are unaffected by magnetic fields. However, due to the low cross section of TS and stray light issues, the design of a TS experiment is often very complex and limited to studies with relatively high n_e.

Examples of LTS equipment design and it's use in magnetron sputtering discharges are found in [100–103] and is detailed in section 4.2 for the work performed in this thesis. Although laser diagnostic techniques are very advantageous and are mostly considered non intrusive, careful considerations of laser perturbation, (such as laser heating and photo-ionisation - see section 4.2.6) to the plasma needs to be made when designing experiments, in an effort to minimise laser induced effects.

2.1.5 Bipolar HiPIMS

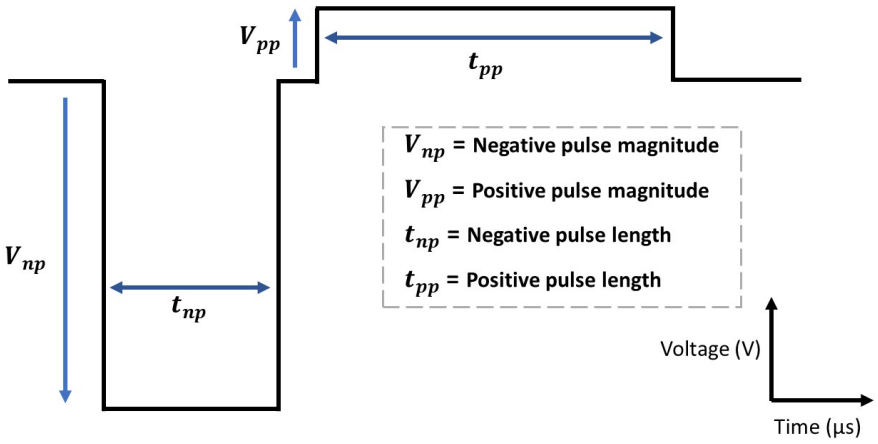

Figure 2.8: An annotated ideal bipolar HiPIMS voltage waveform.

Asymmetric bipolar HiPIMS or HiPIMS with a positive kick has been introduced recently to counter the back attraction effects talked about in section 2.1.3, and as an alternative to substrate biasing [89,104,105]. Bipolar HiPIMS modifies the traditional HiPIMS pulse by adding an asymmetrical positive pulse to the end of the regular negative HiPIMS discharge pulse, see for example [99,104]. The positive pulse voltage V_{pp} is normally in the range 50 - 300 V (up to 900 V in [106]) and varies in length (t_{pp}) from under 10 μs to several 100 μs [94, 99, 107, 108]. An idealised bipolar HiPIMS voltage waveform is given in figure 2.8, with the annotated nomenclature used throughout the text defined. Asymmetrical pulses have been used in pulsed DC systems since the late 90s, see for example [23,109,110], and they have been shown to be capable of ion energy bombardment. While it was common to add an additional negative bias to the HiPIMS pulse using a pre-ioniser [52, 111], to aid re-ignition of the discharge, the use of a positive pulse is a relatively new addition to HiPIMS systems.

The origin of bipolar HiPIMS operation can be traced back to the suggestion made in the paper by Konstantinidis et al [112] in 2006, where they propose that the use of a reverse pulse would accelerate ions to a substrate, increasing deposition rate. The first use of bipolar pulsing in HiPIMS operation was by Nakano et al [113] in 2010, where a positive pulse was delivered for the full off-time of the discharge. It was found that the inclusion of a

positive (reverse) target voltage in the afterglow significantly affected the discharge current rise-time of the subsequent on-time, as plasma ignition is suppressed due to the enhanced loss of charged particles. The first in depth study utilising different positive pulse lengths and magnitudes in a bipolar HiPIMS system to improve film qualities was made by Wu et al [104], in the deposition of Cu films on Si. They observed an increased deposition rate and reduction of tensile stress in their thin films when bipolar HiPIMS was used. Since that study, films produced by bipolar HiPIMS have been shown to, for example: have an increased density [24, 105], smoother surfaces [105, 114], improved hardness [24, 105], greater adhesion strength to the substrate [114] and a higher sp^3 content in diamond like carbon films [105, 107].

2.1.5.1 Effects of Positive Pulsing

In conventional (unipolar) HiPIMS, there exists a large density of sputtered ionised target material close to the target after the delivery of the negative pulse. These ions may be lost to the target instead of contributing to deposition. The positive pulsing method acts to counter this back and aid transport of the metal ions to the substrate. In the bipolar HiPIMS afterglow period, in which the positive pulse is applied, the plasma decays, but substantial electron densities are still present throughout this period with $n_e \sim 10^{17}$ - 10^{18} m^{-3} (see for example [1,2,83]). This plasma will react on application of positive pulse and collective behaviour leads to the applied electric field being shielded in the bulk plasma. This results in the establishment of positive plasma potential (V_p), close to, or matching the target potential. Therefore, ions can be accelerated to bombarding energies up to $E \sim eV_p$, without the need for sample biasing [24]. However, it would require the substrate to be grounded, as demonstrated by Viloan et al [115].

In some cases, during the positive pulse period, a distinct moving potential structure can be observed in the bulk plasma [114] [116]. These structures of raised positive potential at the rear and low potential at the head, advance downstream from cathode to substrate, with speeds of the order of the ion acoustic speed. These features are indistinguishable from a classic double layer, with a distinct plasma potential step (see reviews [117, 118]), that necessarily accelerates ions and electrons in opposite directions across the layer. The nature of the structure moving from cathode to anode will also enhance ion motion toward the substrate. However, this result is not a universally observed phenomenon (see section 2.1.5.2).

Some authors have reported a lower deposition rate using bipolar HiPIMS compared to unipolar pulsing (see for example [89, 115, 119]). The lower deposition rate has been understood as a consequence of significant radial loss of ions to the grounded vessel walls. The transport of ions to the walls is further enhanced for strongly unbalanced magnetic field configurations; where a large proportion of open field lines intercept the chamber. In an attempt to enhance ion flux to a substrate, Han et al [120–122] and Luo et al [123] have used combinations of bipolar pulsing with auxiliary anodes and solenoid coils. The use of the auxiliary anode reduced the radial loss of ions sideways (towards the vessel walls), and solenoid coil enhanced the magnetic field structure perpendicular to the target. This had the overall effect of increasing plasma density and ion current at a typical substrate position [122].

A potentially unwanted side effect of asymmetric bipolar HiPIMS is the ignition of a a secondary discharge in the positive afterglow, found in some systems [1, 2, 108, 124, 125], indicated by the reappearance of background gas and target ion emission and elevated electron temperatures. Kozák et al [108], provided a qualitative image of the spatial density map of Ar^+ ions, recorded by an iCCD towards the end of their positive pulse (reverse discharge phase). This is shown in the insert of figure 2.9, with light emission predominantly centred on the magnetron axis (centre-line) near the positively biased target.

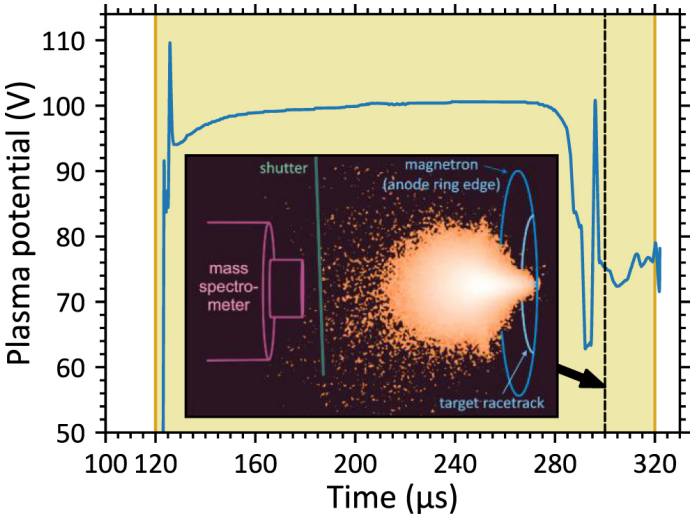

Figure 2.9: Plasma potential measurements at 100 mm from an unbalanced magnetron with a 100 mm diameter Ti target. The insert shows the spatial density map of Ar^+ at time t = 300 μs. Reprinted from [108].

These discharge have been labelled a "reverse" discharge by the authors, as the cathode potential is reversed and the respective anode and cathode switch polarity. Fast electrons travelling to the positive target and energetic secondary electrons released from the chamber walls have been suggested as the candidate for the reverse ignition, however, the exact mechanisms are still to be fully explored. The conditions under which the reverse discharges form are similar to those studied by S. Chauhan [126], who observed the spontaneous formation of a glowing droplet shaped discharge centred on the target, a discharge he attributed to the fireball phenomena [127, 128] (see section 2.2).

2.1.5.2 Plasma Property Measurements

In the last several years, a number of important diagnostic studies have been performed to understand the basic plasma processes that lead to beneficial properties in thin film produced using asymmetric bipolar HiPIMS. These include: electrical probe measurements, using Langmuir probes or emissive probes, optical techniques such as optical emission spectroscopy, laser induced fluorescence and laser Thomson scattering and ion energy analysis, using mass spectroscopy and retarding field energy analyser. Some of the important results most relevant to this study found in the literature are described in the following text.

Ion Energy Analysis

A key tool used for energy analysis has been energy-resolved mass spectrometry, which has revealed that the positive ion (argon and metal) kinetics are altered by the application of the positive pulse. From this, in general there is a generation of high energy ions at the substrate with upper energies corresponding to the applied positive voltage. For instance, Velicu et al [114], investigated the effect a positive pulse has on the time-averaged ion energy distribution function (IEDF) using a copper target in a balanced magnetron, observing two main energy peaks (at the substrate position); a low energy peak near zero energy and a high energy peak, corresponding to the applied reverse pulse magnitude which was not present in the unipolar pulses. Tiron and Velicu [116], extended the study to investigate the effect of positive pulse length on the ion kinetics and saw for short positive pulses, only a small fraction of copper ions gain energy but for increasing length, the ions gain successively more energy, with the count rate of the high energy peak increasing at the expense of diminishing ions at low energy. This effect was explained by the generation of a moving ion accelerating double layer structure that evolves in time. In bipolar HiPIMS using

titanium targets, Keraudy et al [119], found similar characteristics in the time-averaged IEDF's with Ti^+ and Ti^{2+} peaks at low energy corresponding to on-time ion generation and at high energy, corresponding to the positive target potential in the afterglow. A simple model of the potential structure in the discharge was also proposed, characterised by three distinct regions: the magnetic trap, a transition region, and the grounded region. Time-resolved IEDF's of Ti^+ ions were measured by Kozák et al [108], in which the magnitude of the high energy peak scaled with positive pulse length for duration less than 100 μs, with longer lengths yielding no additional benefits as the plasma had sufficient time to diffuse. They found that increasing the delay between the end of the negative pulse and initiation of the positive pulse affects the widths of the high energy peaks, with a distinct narrowing.

Avino et al [129] found for niobium sputtering, long positive pulses (> 250 μs) lead to the entire population of ions (Ar^+ and Nb^+) being shifted to higher energies. Detailed investigations of the time-averaged IEDF's of the sputtering of cobalt, in both reactive HiPIMS with argon and oxygen atmosphere mixtures [124] and HiPIMS with argon atmosphere [83] have been made, revealing differences between the cobalt and argon ions. High energy peaks, corresponding to the applied positive target potential was found for all species, with Co^+ showing a larger spread in energy than argon, thought to be due to the location in which the ions are created. Time-resolved IEDF measurements of the IEDF's in the sputtering of yttrium provide details on the appearance of different energy peaks [125], where a lower energy peak corresponding to ions created within the negative on-time and a higher peak found during the early parts of the positive pulse were found.

Viloan et al [94], experimented with both the negative and positive pulse on-time with a Ti target, they concluded that, careful selection of pulse lengths are required to maximise the production of energetic ions during the positive pulse. Short negative on-times are beneficial to maintain a high concentration of ions near the target. Longer negative on-times allows significant fractions of ions to escape and thus not be susceptible to acceleration in the positive pulse. The length of the positive pulse needs to be long enough to accelerate large fractions of ions but, not too long as to deplete the plasma. For a negative pulse length of 10 μs and positive pulse length of 200 μs, they found that almost 100 % of the ions can be accelerated to high energies in the positive pulse.

Walk et al [89], determined the IEDF's arriving at a gridded retarding field energy analyser (RFEA), for bipolar operation with a niobium target, experimenting with positive pulse magnitude and negative pulse duration. From the IEDF's, they calculated the bombarding ion flux density Γ_i, and the flux density Q_i, to a grounded surface. Similarly,

with the application of the positive pulse, the IEDF's have peaks corresponding to the applied reverse voltage (sitting 10 eV below). However, these peaks are much broader than those found in other studies. It was found that Γ_i was not strongly influenced by increasing positive pulse magnitude, but a marginal reduction was measured for increasing positive pulse magnitudes. Γ_i, significantly increased when the negative on-time was decreased. Q_i, dramatically increased with the inclusion of a positive pulse, scaling with the applied positive potential, peaking approximately 6 times larger than the values from the negative on-time, with a five-fold overall increase. Reducing the negative on-time resulted in higher and broader peaks, with Q_i increasing four-fold.

Optical Techniques

Optical diagnostics have also been used on bipolar HiPIMS discharges. Laser induced fluorescence (LIF) has been performed by Britun et al [99] to map the 2D density evolution of Ti^+ ground state ions in the positive pulse of a bipolar HiPIMS discharge. They found that, during the positive pulse, a shrinkage of the ionisation region near the cathode is present, with fast ion acceleration from the cathode resulting in a faster redistribution of ions in the plasma than compared to the case with no positive pulse. Further confirmation of the observed effects were shown later in [130] by LIF measurements performed at several positive pulse magnitudes and differing negative pulse peak currents. Examination of the effect of magnetic field topology in closed and open fields was later explored in [131] by LIF measurements, revealing larger ion depletion in the closed arrangement. Optical emission spectroscopy has yielded detailed information on the excited species during bipolar pulsing, in which strong Ar(I) line emission is observed in the positive pulse, indicating additional heating of the electrons and the formation a reverse discharge [108, 124, 125]. The authors suggest that two mechanisms may be at work: the generation of fast electrons returning to the positive target [108, 125], and the generation of secondary electrons from the chamber walls [125].

Laser Thomson scattering, OES and 2D broadband optical imaging have also been performed by the author [1, 2] and the results of these studies will be described the in subsequent chapters.

Electrical Probes

Time-resolved Langmuir probe measurements have shed light on the fundamental processes in bipolar HiPIMS discharges. For instance, it is observed that the floating and

plasma potentials are raised rapidly on application of the positive pulse to values comparable to the target voltage, and maintained throughout the length of the positive pulse [83, 108]. Pajdarová et al [132] using a probe with sub-micro-second resolution showed that at the initiation of the positive pulse, large differences between plasma and floating potential were present, up to 200 V, indicating the generation of energetic electrons, confirmed by observation of short-lived hot electrons with temperatures up to 150 eV, derived from the probe characteristic. This process is simultaneously accompanied by a significant decrease in electron density. They also found that the average energy flux of ions to the substrate during the positive pulse, increases with positive pulse height and shorter delay times between the negative and positive pulses.

Emissive probes have been used to determine the spatial and temporal evolution of the plasma potential in the bulk plasma of bipolar HiPIMS discharges. As previously discussed, double layer structures have been found, present during the positive pulse of bipolar HiPIMS operation [114, 116], moving from cathode to anode, enhancing the ion motion toward the substrate. However, these structures are not ubiquitous, for example Kozák et al [108] found that for an unbalanced magnetron, the plasma potential was raised very quickly, some 100 mm, from the target after initiation of the positive pulse, indicating no moving structure. Hippler et al [83], and Pajdarová et al [132], found that both floating and plasma potential reaches high positive values at large distances from the cathode in a similar fashion. Walk et al [89], similarly found no direct evidence of a double layer structure present in their specific magnetron system geometry. It is conjectured by Tiron and Velicu [116] that the plasma and magnetic topology of the device may influence the response of the plasma potential in the positive pulse period, and the possible development of a moving double layer in the plasma during the positive pulse. They suggest that short negative HiPIMS pulses followed by highly positive short pulses are favourable for a double layer formation, as an effective ion acceleration mechanism. Kozák et al [108] suggest that no layer will be found in strongly unbalanced magnetron configurations, in which the fast electrons outside of the magnetic trap can reach the biased target with ease, so equilibrating and raising the potential quickly in the bulk. Currently, it is still difficult to predict whether moving potential structures will appear in a particular magnetron during bipolar operation.

An interesting study performed by Zanáška et al [133], measured V_p using an emissive probe in their unbalanced magnetron at a typical substrate position (10 cm) for varying negative pulse lengths and magnitudes, positive pulse magnitudes and working gas pres-

sure. The study aimed to find the optimal conditions for ion acceleration to a substrate without the need for it to be grounded. The authors found four distinguishable phases of plasma potential at the substrate position, that evolved throughout positive pulsing, with differing time periods dependant on the pulsing parameters. On initiation of the positive pulse it was found that V_p followed the target potential (phase A). V_p closely matches the applied target potential until a sharp drop to ~ 0 V is measured (phase B). V_p is situated at ~ 0 V for the rest of phase B, until large oscillations in both V_p and target current are measured (phase B/C). The plasma potential then finally stabilises to values 20 - 40 V below the applied target potential (phase C). Spatial V_p measurements revealed that during phase B, elevated potentials were found inside the magnetic trap. This combined with $V_p \sim 0$ V at a typical substrate position were proposed as a suitable ion acceleration mechanism. In their system, phase B could be elongated by using low pressures and high negative pulse currents with long duration's. In phase C, a double layer structure revealed itself in front of the target, with high potential side inside the magnetic trap. The authors suggest this may have been connected to the presence of a secondary reverse discharge.

Emissive probe measurements have also been performed by the author [1, 2] and the results of these studies will be described in subsequent chapters.

2.1.5.3 Summary

Asymmetric bipolar HiPIMS is a relatively new addition to the IPVD community, in which the unipolar HiPIMS pulse is modified with the addition of a positive (reverse) polarity pulse, delivered to the target after the negative on-time. It has received great interest due to it's aptitude for ion acceleration (see section 2.1.5.2), with ion energy tailoring capabilities that produce high quality films. The technique has also shown to improve deposition rate (in some cases) and eliminates the need for substrate biasing. Some studies have found a moving double layer structure, extending out from the target, capable of ion acceleration. In other cases, a secondary discharge was found during positive pulse operation with similarities to a plasma fireball.

To date, bipolar HiPIMS has been studied as a means of depositing engineering quality thin films, including Cu [104,114,115], Ti [99], TiN [24], TiNbCrAlHfN [134], carbon [135], diamond like carbon [105, 107, 136], CrN [137, 138], CrAIN [139] and cobalt oxide [124]. The interest in asymmetric bipolar HiPIMS has prompted many diagnostic studies over the past 4 - 5 years and is the motivation behind the work in this thesis. The contributions

to the field made in this study will be discussed in the subsequent chapters.

2.2 Fireballs

Throughout the research performed, as will be shown in the subsequent results chapters, during the positive pulse of the bipolar HiPIMS system, a reverse discharge ignited with similarities analogous to that of a plasma fireball. This section gives an introduction to this phenomenon, detailing what a fireball is and what conditions allows fireball formation in magnetron devices. In short, a fireball is a specific type of anode-plasma interaction, in which ionisation occurs within the anode sheath itself, creating a glowing discharge that expands 100s of Debye lengths from the anode into the bulk; named fireball for its visual appearance [128].

2.2.1 Introduction

The work by Langmuir [140] in 1929 can be attributed as the first observation of what is now most popularly called a fireball. He reports on experiments with hot cathodes in mercury vapour with different sized anodes. He states that with small enough anodes, a point is reached where an electron sheath becomes a possibility. An anode glow can appear in the system, if the potential drop across the anode sheath approaches the ionising voltage of the gas. In his experiments, an increase in pressure caused a second discharge to be produced that protruded from the anode with a globular luminous shape. Langmuir stated that the higher pressure caused the rate of ion production to increase, causing the electron sheath to break down, and a double layer is formed at the boundary of the secondary glow. The double layer had high potential inner positive space charge and outer negative with the drop across of the order of the ionising potential. Since then, many others have observed and studied this phenomena, with authors referring to the phenomenon with many different nomenclature such as: “fire rod” [141], “anode spot” [142], “plasma contactor” [143], “plasma double layer” [144] and “anode double layer” [145]. From here on out this phenomena is referred to by the most common name; “fireball”.

Fireballs are discharges stemming from an electrode in a plasma system, separated from background plasma by a double layer. They are usually several cm in length and are associated with a quasi-neutral, quasi-spherical bright region. They occur when the electrode is biased more positively than the plasma potential, and the formed double

layer provides a mechanism for a steady state, sustained fireball, balancing electron and ion losses. Example applications of fireballs include their use in producing a source of ions [146], dust confinement [147] and, have been used as a tool to explore nonlinear plasma processes [148] and plasma self organisation [149].

2.2.2 Fireball Formation and Sustainment

When an electrode is biased positively with respect to the chamber walls, there exists a multitude of potential structures that can exist near the biased electrode (ion, electron and double sheath, anode glow and fireball [128]). Plasma sheaths form near plasma boundaries, where the plasma self-organises to balance the loss of ions and electrons from the bulk. Non neutral regions form, (quasineutrality is broken) separating the bulk quasineutral plasma from a boundary, shielding the bulk from any charge perturbation. Plasma sheaths can either be ion or electron rich. Ion sheaths form to reduce the flux of electrons leaving the bulk plasma and electron sheaths act to repel the ion flux. As previously discussed in low temperature plasma devices, electrons are more mobile than the much heavier ions, thus ion sheaths are most common in these devices. Electron sheaths can occur near a positively biased object if it's area is small [128]. A well know example of this is found in the electron saturation region of a Langmuir probe trace [150].

Fireballs form due to the build up of a thin region of positive space charge that develops in an electron sheath, formed by a localised increase in ionisation from sheath accelerated electrons. Once the space charge has built up to a high level, the plasma bifurcates into the much larger fireball state with a double layer defining it's edge. The fireball is a quasineutral plasma with the potential drop over the double layer being roughly the ionisation energy of the background gas [142, 151], which spans over several Debye lengths. Fireballs increase the effective collection area of an electrode, resulting in an increase of plasma potential. In the literature, there has been several proposed mechanisms on fireball onset, all of which rely on basic flux balancing over the double layer structure, known as the Langmuir condition [117, 152]:

$$\Gamma_i = \sqrt{\frac{m_e}{m_i}}\Gamma_e, \tag{2.5}$$

where $\Gamma_i = n_i V_i$ and $\Gamma_e = n_e V_e$ are the ion and electron flux densities at the double layer boundary respectively. Song et al [151] considered the transition from an anode glow to the onset of the luminous fireball state. Using equation 2.5, balancing loss and ionisation rates,

they showed that the critical bias for the transition is inversely proportional to operating pressure, which was shown to be true from experiments. They stated that fireball onset occurs when the ion density in the high potential side of the visual anode glow is larger than the bulk plasma density. Further work [152] considered sheath expansion effects, which increased the effective surface area of the electrode. From the modified criterion, in agreement with experiments, either an increase in pressure or electrode bias can result in the transition from an anode glow to a fireball. It has been suggested that, when the quasineutral region of an anode glow reaches the order of a Debye length, a fireball forms [142]. In this scenario, ions leaving the quasineutral plasma must satisfy the Bohm criterion, and thus a pre-sheath is established. The fireball was suggested to be the pre-sheath region. 2D PIC simulations [152], revealed that during the transition from anode glow to fireball, ion density is greater than the electron density close to the electrode. A build up of ion concentration near the electrode due to electron impact ionisation, results in a positive space charge layer that necessitates the trapping of low energy electrons. The positive space charge acts as a potential well for electrons and their concentration in this region increases. As the concentrations of ions and electrons begin to equalise, a quasineutral fireball plasma is formed. Later work using non perturbing laser-based measurements confirmed the simulations [153].

Different sheath structures have been found connecting the quasineutral fireball to the electrode: electron sheath, ion sheath and double sheath have all been reported (see review [128] and references therein). Considerations of current balance to the electrode and through the double layered fireball edge, reveals the conditions in which each sheath structure can be expected to form. If an ion sheath is present, ions are lost both to the electrode and through the double layer. The condition for an ion sheath with a fireball surface area, A_F and electrode surface area, A_E is given by [128, 152]:

$$\frac{A_E}{A_F} >\approx 1.7\sqrt{\frac{T_{el}}{T_e}}\mu, \tag{2.6}$$

where T_e is the total electron temperature and T_{el} is the trapped electron temperature. An electron sheath occurs when $\frac{A_E}{A_F}$ is small:

$$\frac{A_E}{A_F} <\approx \sqrt{2.3\frac{m_e}{m_i}}, \tag{2.7}$$

where m_e and m_i are the electron and ion masses respectively. For an electron sheath

to be present, the plasma potential should be less than the potential of the electrode. This results in electron loss to the electrode at their corresponding thermal speed and ions are lost through the fireball double layer at their sound speed. In the range of equations 2.6 and 2.7, a double sheath is possible. The author is referred again to review [128] for further fireball literature on experiments and simulations relating to fireballs. The rest of this section reviews the relevant literature of fireballs in magnetron devices.

2.2.3 Fireballs in Magnetron Discharges

To the authors knowledge, there has been only a few reports on fireball formation in magnetron sputtering devices [126, 154, 155], each of which have used a DC power source with reversed terminal connections to the conventional magnetron sputtering source. Unlike standard operation in magnetron sputtering, the cathode and anode polarities are switched and the target becomes the anode. In this configuration, the target acts as a sink of electrons rather than a source, with the magnetic field guiding their path to the anode. It has been reported that a visible glow can appear at both poles of the magnetron [154], at the centre pole and at the edges of the device. Similar fireball-like structures have also been observed by Stranak et al [156] during dual magnetron sputtering using time-resolved optical imaging. Each target was alternatively pulsed, acting as either cathode or anode. During operation, close to the magnetron with grounded cathode (anode), a bright central column of light was imaged. In these configurations, electrons created far away from the target, produced at the cathode, are unable to reach the racetrack region inside the magnetic trap. This gives the fireball a unique shape as the discharge is heavily moulded by the magnetic field lines of the magnetron device.

The magnetic field not only shapes the discharge, but is crucial for fireball production in a magnetron. The magnetic field structure constricts the anode surface area, yielding the right conditions for an electron sheath and double layer to form, which ultimately enables a fireball to exist on the anode. Electron sheaths occur when bulk plasma potential is below the anode potential. Chauhan et al [126] summarised different conditions which determines what type of sheath would be present. They consider the relation between discharge current, (I_D) and the electron saturation current (I_{es}) to the anode. Where I_{es} is given by:

$$I_{es} = \frac{Aen_e}{4}\sqrt{\frac{8k_BT_e}{\pi m_e}} \tag{2.8}$$

Where A is the area of the anode. If I_D is larger than I_{es} then an electron sheath emerges that increases the collection area of the anode similarly to the sheath expansion found in Langmuir probe operation at high voltage sweeps. The criterion for electron, ion and no sheath is summarised below, taken from [126]:

$$I_{es} > I_D \qquad \text{Ion sheath,} \tag{2.9a}$$

$$I_{es} = I_D \qquad \text{No sheath,} \tag{2.9b}$$

$$I_{es} < I_D \qquad \text{Electron sheath.} \tag{2.9c}$$

Chauhan makes the point that equation 2.9c is not readily satisfied for their magnetron system as the target anode is relatively large (75 mm in diameter). They state, that the actual collection area is much smaller that the entire area of the anode due to the magnetic field. This allows an electron sheath to form in their system. Equations 2.9 only accounts for electron current. Baalurd et al [127] considered both electron and ion currents in a simplified system, where ions and electrons are lost from the bulk plasma to their own respective surface. Here the condition for an electron sheath is found from:

$$\frac{A_e}{A_w} < \mu \tag{2.10}$$

Where, A_e is the area in which electrons are collected, A_w is the area ions are collected and μ is equal to $\sqrt{2.3\frac{m_e}{m_i}}$. In a magnetron system, A_w is the chamber wall area and A_e is the area of the anode (or constricted anode area).

In the same work, Chauhan et al, used an emisisve probe to measure the plasma potential across the visible glow (fireball) in their system and found a double layer. At the boundary of the glow, a potential difference of 15.6 V was found, corresponding to the ionisation energy of the background argon gas. It is this mechanism that sustained the fireball glow. In their system, the fireball was imaged at lengths of up to $\sim$ 12 cm. Figure 2.10 shows images of observed fireballs in a magnetron sputtering device, reproduced from reference [126].

2.2.4 Summary

Fireballs are impressive examples of plasma self organisation and have been observed in many different plasma devices. They occur near positively biased electrodes when the

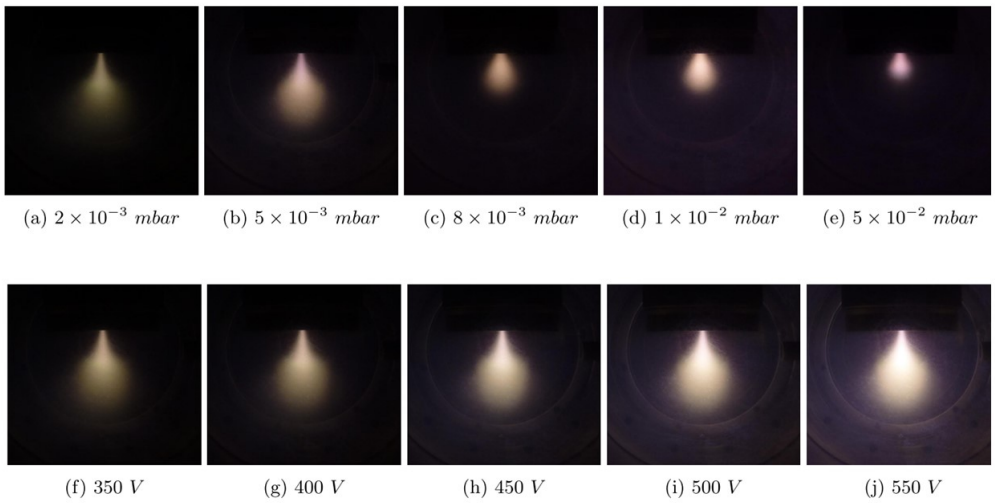

Figure 2.10: Observed fireballs in a magnetron device, reproduced from [126]. The top row indicates discharges produced at a constant + 300 V and the bottom row shows voltage dependence at constant pressure.

electrode bias is greater than the bulk plasma potential. A double layer separates the boundary of the fireball from the bulk plasma, with the visual glow spanning 100s of Debye lengths from the biased electrode. With regards to magnetron sputtering systems, they are possible due to the magnetic field configuration lowering the effective area of the target, constricting the anode surface area. This consequently produces an electron sheath and double layer in the system, which would not have been possible for the relatively large targets used for magnetron sputtering discharges. Operation in this regime is very different to conventional magnetron use, as the target polarity is positive (anode) in appose to negative (cathode). The target is no longer sputtered from impinging ions and acts as an electron sink. The magnetic field gives the fireball a unique shape, yielding a large droplet shaped glow extending from the target (anode) surface with electrons attracted to the poles. From the literature, it was found that the fireballs visual glow can extend up to 12 cm in length from the anode. Fireballs created in a magnetron system have been used to fabricate nanodot patterns [154] and used for ion implantation [155].

2.3 Incoherent Laser Thomson Scattering

In this research, the main diagnostic used was incoherent laser Thomson scattering (LTS), to measure electron temperature and density. This section reviews the relevant practical aspects of the literature that are most applicable to the work in this research. For greater detail in application and theory, the reader is referred to such reviews as [157, 158]. The section includes: a brief description of the technique and some of it's prevalent history, details on the scattered spectrum, the challenges faced when applying Thomson scattering to low density plasma sources and the design considerations relevant to this work. This section focuses on practical specifics, introducing the technique, whereas, background theory is presented in chapter 3.

2.3.1 Introduction

The phenomenon known as Thomson scattering (TS), named after Joseph Thomson, following his theoretical work [159] in the 20^{th} century, explains the scattering of electromagnetic (EM) radiation from free electrons. It is the lower energy limit of Compton scattering where an EM wave is scattered from a charged particle and both the change in electron and photon energy is negligible [158]. The incoming EM wave is scattered elastically, where only the direction of the scattered wave is changed in reference to the incoming wave and, if the scattering particle is in motion, the resultant scattering EM wave is Doppler shifted. If the scattering is incoherent (see section 3.2) such that; as is the case in this research, the EM radiation scatters off of many free charged particles, a resultant spectrum gives information about the velocity distribution of the particles in one dimension and thus their energy distribution. Furthermore, a scattering spectrum yields information on the densities of these charged particles, as a more intense signal the greater the number of scattering events and hence charged particles. TS is a non intrusive diagnostic tool with simple data interpretation and analysis with high temporal and spatial resolutions, making it a very useful diagnostic tool to measure plasma properties.

Incoherent Thomson scattering (ITS) has been utilised for electron temperature, T_e and electron density, n_e measurements for decades on fusion plasma devices where a very dense (bulk plasma $n_e > 10^{19} m^{-3}$) is present, utilising very high powered lasers. The popularity of Thomson scattering can be traced back to 1969, where Peacock et al [160] used the technique to confirm the high performance of T-3 tokamak. Since then, TS has been a prevalent diagnostic in nuclear fusion devices and is referred to by some as the

"gold standard" for electron property measurements. To this date, TS is still used and it's advancement has allowed lower density regions (divertor plasma $n_e > 10^{18} m^{-3}$) of modern tokamaks to be measured [161]. The cross section for Thomson scattering is relatively low[3] and in low temperature laboratory plasmas, with relatively low electron density, few scattering events occur, leading to a weak signal. Another difficulty arises when measuring low electron temperatures, as the spectral width of the scattering spectrum is relatively small, leading to stray light issues (see section 4.2.1). The combination of dense plasmas and high powered lasers in fusion experiments, means single shot laser pulses can provide enough scattering signal for electron property measurement. The invention of the ruby and Nd:YAG lasers in the early 1960's [162] yielded the first suitable lights source for Thomson scattering systems and attempts of LTS measurements at lower temperature plasmas became a reality in the late 1970's (see for example the review [157]). Since then, the advancements in detector technology and increased availability of pulsed lasers have allowed the technique to be extended to many different plasma sources such as: electron cyclotron resonance plasmas [163], inductively couple plasma (ICP) [164, 165], glow discharges [166, 167], microwave-induced plasmas [168], helicon plasma sources [169], plasma jets [170, 171] and recently, magnetron discharges [100–103].

It is clear that for typical low temperature, laboratory plasmas with low plasma density, there are several issues arise that need to be accounted for. These are detailed in [172] for the more general low density plasma source, whereas the following description is focused on the specific experimental source in this work. To overcome the issues requires:

- Appropriately powered radiation source
- High spectral resolution spectrometer
- High sensitivity detector
- Stray light reduction
- Data accumulation methods

[3]The Thomson scattering cross section is ~ 2 orders of magnitude higher than other scattering events such as Rayleigh scattering (see section 3.1) meaning that the fewer scattering events due to low density is the dominating factor in the weak Thomson signal

2.3.2 A Typical Spectrum

What has not yet been fully considered is that a TS signal is not the only signal that can be detected, nor is it the most prominent. Several other scattering events and redistribution of EM radiation occurs when a laser is introduced into a plasma, including Rayleigh scattering (RS) and stray laser light. Further more, the plasma itself will be emitting EM radiation corresponding to the emission lines of the particular composition of plasma and it's constituting process gas. The best way to describe these contributions is by looking a typical spectrum from this research. This is shown in figure 2.11 and discussed in the subsequent text.

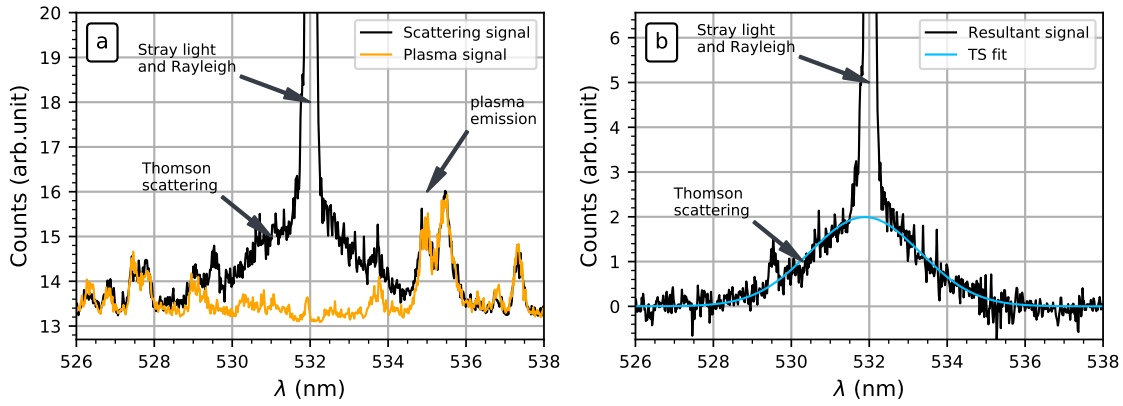

Figure 2.11: (a) Total spectrum example, acquired from an experiment in this work. Plotted are two signals: one showing the total spectrum including, plasma emission, stray light, Rayleigh scattering and Thomson scattering and the other showing the plasma emssion only. (b) The resultant spectrum after the plasma emission has been taken away, revealing the wings of Thomson scattering signal. Also shown is the Thomson scattering fit.

- **Thomson scattering** - *The signal to isolate.* This signal arises from the laser scattering off of free electrons in the plasma and is weak due to the processes low cross section. A simple calculation performed by Muraoka et al [157] shows that the number of TS photons typically detected is of the order $10^{-17} \cdot n_e \ [m^{-3}]$, thus for a typical experiment performed in this thesis, of the order $10^{16} - 10^{19} \ m^{-3}$ the intensity is weak and data accumulation methods needed to be introduced. For reference, in this work, the maximum and minimum electron temperatures measured are 0.12 eV and $\sim$ 3 eV respectively. The 1/e half width of these spectra are $\sim$ 0.5 nm and $\sim$

2.6 nm.

- **Rayleigh scattering** - *An unwanted signal when isolating TS, but is utilised later for calibration purposes.* This signal arises from the elastic, incoherent laser scattering of bound electrons in ions and atoms and can dominate in intensity. The scattering electrons are bound to heavy atoms and as such are moving relatively slow in comparison to the free electrons, this gives a much smaller Doppler broadening and thus a much smaller 1/e half width. For room temperature argon gas, the 1/e half width broadening effect is $\sim$ 1pm and is often below the spectral resolution of a typical TS detection system. This results in other sources of broadening being more dominant, such as the convolution of the instrument function and the laser line width.

- **Plasma emission** - *An unavoidable consequence of working with plasmas, yielding a large source of noise.* This signal arises when atoms or ions are excited and dexcited inside a plasma and produces not only line emissions, but a continuum over all wavelengths. Careful consideration of either the materials and process gas used or the laser wavelength needs to be made to ensure that there are minimal dominating line emission near the laser wavelength. The emission is a large contributor to the noise on the TS spectrum. The resultant plasma emission needs to be subtracted from the TS signal to isolate the TS signal, this is done by taking a plasma only measurement, with no laser incident on the plasma medium. This is shown in figure 2.11.

- **Stray laser light** - *Detrimental to Thomson scattering acquisition, dominating in intensity.* This signal arises from a small percentage of dispersed laser light as the laser travels through the optics. The most significant and notable contribution is laser light entering and exiting the system, this light passes through the chamber windows and reflects inside the vacuum vessel until finally it enters the detection system. As aforementioned, the Rayleigh Doppler broadening is virtually negligible and as such the stray light signals and the Rayleigh directly overlap and for low pressure, (of the order a few Pa) the stray laser light dominates over the Rayleigh contribution. Stray light can be a major issue in TS experiments due to both the small TS cross section and the large number of photons entering the system per laser pulse (of the order 10^{17}). The less dense the plasma, the more stray light dominates in its relative

contribution to the detection system. Figure 2.11, highlights how strong the stray light signal can be in comparison to the much weaker TS signal, with its intensity, peaking outside the figure plot.

.

2.3.3 Experimental Design Considerations

Laser Thomson scattering experiments on laboratory plasmas were initially limited to very dense plasmas, such as those created inside tokamaks. In these devices, single shot laser pulses were sufficient in yielding enough scattering signal for measurement. For low density and temperature plasma sources, laser induced perturbation (see section 4.2.6) effects can be more prominent and as such, using very high powered lasers to enable single shot acquisition is not beneficial. A data accumulation method, averaging over many laser pulses is required to lower the detection limit and several other adaptations are needed which are discussed below.

For an ideal detector in a Thomson scattering experiment, the signal-to-noise ratio (SNR) is effectively modelled by the shot noise from the detection of both the number of Thomson scattering (N_{TS}) and plasma emission (N_e) photons [167, 173], and is given by:

$$SNR \approx \frac{N_{TS}}{\sqrt{N_{TS} + 2N_E}} \tag{2.11}$$

Here the factor 2 encompasses the plasma emission, contributing both to the background measurement and the Thomson measurement (I.e with laser off and on) [174, p. 60]. It is clear that N_{TS} needs to be maximised compared to N_E. This is achieved by using pulsed lasers with moderate power and high repetition rate. The most frequently used radiation source used over the years has been the Nd:YAG, firing at it's second harmonic wavelength of 532 nm. This coupled with detectors that can be gated, only acquiring data when the laser pulse is firing, and that generates minimal amounts of noise over the acquisition period, increases the signal to noise ratio.

Scattered light is usually collected at 90° to both laser propagation and polarisation in order to maximise the cross section for TS, and it is efficient to use a collection lens to focus light into a spectrometer, rather than using an optical fibre which would suffer from losses. Grating spectrometers are used to separate the resultant spectrum into it's separate wavelengths and are detected using either photomultiplier or an intensified charge-couple

device (iCCD) [157]. As aforementioned, stray light is big issue in the design of a TS experiment and it's main source usually occurs at entrances and exits of the vessel. This can be somewhat mitigated by having long extensions to the chamber, where the light enters and exits far away from the plasma, with baffles in place to stop the dispersed light from travelling into the detection volume. The use of a viewing dump in the field of view of the collection lens would further reduce the stray light contribution.

All this considered, stray light may still dominate the TS signal and during data accumulation, may over-saturate the detector before sufficient TS signal is acquired. Either a double or triple grating spectrometer (TGS) is used to attenuate stray light. A TGS, uses a physical mask to remove the central laser wavelength and it has been found that the combination of a TGS and iCCD can produce very high levels of stray light rejection [175]. An innovative design, that provided a compact LTS system was first implemented in 2018 by Vincent et al. [176], used a narrow Bragg grating notch filter to attenuate stray light, coupled with an iCCD camera and single spectrometer. This system in comparison to those using a TGS, is much more concise and reduces transmission losses as there are fewer optical components.

The SNR can be improved further by comparing the signal at a detector to an externally set threshold, in a method called photon counting [167]. This would distinguish between noise generated in a detector and a true photon reading. A final way to improve the SNR would be to use a linear polariser, placed just before the entrance of the detector, polarised in the same plane as the incoming laser beam, whereas the plasma emission will have random polarisation and hence, reduced transmission through the filter.

2.3.4 Summary

Incoherent laser Thomson scattering has been used in fusion plasmas for the past 50 years, providing accurate, high fidelity, electron temperature, electron density and EVDF measurements. Advancements in lasers and detectors have made LTS measurements on low temperature, low density plasmas a reality. LTS can provide high spatial and temporal resolution measurements, with straightforward data interpretation and is non-intrusive. TS is not the only signal that would be present in a TS experiment and due to stray light domination, complicated and expensive equipment is required to make an LTS system that can suppress its contribution to the signal. Several experimental considerations to increase the SNR have been reviewed. A final note is that the magnetron sputtering system used,

deposits material onto the viewing ports which accumulates and reduces transmission of the signal. Therefore, careful consideration of data acquisition and accumulation times needs to be considered.

2.4 Emissive Probe

An emissive probe (EP) was used in this work to measure and track plasma potential (V_P). This section aims to introduce the technique and review the practical aspects that are required to accurately track plasma potential. The author refers the reader to the review [177], for a detailed historical review of EP's and the different methods used to obtain V_p. The experimental apparatus and procedure used in this work is described in section 4.3.

2.4.1 Introduction

Langmuir proposed the idea of an electron-emitting probe (EP) in 1923 when he first proposed the collecting probe [178]. Collecting probes such as the single LP can measure V_p by finding the "knee" of the IV curve, or by finding the inflection point by differentiating the I-V curve [150]. However, this can be unreliable when there is significant rounding of the knee, for example due to magnetic field effects [179]. Another downside of LP determination of V_p, is the requirement to sweep the voltage applied to the probe to create the I-V characteristic, such that fast changes in V_p cannot be resolved. EP's on the other hand can measure V_p down to 0.1 T_e [180]. An EP usually utilises the heating of a thin wire, whereby electrons are emitted from the wire into the plasma and the emitted electron current is described by the Richard-Dushman equation [177]. Basically, if an EP is biased more positively than V_p, then only a small number of high energy electrons can be released from the probe with the predominant proportion unable to be emitted. If the probe is biased more negatively than the plasma potential, then the probe begins to emit electrons. The releasing of electrons in the plasma allows local potentials to be measured and with sufficient electron release, the probe voltage tends to V_p.

2.4.2 Techniques

There exists 3 main methods of determining V_p from an EP experiment in literature, namely: (1) The separation technique, originally developed by Langmuir [178] involves

finding the point of separation of superimposed I-V curves of cold and warm (emitting) probes. This technique was found to be unreliable, in part due to space charge effects around the emissive probe, as it releases electrons into the plasma and surface contamination of the cold probe [181]. (2) The saturated floating method, first established by Kemp and Sellen in 1966 [182], relies on the EP tip being isolated from ground potential, such that it sits at the plasma floating potential V_F ($I_p = 0$). When the tip is heated, the potential of the EP increases, approaching V_p and saturates. The point at which V_F saturates is said to be the plasma potential however, in reality, a truly saturated relationship does not exist due to sheath expansion at higher heating currents. It has been found that EP's using the floating method, typically measure 1 - 1.5 T_e below the plasma potential [181, 183, 184]. The most advantageous property of this type of measurement is that once the probe is identified to be floating at saturation, the method can accurately track temporal and spatial fluctuations in V_p with minimal perturbation/disturbance to the plasma (unlike the separation technique which requires a voltage sweep). (3) The inflection point method introduced by Smith et al [185], involves taking a range of several I-V curves of weak emission and finding the peaks of the first derivative. The peaks at the differing emission levels are plotted against the potential and are extrapolated to zero emission to find V_p and was found to underestimate V_p by 0.1 T_e [183]. It should be noted that EP's can also be used to measure T_e [177], but is beyond the scope of this thesis.

2.4.3 Summary

Emissive probes are a robust and reliable tool to accurately measure plasma potential and fast plasma potential changes in plasma devices. There exists several techniques for extracting V_p with differing accuracy's and complexities. In this work, the floating point method (2) was used due to it's ease of implementation, it's excellent ability to track quick plasma potential changes and, compared to the other techniques, causes minimal disturbance to the plasma as (in theory) no net current is collected. The floating point method has been used to measure V_p in many plasma devices such as magnetrons [35] and fusion devices [186]. Thoriated tungsten is the typical material used for the wire tip, due to it's high melting point and is typically heated through Joule heating by passing a current through a closed looped. In typical magnetron experiments, heating of the wire is achieved by use of mains supply, with a variable and fixed transformer combination, for example [35]. The variable transformer is connected directly to the mains supply,

and is used to step up the current, whilst stepping down the voltage. The second fixed transformer isolates the probe from ground and a centre tap is used, in conjunction with a voltage probe that measures the floating potential of the probe. By adjusting the variable transformer, current can be delivered to the probe. This type of EP system is used in this work.

It should be noted that in this work, the raw floating voltage measurements were taken as V_p. As previously mentioned, the floating potential of an emitting probe typically measures $\sim T_e$ below the plasma potential. The exact deviation is dependant on the EEDF of the plasma, the probe emission and the surrounding sheath [180]. Correction would also require separate measurement of T_e. The deviation is also further complicated in this work due to the magnetic field of the magnetron (see section 4.3.3). For these reasons, and the fact that the measured plasma potential in this work is much larger than the electron temperature, no attempts at correcting the measured values were performed. Details of the specific system, design and implementation is given in section 4.3.

Chapter 3

Laser Thomson Scattering Theory

In this research, Bipolar HiPIMS discharges were measured using incoherent laser Thomson scattering (LTS), with a focus on electron properties during the positive afterglow. The purpose of this chapter is to describe the theory behind the technique, and how electron properties were extracted from a measured scattering spectrum. The reader is referred to the book written by Sheffield [187] for a complete description of this phenomenon.

3.1 Electromagnetic Scattering from an Electron

The elastic scattering of electromagnetic waves from free electrons (in a plasma) is called Thomson scattering and is described through classical electromagnetism (EM). A laser producing a linear polarised, monochromatic plane wave propagating along a unit vector e_e, towards an electron in time t has the form:

$$\mathbf{E_i}(x,t) = \mathbf{E_0}\exp[i(\mathbf{k_i}\cdot\mathbf{x} - \omega_i t)]. \tag{3.1}$$

Defining the quantities in equation 3.1 as $\mathbf{E_0} = E_0\mathbf{e_0}$, the vector amplitude of magnitude E_0 in the $\mathbf{e_0}$ direction. The wavelength of the wave as $\lambda_i = 2\pi c/w_i$ with c being the speed of light and w_i the angular frequency, then the wavevector is defined as $k_i\mathbf{e_i} = 2\pi\mathbf{e_i}/\lambda_i$. Two Doppler shifts are present due to the oscillating motion of the electrons in the presence of an electric field, producing electric-dipole radiation. The first of which comes from considering the motion of an electron in it's rest frame [174], and it's velocity component

$\mathbf{v}$ in the direction of the laser:

$$\omega_e = \omega_i - \mathbf{k_i} \cdot \mathbf{v}. \tag{3.2}$$

Here, the scattered radiation wavevector originating from the electron's position is $\mathbf{k_e} = 2\pi\mathbf{e_s}/\lambda_e$ and $\lambda_e = 2\pi c/\omega_e$ with $\mathbf{e_s}$ in the direction of an observer.

The second shift arises from the measured angular frequency in the laboratory frame due to the velocity component in the direction of the observer:

$$\omega_s = \omega_e + \mathbf{k_s} \cdot \mathbf{v}. \tag{3.3}$$

Here, the scattered wavevector originating from the electron's position measured in the lab frame by an observer is $\mathbf{k_s} = 2\pi\mathbf{e_s}/\lambda_s$ and $\lambda_s = 2\pi c/\omega_s$ with $\mathbf{e_s}$ is in the direction of an observer.

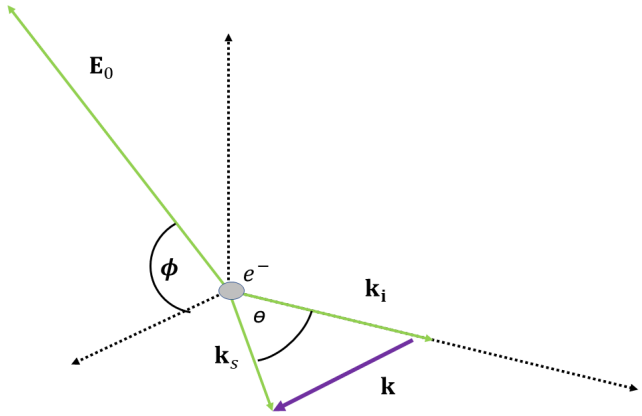

Figure 3.1: The scattering geometry, showing the incident wavevector $\mathbf{k_i}$ and scattered wavevector $\mathbf{k_s}$ from the electron's position at the origin. θ is the scattering angle and ϕ is the angle between the polarisation and the plane of scattering.

The contributions of both Doppler shifts relative to the scattering vector $\mathbf{k}$, is defined by:

$$\mathbf{k} \equiv \mathbf{k_s} - \mathbf{k_i}, \tag{3.4}$$

where $\mathbf{k_s}$ and $\mathbf{k_i}$ are defined figure 3.1.

The resultant angular frequency shift of the scattered laser waves from the scattering process can be written as:

$$\Delta\omega = \omega_s - \omega_i = \mathbf{k} \cdot \mathbf{v} = kv_k, \tag{3.5}$$

where v_k is the velocity component in the $\mathbf{k}$ direction. The magnitude of $\mathbf{k}$ can be found by considering two perpendicular components, parallel and perpendicular to $\mathbf{k_i}$ and using the fact that $\lambda_i \approx \lambda_s$ for $v_k \ll c$. This leads to:

$$k \approx |\mathbf{k}| = \sqrt{2}k_i\sqrt{1 - cos\theta}^1 = 2k_i sin\frac{\theta}{2}. \tag{3.6}$$

Equation 3.5 can also be transformed into the more accessible wavelength shift ($\Delta\lambda = \lambda_s - \lambda_i$) which has the form:

$$\Delta\lambda \approx \frac{-\lambda_i^2 k v_k}{2\pi c}. \tag{3.7}$$

Equations 3.6 and 3.7 shows that the scattered light frequency shift is dependent on the one dimensional component of the electron's total velocity with respect to the scattering geometry and the incident wavelength of the incoming EM wave. If the scattered waves follow the assumptions of incoherent scattering (see section 3.2), where the scattered waves do not bare a phase relationship and interference effects can be ignored, the frequency distribution of scattered waves is directly related to the velocity distribution in the $\mathbf{k}$ (scattering vector) direction.

The scattered radiation is distributed analogous to that of a radiating dipole [174]. It is rotationally symmetric around the dipole axis, with it's greatest intensity perpendicular to this axis and no radiation emitted along the dipole axis. The differential cross section for Thomson scattering can be written as:

$$\frac{\mathrm{d}\sigma_{\mathrm{TS}}}{\mathrm{d}\Omega} = r_{ce}^2(1 - \sin^2\theta\cos^2\phi), \tag{3.8}$$

where r_{ce} is the classical electron radius of 2.818 x 10^{-15} m and the definitions of ϕ and θ are shown in figure 3.1. The maximum power radiated and hence the greatest cross section occurs when $\mathbf{k}$ is perpendicular to $\mathbf{E_0}$. Mathematically this occurs when $\phi = \pi/2, 3\pi/2...$ and/or when $\theta = 0,\pi...$ Physically however the maximum at $\theta = 0$ does

[1] Here the fact that $(1 - cos\theta)/2 = sin^2(\theta/2)$ has been used.

not occur, as this corresponds to $\mathbf{k} = 0$, as there is no scattered radiation along the dipole axis. This then leads to the maximum differential cross section, $\frac{\mathrm{d}\sigma_{\mathrm{TS}}}{\mathrm{d}\Omega} = r_{ce}^2 \cdot 1 = 7.941$ x $10^{-30} m^2$. This value is small and as such, powerful lasers and sophisticated, expensive equipment are needed to produce the scattering beam and collect the scattered light.

Finally one will consider the electric field at the observers position created from a single scattering event from a single electron and the corresponding polarisation of the scattered wave.

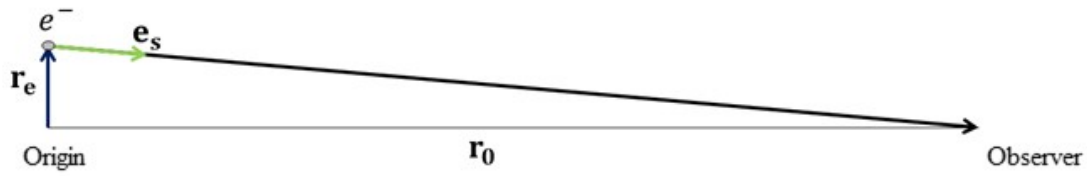

Figure 3.2: The far field configuration where $|\mathbf{r_e}| = r_e \ll |\mathbf{r_0}| = r_0$. The observer ($\mathbf{r_0}$), the electron $e^-(\mathbf{r_e})$ position vectors and the scattering unit vector ($\mathbf{e_s}$) are labelled.

In the far field configuration (see figure 3.2), the electric field has the form:

$$\mathbf{E_s} = \mathbf{E_{s0}} \exp[i(k_s r_0 - \omega_s t - \mathbf{k} \cdot \mathbf{r_e}(t = 0)], \tag{3.9}$$

Where $\mathbf{E_{s0}} = E_{s0}[\mathbf{e_s} \times (\mathbf{e_s} \times \mathbf{e_0})]$, $\mathbf{r_e}(t = 0)$ is the radial distance vector to the electrons position from the origin at the start of the scattering event, and r_0 is the distance from the origin to the observer. The polarisation state is linear and the use of a linear polariser is beneficial in an experimental set up to block the collection of unpolarised noise signals but allow the transmission of the polarised Thomson signal.

3.2 Coherent and Incoherent Scattering

The scattered radiation in a plasma due to free charged particles is predominately caused by electrons as these have much smaller mass and are accelerated considerably more than the much heavier ions by the electric field. When there are multiple electrons or a collection of them (as is the case in a plasma), the density fluctuations are what determine the spectrum and the intensities of the scattered light. The total electric field due to multiple electrons in the Thomson scattering process is the superposition of all the individual waves and intuitively, the total power of the scattered light is the modulus squared of the summation

of the individual electric fields given by equation 3.9. The average scattered power per unit area (Poynting vector) has two contributions to its time averaged magnitude [158], given by:

$$|\langle \mathbf{S} \rangle| = \underbrace{N|\langle \mathbf{S}_{single} \rangle|}_{incoherent} + \underbrace{c\epsilon_0 \left\langle \sum_i^N \mathbf{E}_{s,i} \cdot \sum_{j \neq i}^N \mathbf{E}_{s,j} \right\rangle}_{coherent}, \tag{3.10}$$

[188, p. 62], where the subscripts i, j represent the the scattered waves from each electron, ϵ_0 is the permitivity of free space, N is the total number of electrons in the volume and $|\langle \mathbf{S}_{single} \rangle| = c\epsilon_0 E_{s0}^2/2$ is the average power flux of a single radiating electron with scattered electric field given by equation 3.9. The incoherence term is the sum of the scattered power by each independent electron; in contrast, the coherence term includes the phase differences between scattered waves. The coherence term becomes zero if the electrons have random, uncorrelated positions but becomes important if the motion of the electrons are correlated and behave collectively.

Consider two scattered waves with wavelength λ_s at time t = 0, with electrons at initial positions, $\mathbf{r}_e$ and $\mathbf{r}_e + \Delta\mathbf{r}_e$ respectively, then the condition for total constructive interference occurs when the waves are separated by $2\pi n$ thus the scattered waves have the same phase when the electrons are separated by a distance of $2\pi/k$ along $\mathbf{k}$. If electron positions are correlated on this length scale, then coherent effects are introduced, however if electron positions are random within this length scale, then the scattering is incoherent as the phases of the scattered waves are random. The length scale $2\pi/k$ is a "sample length" over which coherence effects are probed [189].

The Debye length (λ_D) is the smallest correlation length scale in a plasma [158], determining the radius of the electron cloud surrounding positive ions. If:

- $2\pi/k \ll \lambda_D$, then the random positions of the electrons within the Debye sphere can be resolved, and the coherence term in equation 3.10 tends to zero. Therefore the scattering follows the **incoherent regime**.

- $2\pi/k \gg \lambda_D$, then the resolution is poor, and electron density fluctuations (i.e caused by waves in the plasma) cause the electron positions to be correlated. Therefore the scattering follows the **coherent regime** and the second term in equation 3.10 needs to be considered.

A common, useful way to quantify the coherent effect is the Salpeter parameter:

$$\alpha \equiv \frac{1}{k\lambda_D} \approx \frac{\lambda_i}{4\pi\lambda_D \sin\left(\frac{\theta}{2}\right)}, \tag{3.11}$$

For $\alpha \ll 1$ the incoherent regime holds and the scattering is uncorrelated. As α approaches values close to 1, then coherent effects are present and need to be accounted for. With $\theta = \frac{\pi}{2}$ and $\lambda_i = 532$ nm, α is proportional to the root of the electron density in the plasma and inversely proportional to the root of the electron temperature, through λ_D. For the highest density and lowest temperature combination measured in this study ($n_e \sim 10^{19}$ m^{-3} and $T_e \sim 1$ eV), α reaches a maximum of approximately 0.03. Therefore the assumption of an incoherent scattering spectrum was appropriate for the measurement's performed throughout the presented work in the subsequent chapters.

3.3 Incoherent Thomson Scattering Spectrum of a Maxwellian EEDF

The intensity and shape of the detected Thomson signal (in the incoherent regime) depends on the properties of the detection system and the density of the electrons in the plasma. If one considers the ideal case, where there is no transmission losses through the system and the detector is 100% efficient, meaning that all scattering events collected in the collection medium are equal to the total scattering events (in the collection medium), then the spectrum can be expressed as:

$$\begin{aligned} f_{N\lambda}(\lambda_S)d\lambda_s &= N_{TS_{ideal}} \cdot S(\lambda_s)d\lambda_s, \\ \text{with:} \qquad N_{TS_{ideal}} &= f_{(Hz)} t_i N_l L \frac{\mathrm{d}\sigma_{\mathrm{TS}}}{\mathrm{d}\Omega} \Delta\Omega \cdot n_e. \end{aligned} \tag{3.12}$$

Where $f_{(Hz)}$ is the frequency of the laser, t_i is the integration time (time of data collection), $N_l = \lambda_i P_i / hc f_{(Hz)}$ is the number of laser photons produced from the laser, L is the detection volume length, $\Delta\Omega$ is the collection solid angle and n_e is the electron density. The term $S(\lambda_s)d\lambda_s$ is included to represent the probability that a collected photon (λ_s) lies within the wavelength range $d\lambda_s$. It should be noted that in this treatment, the plasma is said to be optically thin and thus a photon undergoes one scattering event in the plasma.

If one now considers the term $S(\lambda_s)d\lambda_s$ and the shape of the scattered spectrum by

returning to equation 3.7, the change in wavelength is proportional to v_k (electron velocity along $\mathbf{k}$) it can be shown that:

$$v_k(\lambda_s) \approx \frac{-c\Delta\lambda}{2\lambda_i \sin\left(\frac{\theta}{2}\right)}. \tag{3.13}$$

Consequently, this means that the probability distribution is directly related to the electron velocity probability distribution (f_k), in the $\mathbf{k}$ direction:

$$S(\lambda_s)d\lambda_s = f_k \frac{dv_k}{d\lambda_s} d\lambda_s \approx \frac{-c}{2\lambda_i \sin\left(\frac{\theta}{2}\right)} \cdot f_k(\lambda_s)d\lambda_s. \tag{3.14}$$

Now, in terms of wavelength and photon number, the total expression for an ideal incoherent Thomson scattering spectrum is:

$$f_{N\lambda}(\lambda_S)d\lambda_s = f_{(Hz)} t_i N_l L \frac{\mathrm{d}\sigma_{\mathrm{TS}}}{\mathrm{d}\Omega} \Delta\Omega \cdot n_e \frac{-c}{2\lambda_i \sin\left(\frac{\theta}{2}\right)} \cdot f_k(\lambda_s)d\lambda_s. \tag{3.15}$$

3.3.1 Electron Temperature

As shown in the previous section, the spectral distribution has the same shape as the velocity distribution. In the case of a Maxwellian electron energy distribution function, the one-dimensional probability velocity distribution is:

$$f_k = \frac{1}{\hat{v}\sqrt{\pi}} \exp\left[-\left(\frac{v_k}{\hat{v}}\right)^2\right]. \tag{3.16}$$

Where:

$$\hat{v} = \sqrt{\frac{2k_B T_e}{m_e}}$$

is the most probable electron energy. Now substituting equation 3.13 into equation 3.16, f_k now becomes:

$$f_k = \frac{1}{\hat{v}\sqrt{\pi}} \exp\left[-\left(\frac{-\Delta\lambda c}{2\lambda_i \sin\left(\frac{\theta}{2}\right)\hat{v}}\right)^2\right]. \tag{3.17}$$

One can now define the 1/e half width of the spectrum by calculating $\Delta\lambda_{\frac{1}{e}} = \lambda_{\frac{1}{e}} - \lambda_i$

and calculating 1/e to be [2]:

$$\frac{1}{e} = \frac{f_k(\lambda_s = \lambda_{\frac{1}{e}})}{f_k(\lambda_s = \lambda_i)} = \exp\left[-\left(\frac{-\Delta\lambda_{\frac{1}{e}} c}{2\lambda_i \sin(\frac{\theta}{2})\hat{v}}\right)^2\right], \tag{3.18}$$

gives $\Delta\lambda_{\frac{1}{e}}$ as:

$$\Delta\lambda_{\frac{1}{e}} = \frac{\hat{v}}{c} \cdot 2\lambda_i \sin\left(\frac{\theta}{2}\right). \tag{3.19}$$

Rearranging, gives the electron temperature as:

$$T_e = \frac{m_e c^2}{8k_B sin^2(\frac{\theta}{2})} \cdot \left(\frac{\Delta\lambda_{\frac{1}{e}}}{\lambda_i}\right)^2, \tag{3.20}$$

where m_e is the electron mass, c is the speed of light, k_B is the Boltzmann constant, θ is the scattering angle, $\Delta\lambda_{\frac{1}{e}}$ is the $\frac{1}{e}$ half width of the spectrum and λ_i is the incident laser wavelength.

Now relating equation 3.20 to a Gaussian of the form:

$$y = A \cdot \exp\left(\frac{-(x-B)^2}{2C^2}\right), \tag{3.21}$$

where A is the amplitude of the curve, B is the centre offset and C is related to the width through standard deviation. Making θ equal to 90°, equation 3.20 reduces to:

$$T_e[eV] = \frac{m_e c^2}{2e} \cdot \left(\frac{C}{\lambda_i}\right)^2 \tag{3.22}$$

and the total number of counts at a detector is found from the area under the measured spectrum by:

$$N_{TS_{counts}} = AC\sqrt{2\pi} \tag{3.23}$$

3.3.2 Electron Density

This section now revisits the ideal spectrum derived in this chapter to relate the spectrum to the true number of counts measured. If the detector used in the experiment had a

[2] $\Delta\lambda = \lambda_s - \lambda_i$

quantum efficiency of 1 and the optics used to redirect, focus and collect the scattered light was ideal (no transmission losses) then:

$$\int_0^\infty f_{n\lambda}(\lambda_s)d\lambda_s = N_{TS_{ideal}}. \tag{3.24}$$

In reality, however the number of detected photons is much less than this and detectors often measure the scattered spectrum in terms of counts, which is hard to relate to actual photon numbers. To determine the electron density, one needs to account for this and a factor Z is introduced such that the spectrum equation in terms of counts now becomes:

$$f_{c\lambda}(\lambda_S)d\lambda_s = ZN_{TS_{ideal}} \cdot \frac{-c}{2\lambda_i \sin(\frac{\theta}{2})} \cdot f_k(\lambda_s)d\lambda_s, \tag{3.25}$$

and:

$$Z \equiv \frac{\int_0^\infty f_{c\lambda}(\lambda_S)d\lambda_s}{\int_0^\infty f_{n\lambda}(\lambda_S)d\lambda_s} = \frac{N_{TS_{counts}}}{N_{TS_{ideal}}} \tag{3.26}$$

Here Z is the ratio between the total detected counts of the system and the ideal number of photons collected for the ideal system. Hence a calibration needs to be done and in this research, this was done by Rayleigh scattering of room temperature argon.

Rayleigh scattering, similar to Thomson scattering, is the elastic scattering of electromagnetic radiation, but in this case it is the scattering from bound electrons in ions, molecules and atoms. The incoherent Rayleigh scattering spectrum is identical to the spectrum calculated in 3.25 however the Doppler broadening is much lower due to the heavier scattering species moving at much lower speeds relative to the free electrons in Thomson scattering. This has the form:

$$\begin{aligned} f_{R\lambda}(\lambda_S)d\lambda_s &= ZN_{RS_{ideal}} \cdot \frac{-c}{2\lambda_i \sin(\frac{\theta}{2})} \cdot f_{Rk}(\lambda_s)d\lambda_s, \\ \text{with:} \qquad N_{RS_{ideal}} &= f_{(Hz)}t_{Ri}N_{Rl}L\frac{\mathrm{d}\sigma_{\mathrm{RS}}}{\mathrm{d}\Omega}\Delta\Omega \cdot n_g. \end{aligned} \tag{3.27}$$

Where $f_{Rk}(\lambda_s)d\lambda_s$ is the one dimensional velocity probability distribution of the heavy species in the $\mathbf{k}$ direction, and $N_{RS_{ideal}}$ is the ideal total number of Rayleigh photons scattered from a gas of density n_g. $\frac{\mathrm{d}\sigma_{\mathrm{RS}}}{\mathrm{d}\Omega}\Delta\Omega$ is the differential cross section equal to 5.41 x $10^{-32}m^2$ and N_{Rl} is the number of photons per laser pulse for the Rayleigh scattering.

All other terms are identical to the Thomson scattering spectrum.

Finally, using equations 3.25 3.26, and 3.27 electron density can be determined through:

$$n_e = \frac{N_{TS_{counts}}}{N_{RS_{counts}}} \cdot \frac{N_{Rl}}{N_l} \cdot \frac{t_{Ri}}{t_i} \cdot \left(\frac{\frac{d\sigma_{RS}}{d\Omega}}{\frac{d\sigma_{TS}}{d\Omega}} \right) \cdot n_g. \tag{3.28}$$

The calibration procedure was to work out $\frac{N_{RS_{counts}}}{n_g}$, this was done by measuring the total Rayleigh scattering signal at different gas pressures (and therefore densities through the ideal gas law) and finding the gradient of counts as a function of gas pressure. Substituting all know values into equation 3.28 determines the total electron density in the measured plasma volume.

Chapter 4

Experimental Arrangement and Procedure

This chapter details the experimental arrangement, plasma source and diagnostics used. It gives a description of the experimental system, diagnostics and analysis procedures. The section is organised as follows : (1) a description of the magnetron system; (2) the Thomson scattering and optical emission systems, with experimental procedures explained; (3) the emissive probe system and experimental procedures; (4) the 2D imaging apparatus and procedures.

4.1 The Magnetron System for HiPIMS

This section introduces the magnetron sputtering system used throughout this work. It provides a description of the vacuum vessel, the magnetron, the magnetic field configuration and the power supplies used to create discharges either in a unipolar, or bipolar HiPIMS configuration. Figure 4.1 shows the schematic of the experimental set up, consisting of the magnetron and the integral parts of the Thomson scattering diagnostic. The magnetron used is a VTech 150 series unbalanced magnetron (Gencoa Ltd,UK) with a 150 mm diameter tungsten (99.95% purity) target mounted vertically with reference to the chamber floor. The anode of the magnetron surrounds the perimeter of the target and protruded ~ 7 mm above the target surface. The vertical position of the magnetron inside the vacuum chamber could be altered, allowing different positions to be measured by the diagnostic equipment. The chamber was evacuated to a base pressure of the order 10^{-3} Pa,

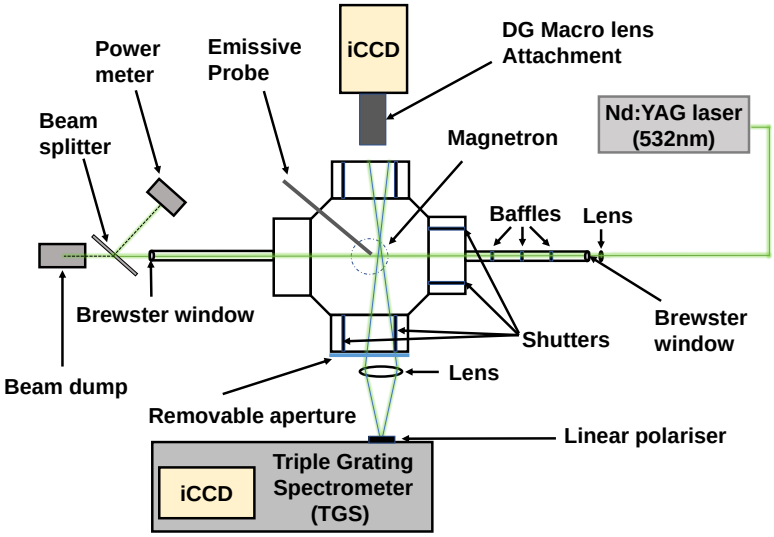

Figure 4.1: A Schematic of the experimental set up. Including: vacuum vessel, magnetron, Thomson scattering apparatus, emissive probe, secondary iCCD for imaging and removable aperture for OES measurements

using a combination of turbomolecular pump (Pfeiffer TMU071P) and a backing rotary pump (Edwards RV3). The pressure was measured using an inverted magnetron gauge (Edwards AIM-X). Argon gas of purity 99.998 % was supplied to the vacuum chamber using a mass flow controller (MKS 1179A). Three further pressure gauges were used, a capacitance manometer (MKS Baratron 627) measured the (low) argon gas pressure used when igniting and sustaining a plasma discharge, a capacitance manometer (MKS Baratron 626) measured the (higher) argon pressure used in the Rayleigh scattering data acquisition and a Pirani gauge measured the chamber pressure from atmospheric pressure, down to 1 x 10^{-2} Pa. The two Baratrons had ranges 1.33 x 10^{-3} to 1.33 x 10^{1} Pa and 1.33 x 10^{0} to 1.33 x 10^{4} Pa respectively.

The magnetic field of the magnetron is shown in figure 4.2, it is a slice of the magnetic configuration in the radial-height plane, showing the magnitude and direction of the field. To create this figure, a digital Gauss meter (Hirst GM04) was used in two configurations to create the resultant vector field shown. The noteworthy points in figure 4.2 is the location of the magnetic null and the main racetrack erosion (magnetic trap region), these were at r = 0 mm, z = 61 mm and r = 48 mm, z = 0 mm respectively.

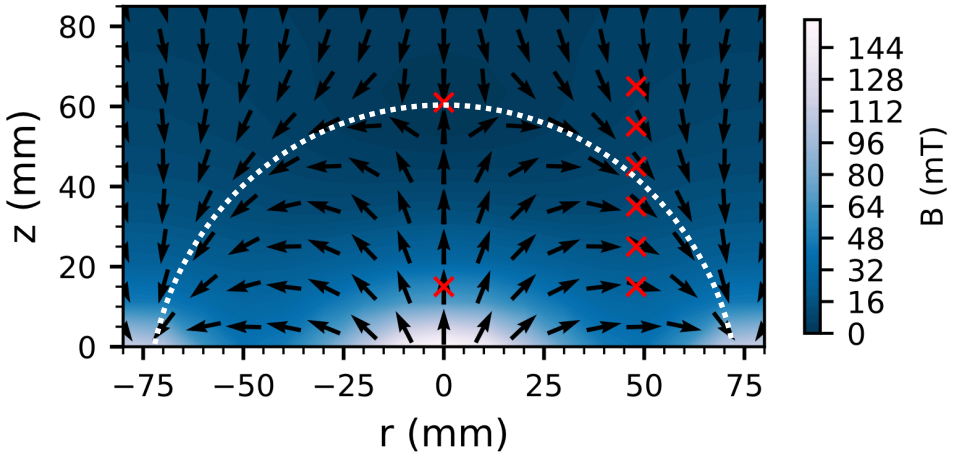

Figure 4.2: Measured magnetic field of the unbalanced planar magnetron. r is the radial direction parallel to the magnetron surface and z is the perpendicular distance from the magnetron. r = 0 is the centre of the target and z = 0 is the magnetron surface. The main race track erosion is located at z ∼ 48 mm and the magnetic null is located at r = 0 mm, z ∼ 61 mm. Plotted in red is the measurement positions made by LTS and in white is the last closed flux surface marking the boundary of the magnetic trap region.

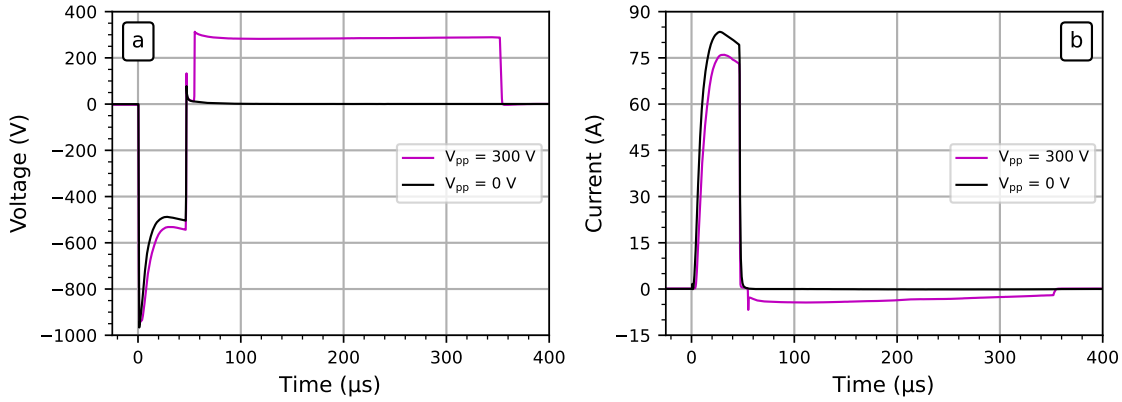

Figure 4.3: Example discharge voltage (a) and current (b) waveforms. The magenta curves represent a bipolar pulse with a 300 V magnitude positive pulse and black curves indicate a unipolar pulse.

Discharges were driven by an asymmetric bipolar HiPIMS power supply designed and built in house. It consisted of two synchronised generators, one for generating conventional negative voltage pulses (up to -1 kV) and the second for generating reverse polarity positive voltage pulses (up to + 350 V), delayed by 8 μs after termination of the former. The target voltage and current waveforms were measured using a 100x Tektronix P5100 voltage probe and a model 110 A Pearson current monitor respectively. Figure 4.3 shows example voltage and current waveforms for two example discharges created in this work: a unipolar HiPIMS pulse and a bipolar HiPIMS pulse with a 300 V positive pulse of length $t_{pp} = 300$ μs. In each case, an average pulse energy, power, and peak target power density of 1.8 J, 85 W and $\sim 230 \mathrm{Wcm}^{-2}$ were achieved. The discharges shown in figure 4.3 had a fixed repetition rate of 50 Hz and negative pulse length of $t_{np} = 50$ μs.

From figure 4.3, it is shown that, increasing the positive pulse voltage can increase the current rise time and reduce the peak current during the negative pulse (main sputtering phase). As will be shown later in the thesis, (see chapter 5) this may be due to lower residual electron densities being available in the afterglow to aid ignition of the next pulse, when large positive pulses are utilised. In the case shown in figure 4.3, reverse negative currents of up to 5 A to the cathode are generated for this particular positive pulse voltage. From here on in, the start of the negative pulse is defined to be t = 0 μs.

4.2 The Thomson Scattering and Optical Emission Spectroscopy System

Figure 4.1 shows the experimental arrangement and the apparatus used for the Laser Thomson Scattering (LTS) diagnostic system. It should be recognised that the experimental arrangement is mostly the same as that as used by a previous PhD student (Peter Ryan) and is detailed in their PhD thesis [188]. For completion, the system is described in full throughout this section. The system consisted of a Nd:YAG laser (532 nm), focusing lenses, baffles, brewster windows, shutters, linear polariser, Triple Grating Spectrometer (TGS) and an iCCD camera. The laser used was a Quantel Brilliant B, which operated at it's second harmonic wavelength of 532 nm. It supplied 200 - 250 mJ of energy per pulse as measured by laser power meter (Gentec-EO SOLO2) configured in a calibrated beam split. The beam was in the plane of the target surface and had a duration of 5 ns, beam divergence of 0.5 mrad and pulsed at 10 Hz. At the measurement position, the beam

diameter was 0.25 mm after being focused by a 1 m focal lens and its electric field was polarised perpendicular to the beam path.

A lens of diameter 75 mm and focal length of 200 mm and was positioned at a distance of 310 mm (see section 4.2.4) from the measurement position, at an angle of $\frac{\pi}{2}$ rad with respect to the laser polarisation and propagation. This lens collected the scattered photons from the measurement position and the angle $\frac{\pi}{2}$ rad was used in order to maximise the Thomson differential cross section (equation 3.8). The scattered light was then directed into a Triple Grating Spectrometer (TGS, Horiba T64000) at a distance of 564 mm see section (4.2.4) and was configured in the double-subtractive configuration to physically remove a small wavelength range around the laser wavelength, thus attenuating the stray light and Rayleigh signals. Therefore the central region of the resultant TS spectra is attenuated and only the wings of the spectrum can be used for data analysis (further details provided in section 4.2.5).

It is important to note, that due to the deposition from the magnetron sputtering system, material coated the inside of the chamber and any windows on the vacuum vessel. This was problematic for Thomson scattering signal acquisition. Increased deposition results in transmission loss through the window and hence decreased the intensity of the scattered light. This was countered by having mechanical shutters on the system, which were opened when a measurement was taken and closed in the meantime. Low-cost, removable soda glass windows were used and replaced periodically when transmission became too low for measurement.

The dispersed light was then collected by an intensified charged-coupled device (ICCD) camera (Andor iStar DH320T-18U-A3). The device recorded the incoming scattered light on an array of 1024 x 255 pixels where; the former records the wavelength of scattered light and the later is the spatial dimension. The range of the wavelength axis was determined by the grooves of the gratings in the TGS, these had 1800 groves/mm (more details in section 4.2.2), yielding a spectral range of 522.99 - 541.09 nm. To reveal the Thomson signal, data acquisition with and without the laser incident on the plasma was required to allow the background signal to be removed. The recorded iCCD images were integrated throughout data acquisition and only readout once per acquisition to reduce readout noise in the spectrum. The CCD was synchronised to the Q-switch of the laser by a TTL signal, so the microchannel plate of the camera intensifier and the photocathode opened only for the full laser pulse width; minimising the noise and capturing the scattered light. Further details of the camera settings and noise contributions to the Thomson spectrum can be

found in section 4.2.3.

Stray light and noise contributions is the biggest persisting problem in the Thomson scattering system and efforts had to be made to reduce these effects. Stray light originates from dispersion of optical components and reflects inside the vacuum chamber, able to reach the detection system. Noise in the measured Thomson signal is created at the iCCD interfaces. The ways in which stray light and noise has been reduced and accounted for are shown in the following sections.

4.2.1 The Issues of Stray Laser Light

A limiting factor in any CCD is saturation; the maximum charge a pixel can store between readouts. To avoid damage to the camera, the signal intensity must be kept below this threshold. However for weak signals such as a Thomson spectrum, iCCD's are used with maximum intensifier gain and a relatively long integration time. The signal with the largest amplitude, and therefore risk of saturation, is the superposition of stray light and Rayleigh signals. These signals have an almost monochromatic spectrum on the CCD, and are therefore predominantly present at the centre of the Thomson spectrum (due to redistribution of light by the instrumental profile this causes a slight broadening). An obvious method to stop camera saturation would be to perform multiple consecutive measurements with small integration times and sum the resultant spectrum. This however yields a lower signal to noise ratio due to noise being added to the spectrum every time the CCD is readout. This is known as readout noise, and in this system yields poor results with large errors. To protect the camera, attenuation of a small region around the laser wavelength is required to block the stray light and Rayleigh signals and protect the camera from laser misalignment. Details in section 4.2.2.

The instrument function of a spectrometer can redistribute light and for a monochromatic light source, produce a peak with a finite spectral width. In this research, the instrument function was modelled as the Rayleigh scattering spectrum (S_{RS}) which is justified by considering each of the individual components that contribute to spectrum broadening. These are: Doppler broadening (S_{DB}), laser line width (S_{LW}) and the Instrument function (S_{IF}). The latter term has encompassed the contributions from the entrance slit width of the spectrometer, signal diffusion in the ICCD and non-ideal optical elements causing aberrations. If S_{DB} and $S_{LW} \ll S_{IF}$ such that $S_{RS} \approx S_{IF}$ then the instrument function can be modelled as the Rayleigh spectrum. Allocating Gaussian profiles for each

contribution, then S_{RS} is the convolution of the above terms:

$$S_{RS} = A \cdot S_{DB} \otimes S_{LW} \otimes S_{IF} \tag{4.1}$$

Where A is an amplitude scaling factor. The full width half maximum (FWHM) for S_{RS} from the detector system used in this work is measured to be $\approx$ 218 pm, for S_{DB}, it is calculated to be $\approx$ 1 pm and for S_{LW} it is stated by the laser manufacturer to be $\approx$ 40 pm. Through the convolution theorem, S_{IF} FWHM is calculated to be $\approx$ 214 pm. Hence S_{RS} (FWHM = 218 pm) $\approx$ S_{IF} (FWHM = 214 pm) and the criterion is met.

Figure 4.4, shows a measured Rayleigh scattering spectrum from an experiment performed in this work, which as stated above, can be modelled as the effective instrument function of the system. This particular figure was created using maximum gain on the iCCD camera and was accumulated over 10 s (100 laser pulses) using argon gas of pressure 470 Pa. It is normalised over the wavelength axis of the spectrometer, such that integral of intensity over each wavelength is equal to 1. Stray light becomes an issue when it's redistribution interferes and overlaps with the wings of the TS system. A triple-grating spectrometer is used to mitigate this effect and it's operating principle is described on the next page.

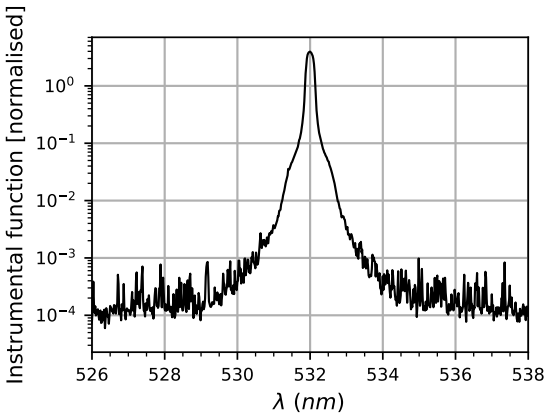

Figure 4.4: The normalised instrumental function of the triple-grating spectrometer detection system used in this work. Created using Rayleigh scattering from argon gas of pressure 470 Pa. The entrance slit was set to a width of 0.30 mm, the second slit, located at the notch location had a width of 20 mm and the exit slit had a width of 0.42 mm.

4.2.2 The Triple-Grating Spectrometer (TGS)

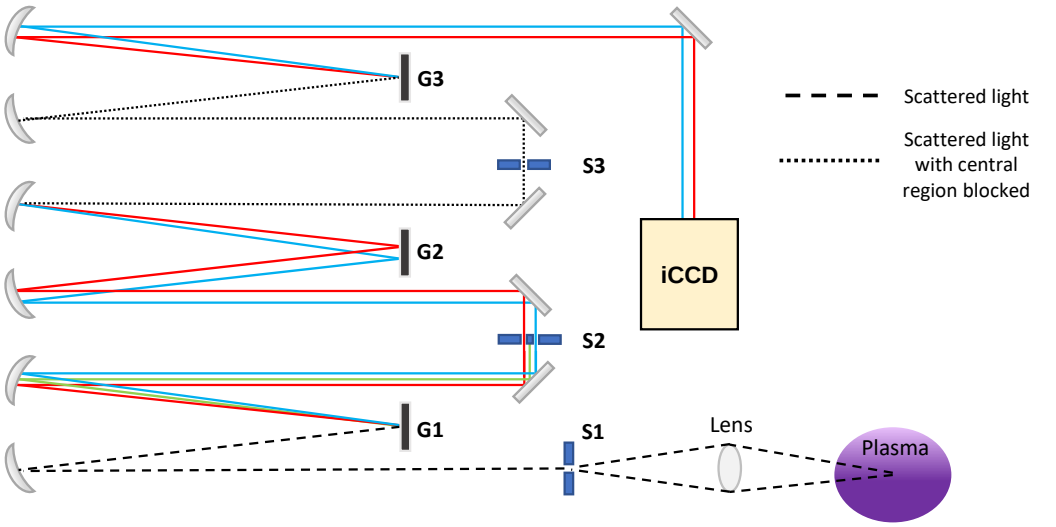

Figure 4.5: A schematic of the scattered light path as it passes through each stage of the triple grating spectrometer. Labelled is the slits (S1-S3) and the gratings (G1-G3).

The optical arrangement of the triple grating spectrometer, is a robust and well renowned design and its principles is shown in figure 4.5. In this set up, light entering the spectrometer first passes through the slit S1 with width 0.3 mm, and the collimated beam is then directed to the first grating, G1. The light is then dispersed and passes through S2 of width 20 mm (large to account for the dispersion) and a central mask is placed to block the wavelength region 531.5 - 532.5 nm corresponding to the stray light and Rayleigh signal region. If the iCCD camera was to be placed after S2 then the wings of the stray light spectrum would dominate over the Thomson scattering spectrum. This is due to the redistribution of the stray light from the first spectrometer and hence the ability of a 532 nm photon being able to avoid the mask, passing through S2. Therefore, efforts need to be made to reduce this stray light domination.

The way the TGS counters this light dispersion, is to mirror the arrangement of the first spectrometer, this is known as the double subtractive configuration. The light now missing the central region is recombined at the second grating, G2, and exits the second spectrometer at S3 of width 0.42 mm. S3 has larger width than S1 to account for any misalignment but is still kept small so the probability of a 532 nm photon redistributed by

the second spectrometer does not pass through it. The small slit also reduces the amount of background light entering from the previous spectrometers. This background light is produced throughout the TGS from scattering contributions from optical components and the different diffraction orders. The final step is to disperse the light onto the iCCD by using a third grating, G3. A 532 nm photon that has entered and hit the third spectrometer, can only interfere with the Thomson signal if it is redistributed outside of the mask region.

Consequently, a TGS system has excellent stray light mitigation and attenuation as the probability that a 532 nm photon is able to pass through the slits, avoid the mask and be registered outside of the mask region, interfering with the Thomson signal is extremely small. However, as is evident from figure 4.5, many optical components are needed which not only degrades the optical transmission, the equipment is also expensive. Furthermore, the complexity of the design means the system is very sensitive to misalignment.

It was found that fluctuations in ambient temperature affected the alignment of the TGS. A combination of laser operation and optical component drift meant that frequent realignment of the TGS was needed. To mitigate the effect that high laboratory temperature had on the laser operation, the laser was allowed several hours to equilibrate at its optimum operating temperature and was fired for 15 minutes prior to TS measurements to allow the beam to settle. Its cooling system was also cleaned periodically. Frequent small adjustments of the TGS were needed to ensure the optics were aligned correctly and the notch filter blocked the central region. This was a combination of manual adjustments and resetting of the TGS to ensure the laser wavelength was central on the CCD. Alignment was checked before and after every measurement by plotting the Rayleigh spectrum with and without the notch filter present. This combined with instrument function plotting (as shown in figure 4.4) meant that any drift in alignment was tracked and could be rectified. This meant that the instrument function remained symmetric, the laser wavelength was central to the CCD and the notch filter blocked the desired wavelength region.

4.2.3 Sources of Noise and SNR

This section considers the path of the scattered photons throughout the detection system and the contributions of noise through each stage of detection. It can be shown that there are three main contributing sources in a TS measurement; Thomson scattering and plasma emission statistical noise, intensifier noise and CCD noise. The following discussion highlights the efforts made to reduce noise and increase the signal to noise ratio (SNR), and

presents the detection system parameters. The path of the photons through the detection system is shown in figure 4.6 and the factors T, Q_1, g, Q_2 and S will be described below. Table 4.1, summarises the detection system parameters, for the readers convenience.

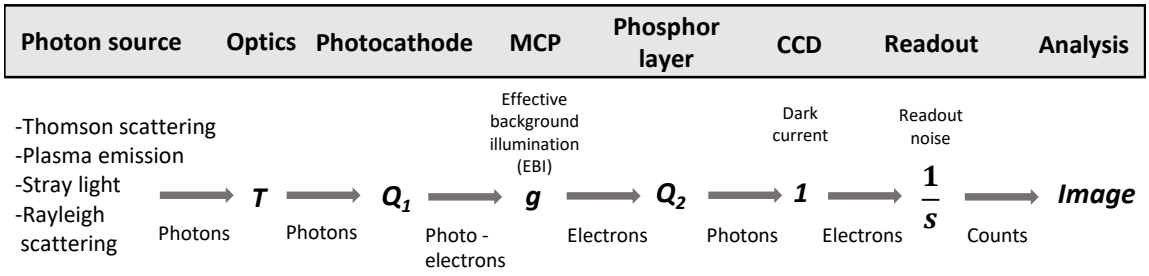

Figure 4.6: Photon path through the detection system.

Paramater	Symbol	Value	Units
Laser beam width	b_w	~ 0.25	mm
TGS slit 1 (S1) width	w	0.3	mm
TGS slit 1 (S1) length	l_s	6	mm
Magnification factor	m	-1.82	-
Detection volume length	$L(l_s/m)$	3.3	mm
Detection volume width	w/m	0.17	mm
Collection solid angle	$\Delta\Omega$	0.046	sr
Laser beam pulse length	t_l	5	ns
Photocathode gate width	Δt_{Pc}	7.5	ns
Optics transmission	T	~ 0.05	-
Photocathode QE	Q_1	0.41	-
Phosphor and CCD combined QE	Q_2	≥ 0.9	-
Photoelectron effective gain	gQ_2	1299	CCD e^-/Photocathode e^-
Min photoelectron effective gain	g_0q_2	1.65	CCD e^-/Photocathode e^-
MCP gate width	Δt_{MCP}	107.5	ns
MCP noise factor	F	~ 1.6	-
Readout sensitivity	S	3.4	CCD e^-/Count

Table 4.1: Summary table of the photon detection system parameters.

Considering the path of the scattered incoming photons through the detection system, shown in figure 4.6, the photons first pass through optical components of transmission $T \sim$

0.05 and strike a photocathode of efficiency Q1 = 0.41. Due to the low Thomson scattering cross section, the number of Thomson scattering photons striking the photocathode is very small (of the order $\sim 10^{-17} \cdot n_e$ $[m^{-3}]$ [157]). Consequently, due to the probabilistic nature of the quantised scattering event, there is a relatively large statistical fluctuation in the number of photoelectrons generated, for each laser pulse. This randomness can be modelled by the Poisson distribution and is referred to as shot noise. The SNR at this point can be shown to be:

$$\mathrm{SNR}_{photocathode} = \frac{N_p T Q_1 \hat{N}_{Ti}}{\sqrt{N_p T Q_1 \hat{N}_{Ti}}} = \frac{\delta_{TS^2}}{\delta_{TS}} \tag{4.2}$$

Where, δ^2_{TS} is used to represent the mean number of photoelectrons and δ_{TS} represents the standard deviation. $\hat{N}_{Ti}$ represents the number of photons collected per pulse for the ideal system ($\hat{N}_{Ti} = N_{TS_{ideal}}/N_p$) where $N_{TS_{ideal}}$ is given by equation 3.12.

After the photo electrons have been created at the photocathode, they are accelerated by an electric field to the michrochannel plate (MCP). The MCP amplifies the electron current (and shot noise) by gain g, this amplification process is described by a distribution function such that an additional source of noise is also introduced. The resultant SNR at this point is the entering shot noise multiplied by Fg where F is provided by the manufacturer as $F \sim 1.6$

$$\mathrm{SNR}_{MCP_{TS}} = \frac{g\delta^2_{TS}}{Fg\delta_{TS}}. \tag{4.3}$$

It is noteworthy that the amplified shot noise is also present upon the plasma emission signal. Equations 4.2 and 4.3 provide an analogous result for the plasma emission, where the SNR can be shown to be:

$$\mathrm{SNR}_{MCP_{PE}} = \frac{g\delta^2_{TS}}{Fg\delta_{PE}}. \tag{4.4}$$

Where now, δ_{PE} represents $\sqrt{N_p T Q_1 \hat{N}_E}$ and N_E is the number of plasma emission photons collected per pulse for the ideal system. The noise contribution from the plasma emission is minimised by gating the phtocathode with respect to the laser pulse width such that excess plasma emission photons are not collected. The photocathode gate width Δ_{Pc} was 7.5 ns and the laser pulse width t_l was 5 ns (see table 4.1). Furthermore, a linear

polariser at the entrance to the triple-grating spectrometer attenuates the unpolarised plasma emission signal whilst transmitting the linearly polarised Thomson signal, again reducing the plasma emission contribution.

Now the electrons created are converted to photons of single wavelength using a phosphor layer and are guided towards the CCD chip to create electron-hole pairs. This has a quantum efficiency of $Q_2 \gtrsim 0.9$ and the wavelength of the photons is chosen to maximise this (i.e close to unity efficiency). This is again shot noise and the contribution to the SNR is found to be:

$$\mathrm{SNR}_{phosphor} = \sqrt{\frac{gQ_2}{1-Q_2}} \cdot \frac{\delta_{TS}^2}{\delta_{TS}} \tag{4.5}$$

A quick comparison of equation 4.5 and 4.3 shows that the noise contribution in the phosphor layer is negligible as the high gain of the MCP ($gQ_2 = 1299$) ensures a large number of electrons in the CCD per photelectron generated. I.e $F \gg \sqrt{\frac{1-Q_2}{gQ_2}}$. Such that this term can be neglected in the analysis.

Thermally generated photoelectrons created at the photocathode, contribute the dominant noise from the intensifier as this signal is amplified by the MCP. This is known as the effective background illumination (EBI). To minimise this, a synchronised but short (107.5 ns) gating of the MCP voltage is used, such that this dark current is amplified for short periods only. The resultant noise has the same form as equation 4.3 :

$$\mathrm{SNR}_{MCP_{EBI}} = \frac{g\delta_{TS}^2}{Fg_0\delta_{EBI}} \tag{4.6}$$

Where now, δ_{EBI} is equal to $(N_{EBI}N_p/f_{(Hz)})^{1/2}$. With N_{EBI} equal to the number of photoelectrons per second and the term $N_p/f_{(Hz)}$ represents the Thomson scattering integration time. As with the Thomson signals and plasma emission signals, the electrons created are converted to photons, but the effective gain of the MCP ($g_0Q_2 = 1.65$) is much less, making it's overall contribution virtually negligible. A final noise consideration comes from the CCD, where dark current and readout noise contribute. The readout noise comes from the conversion of charge to counts, this has a sensitivity of S = 3.4 electrons per count. These however can be negated and become insignificant if a high intensifier gain is used, and the CCD is kept at low temperature. In this research, the CCD was kept at 243 K and maximum gain was used for all Thomson and Rayleigh measurements.

In summary, sources of noise in the Thomson scattering experiment arise from: the sta-

tistical noise of the Thomson and plasma photons, intensifier noise and CCD noise. Using a high gain for the intensifier, keeping the camera cool, gating the MCP and photcathode with short periods in synchronisation with the laser pulse and reading out the CCD once per spectrum minimises the latter two such that they become insignificant. Thus the SNR can be calculated from the resultant combination of the contributions of plasma and Thomson scattering shot noise. This is done by adding the relative standard deviations in quadrature, to give:

$$SNR_{total} \approx \left(\frac{1}{SNR^2_{MCP_{TS}}} + \frac{2}{SNR^2_{MCP_{PE}}} \right)^{-\frac{1}{2}} = \frac{\hat{N}_{Ti}}{F} \cdot \sqrt{\frac{N_p T Q_1}{\hat{N}_{Ti} + 2\hat{N}_E}} \tag{4.7}$$

.

Here the factor 2 encompasses the plasma emission contributing both to the background measurement and the Thomson measurement (i.e with laser off and on). For a typical plasma condition, laser power and acquisition time used in this research; $n_e = 10^{18}$, $N_p = 600$ (acquisition time of 60 s) and laser power of 2.4 W. The SNR can be shown to be > 36 if the plasma emission is half as intense as the Thomson signal ($\hat{N}_E < \hat{N}_{Ti}/2$). This however quickly degrades for higher plasma emission such that the system has to be designed to minimise this.

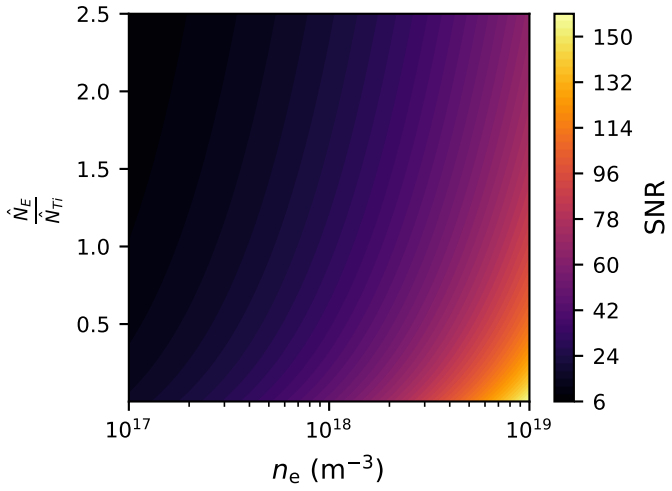

Figure 4.7: SNR dependence on plasma density and plasma emission intensity. Here, N_p and laser power were kept constant at 600 and 2.4 W respectively.

Figure 4.7, shows the resultant SNR, for combinations of n_e and plasma emission ratios, $\frac{\hat{N}_E}{N_{Ti}}$, shown as a contour plot. The density ranges in this plot are $10^{17} - 10^{19}$ m^{-3}, which cover the predominate measured n_e values reported in this work. It is clear that the SNR vastly improves with increasing n_e, and reduces for increasing plasma emission fraction. For lower n_e values and high plasma emission, the SNR is the lowest, resulting in noisy data. Fortunately, in the case of this work, low n_e values are typically measured during the plasma afterglow, where there is little plasma emission, thus maintaining a high SNR for measurement. Furthermore, careful consideration of the target material must be made such that intense emission lines of the material do not lie within the CCD spectral range. For the tungsten target used in this work, this is fulfilled.

As stated earlier in section 2.3.3, photon counting can further improve the SNR ratio and would result in F in equation 4.7 equalling 1, resulting in a total SNR increase of 1.6. This technique was not used in this work in an effort to minimise the acquisition time and thereby reducing transmission losses from sputtering on the chamber window. Photon counting requires multiple readouts of the CCD per measurement, as the CCD pixel can only record one photon at a time, which would increase the measurement time significantly. This would result in large transmission losses throughout the measurement, which in turn would cause the density calibration to over-estimate n_e and require frequent changing of the soda glass. In this work, the TS and background signal on the CCD was integrated over the acquisition time and readout once per measurement.

4.2.3.1 Spectral SNR

In the previous treatment, equation 4.7 is formulated from the summation of the number of collected photons at each wavelength of detection in the TS spectrum. However, for incoherent Thomson scattering, the spectrum is proportional to the EVDF in the direction determined by the scattering geometry. In this work, the measured EVDF's were found to be Maxwellian and thus have a Gaussian distribution, with the scattering signal intensity degrading at increasing wavelength shift from the scattering beam ($\Delta\lambda = \lambda - \lambda_i$). This results in an SNR distribution, whereby the SNR decreases at increasing wavelength shift. From equation 3.17 the one-dimensional probability velocity distribution (and equivalently the energy distribution) function is $\propto e^{(\Delta\lambda^2)}$ and hence a plot of $\log_e$(intensity) vs $\Delta\lambda^2$ would result in a linear straight line plot for the ideal Maxwellian distribution. This is shown in figure 4.8.

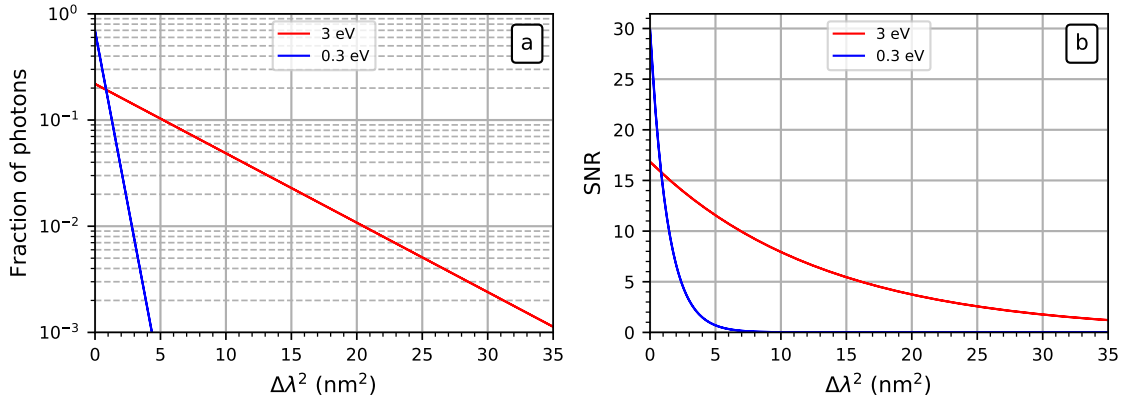

Figure 4.8: (a) The fraction of scattering photons for a Maxwellian EVDF as a function of $\Delta\lambda^2$ for two typical electron temperatures measured in this work of 0.3 and 3 eV. (b) the resultant SNR TS shot noise dependence with $\mathrm{SNR}_{total} = 36$.

Figure 4.8 (a) shows the fraction of TS photons for Maxwellian EVDF's of temperatures 0.3 and 3 eV. Figure 4.8 (b) shows the resultant spread in the SNR as a function of $\Delta\lambda^2$ and total SNR taken as the above value of 36. Clear from these figures is that, for lower measured T_e, the SNR quickly decreases at increasing wavelengths, with high SNR's close to the scattering wavelength. For the higher T_e, the SNR has a lower peak near the scattering wavelength and maintains a relatively high value over the wavelength range shown here. To experimentally resolve the wings of low T_e requires an increase in scattering intensity, which can be achieved with longer acquisition times by collecting data over a larger number of laser pulses.

Examples of TS spectra found in this work, for comparable temperatures to that shown in figure 4.8, are presented in figure 4.9, for (a,b) $T_e = 0.32$ eV and (c,d) $T_e = 2.97$ eV . Figures 4.9 (a,c) show the resultant fraction of signal intensity as a function of $\Delta\lambda^2$ and figures 4.9 (b,d) show the measured spectrum. Plotted also is the Gaussian fit used to extract electron temperature. The figures are normalised similar to figure 4.8 whereby, the fraction of the signal intensity is plotted relative to the resultant Gaussian fit. They show that the measured TS spectrum's are Maxwellian due to the linear relationship of the fraction of intenisty vs $\Delta\lambda^2$. These figures also highlight the SNR relationship found in figure 4.8, as for subsequent $\Delta\lambda^2$ shifts, the data becomes increasingly noisy. This is most evident for the $T_e = 0.32$ eV plot. It should be reiterated that the notch region (531.5 nm - 532.5 nm) was excluded from the fit. Plots of intensity vs $\Delta\lambda^2$ were routinely created

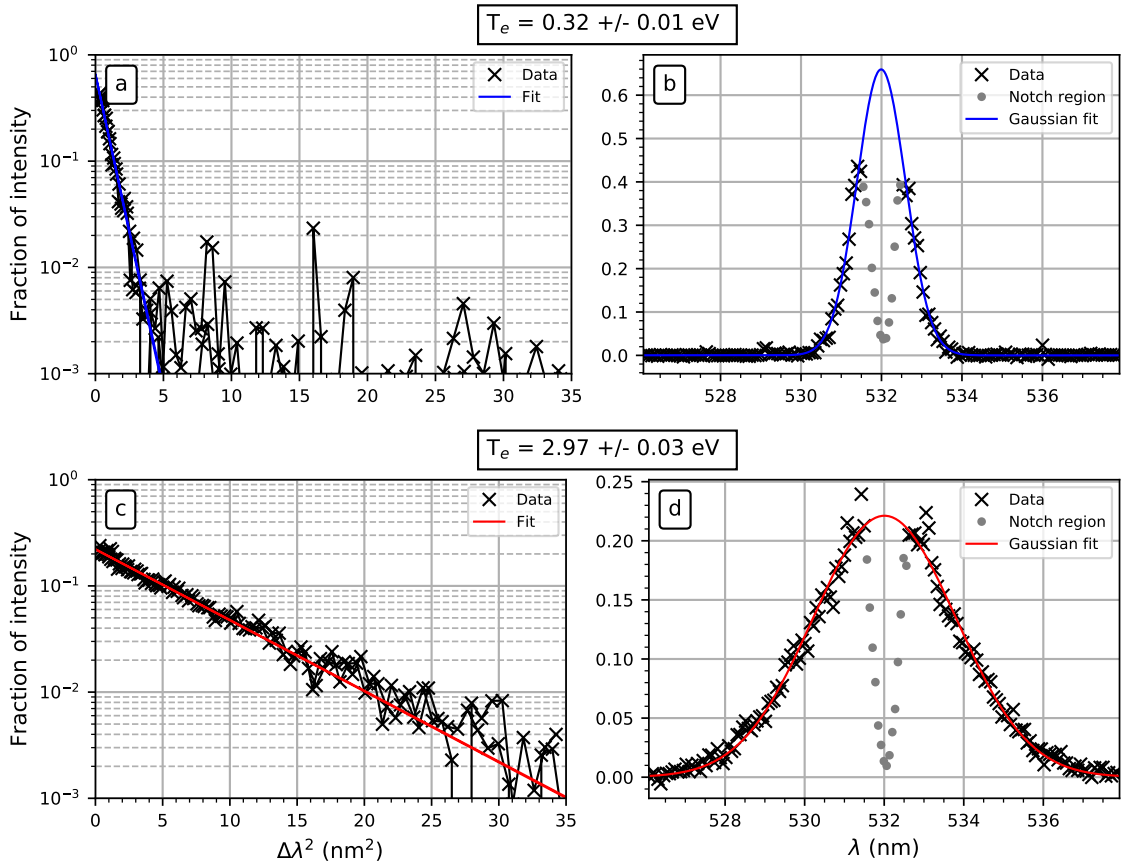

Figure 4.9: (a,c) The fraction of scattering intensity as a function of $\Delta\lambda^2$ for electron temperatures of 0.32 eV and 2.97 eV from example TS spectra measured in this work. (b,d) The TS spectra used to create (a,c). Plotted also is the Gaussian fit to the data.

after every TS measurement to check the validity of the Maxwellian assumption. All of the TS spectra in this work were deemed to be Maxwellian.

4.2.4 Measurement Positions

In this work, two different laser beam alignments were performed with the laser beam propagation in the target surface plane. This allowed centre-line and racetrack measurements to be made. Figure 4.10 (a), shows the beam path relative to the target surface. Figure 4.10 (b) shows the measurement positions in the r - z plane with respect to the

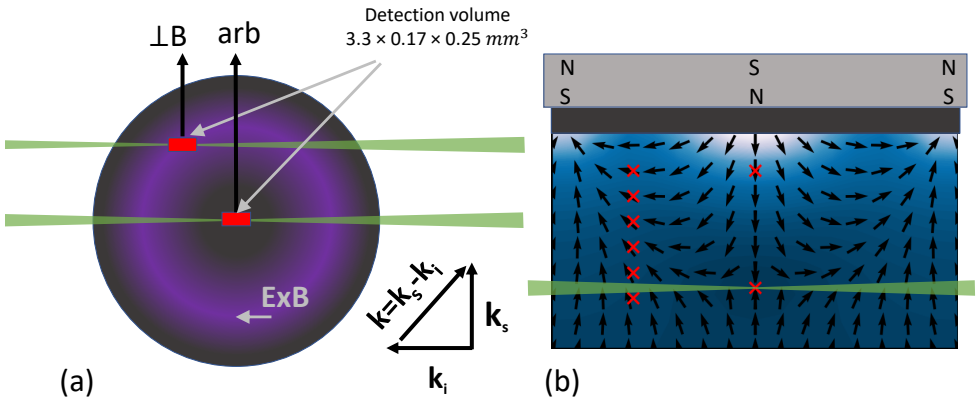

Figure 4.10: (a) The beam propagation through the chamber with respect to the target diameter. The two detection volumes are labelled, with scattering, $\mathbf{k_s}$, incident, $\mathbf{k_i}$ beam and the resultant $\mathbf{k}$ vector directions shown. (b) Measurement locations in the r - z plane. Note that the magnetron was mounted vertically with the target face pointing downward.

magnetic field configuration (also shown in 4.2). For centre-line measurement positions, the laser beam was aligned through the centre of the chamber. For racetrack measurements, the beam was offset 34 mm from the centre. The collection lens and consequently the TGS were placed at $\pi/2$ rad with respect to this laser propagation, placed centrally for centre-line measurements and offset by 34 mm for racetrack measurements. This allowed racetrack measurements to be made at r = 48 mm, despite the small size of the viewing port[1]. For racetrack TS measurements, the laser beam had an azimuthal angle of $3\pi/4$ radians, measured anticlockwise with respect to the laser beam propagation through the chamber. Consequently, the scattering vector was aligned perpendicular to the magnetron magnetic B-field. For centre-line measurements, the scattering vector was in an arbitrary plane. To measure the positions in the Z direction, the magnetron was moved vertically, with the laser beam propagation fixed through the chamber.

Careful consideration of the detection lens position and distance from the detection volume (s) and in turn, the distance of the TGS entrance slit from this optic (s') is

[1]The viewing port restricted full view of the magnetron and consequently meant that the laser beam propagation could not be simply offset to measure large radial distances easily.

needed. The placement of the lens affects the solid angle ($\Delta\Omega$) of collection, detection and the magnification (m) of the image. The solid angle is calculated to be $\Delta\Omega \approx \pi d^2/4s^2$, where, d is the diameter of the collection lens (75 mm), the relationship between s, $s^{'}$ and m is given by the well known equations:

$$\frac{1}{f} = \frac{1}{s} + \frac{1}{s'} \tag{4.8}$$

$$m = -\frac{s^{'}}{s} = -\frac{f}{s-f} \tag{4.9}$$

Returning to the ideal number of photons collected stated by equation 3.12 a number of substitutions can now be made in an effort to relate the number of collected photons and the position of the lens. Firstly, L is equal to the length of the entrance slit (l_{es} = 6mm) magnified by m; $L = l_{es}/m$. Secondly, the number of photons in the detection volume can be shown to equal the total number of laser photons per pulse, $N_l^{'}$ multiplied by the width of the TGS entrance slit width, w_e = 0.3 mm (with magnification considerations) divided by the laser beam width, b_w = 0.25 mm. Therefore, $N_l = N_l^{'} w/b_w m$.Finally, $\Delta\Omega$ can be substituted to give an overall proportionality of:

$$N_{TS_{ideal}} \propto N_L L \Delta\Omega \propto \frac{(s-f)^2}{s^2} \tag{4.10}$$

Hence it is essential to maximise this function to ensure a large signal of incoming photons. However, limitations such as the maximum acceptance angle of 0.014 sr of the TGS entrance slit and the equipment limitations, meaning that the lens cannot be placed closer than 250 mm to the detection volume, limit the placement of the lens. It was found by a previous PhD student [188, p. 94] (Peter Ryan) that the lens is best positioned at $s^{'}$= 564 mm away from the entrance slit and consequently placed s = 310 mm from the detection volume. This in turn, created an inverted image of magnification m = -1.82 and a detection volume of $\frac{l_{es}}{m} \times \frac{w}{m} \times b_w = 3.3 \times 0.17 \times 0.25$ mm^3 imaged on the iCCD.

In total, 8 Thomson scattering measurement positions were performed in this work: 6 measurement positions above the racetrack, starting at 15 mm and ending at 65 mm in steps of 10 mm and two centre-line measurements at z = 15 and z = 61 mm. These are shown in figure 4.2 and again in 4.10. Measurements closer to the target were limited by the anode ring, which protruded $\sim$ 7 mm from the target surface.

4.2.5 Data Capture and Analysis

The first step of any measurement was to create a stable plasma and determine the position (relative time) on the HiPIMS waveform a Thomson signal is to be taken. Time-resolved measurements were achieved by synchronising the laser, iCCD and plasma source. This was accomplished using a transistor-transistor logic (TTL) signal from the HiPIMS source to trigger the firing of the laser which in turn triggered the iCCD. The laser pulse was delayed in time, relative to the HiPIMS discharge waveform, through the use of an Arduino Due board. The 50 Hz TTL signal was divided by 5 to produce the 10 Hz signal required for laser pulsing. This system had a time resolution of $\sim$5 μs. The laser itself needed 1-2 hours to thermally stabilise and a further 15 minutes of firing time for the power to maximise and become stable. After these conditions have been met and the laser is firing synchronous to the waveform, measurements with the laser on and off needed to be taken. This enabled the plasma emission to be subtracted and isolation of the Thomson scattering spectrum to be isolated. For measurements performed in this work, data accumulation was recorded for 60 - 3000 laser pulses (60 – 300 s), for both Thomson and background images, with the average laser power over this time period recorded.

After the Thomson signal had been isolated, The resultant spectrum was then summed over the spatial dimension (3.3 mm) and the pixel axis was then separated into bins of 4 pixels to reduce noise. To convert between the CCD pixel array and the corresponding wavelength, the dispersion relationship (nm/mm) from the TGS manual was used. The resultant resolution was $\sim$ 0.071 nm. It is important to reiterate here that for the Thomson measurements and the background plasma emission measurements, the mask was inserted to attenuate the wavelength region around the laser wavelength as stated in section 4.2.2. A check was performed periodically to monitor the stray light and Rayleigh signals contribution to the Thomson signal by performing a measurement with the laser on, mask inserted and no plasma present. This yielded no signal meaning these contributions were negligible.

To extract an electron temperature, a Gaussian of the form of equation 3.21 was fitted to the data points outside the notch region. This models the data inside the notch region and allows electron properties of the bulk population to be made. The lowest temperature the system can detect is determined by the width of the TGS notch filter. This is roughly 0.5 nm and following equation 3.22 gives a minimum temperature of $T_e = 0.12$ eV. The analysis was done via a python script that used the “curve fit’ fitting function that minimises the

sum of the residual squares.

A final consideration taken into account when analysing the resultant TS spectra, was the temperature overestimation due to the instrument function contribution to the signal. The resultant spectrum will be a convolution of the instrument function of the TGS and the Doppler broadening due to the electron motion and consequently, will depict a higher temperature. Thus, deconvolution needed to be considered. It was shown in section 4.2.1 that a good estimation of the instrument function is the Rayleigh spectrum. Modelling the instrument function as a Gaussian curve, the decovolution of the instrument function and the Gaussian Thomson spectrum is trivial, with the percentage error given by [190]:

$$\%_{err} = \frac{[\sigma_1^2(T_e) + \sigma_2^2] - \sigma_1^2(T_e)}{\sigma_1^2(T_e)} \times 100 \tag{4.11}$$

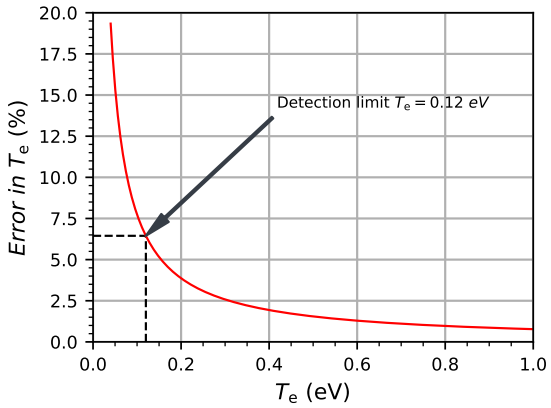

Figure 4.11: A graph showing the percentage error in the measured T_e values due to the convolution of the instrument function and Thomson scattering signal. Both of which are modelled as Gaussian curves. Indicated on the graph is the detection limit of the system of 0.12 eV

Where $\sigma_1(T_e)$ is the standard deviation of the resultant Gaussian curve of temperature T_e. σ_2 is the standard deviation of the instrument (Rayleigh) function found from the FWHM $= 2\sqrt{2ln(2)} \cdot \sigma_2 = 218$ pm. Figure 4.11 shows the error as a function of temperature. The detection limit of the system was ~ 0.12 eV which corresponds to an error overestimation of 6.5 % and the error quickly becomes insignificant at higher temperatures. For completeness, each TS spectra was de-convolved, separating the instrument function and the true TS signal. To do this, the Rayleigh scattering signal at the highest pressure

was used as the instrument function (justified in section 4.2.1). The convolve function in Python was used for this procedure, where the Gaussian fit to the data was convolved with the instrument function. This function then returned the best fit parameters of the Gaussian curve to the data and thus the true electron temperature can be determined.

Density calibration was performed by means of Rayleigh scattering (see section 3.3.2). This was done by performing a background measurement (with no plasma present), with the laser firing into the chamber with measurement base pressure and measurements with several gas pressures. The notch filter was removed for these measurements and each measurement ran for 1 s (10 laser pulses) The range of pressures was 50 - 1000 Pa which ensured the Rayleigh dominated the stray light signal. The gate valve to the turbomolecular pump was shut when adding gas and was extracted by using a secondary rotary pump until the valve could be reopened once again. The CCD images were treated similar to the Thomson scattering images, but are now numerically integrated to calculate the scattering intensities for the given pressure.

Following section 3.3.2 electron density can now be calculated. The density calibration was done immediately after every Thomson scattering measurement, due to the constant transmission loss due to the sputtered flux of material on the viewing port of the chamber. The change in transmission was kept to a minimum by keeping the data acquisition time small and consequently the density overestimation was kept to a minimum. Experiments were performed comparing Rayleigh scattering calibration data, before and after a TS measurement. For the longest TS acquisition time used in this work, this resulted in a discrepancy of $< 12\%$. This provided the largest error in n_e determination.

4.2.6 Laser Perturbation Considerations

LTS is thought of as a non-invasive diagnostic technique. In this section, considerations of laser perturbation to the plasma source are explored, justifying the technique as non-invasive. This is true if, negligible temperature or density perturbations occur in the plasma due to the scattering source and is discussed in this section.

4.2.6.1 Electron Heating

A relatively high powered laser source is required for LTS measurements to ensure enough scattering signal is obtained, however, the laser power must not be too high as to perturb the plasma. The electric field of the laser source can heat free electrons inside the plasma.

Inverse Bremsstrahlung is the most likely candidate for radiation absorption [191], whereby an electron, near an ion [2], absorbs a laser photon. Kunze [192] calculated the fractional increase in electron heating and is given by:

$$\frac{\Delta T_e}{T_e} = 5.32 \times 10^{-11} \cdot \frac{n_e Z^2 \lambda_i^3 I}{T_e^{\frac{3}{2}}} \left(1 - exp\left(\frac{-hc}{\lambda_i T_e e}\right)\right), \tag{4.12}$$

where n_e is the electron density, Z is the charge of the ions, T_e is electron temperature (in eV), λ_i is the laser wavelength and I is the laser intensity (in units Jm^{-2}). This formula gives the upper limit, whereby the electrons in the plasma are assumed to thermalise during the laser pulse, but no transfer to ions occurs. Equation 4.12 is valid when the absorption coefficient of the plasma is not strongly changed by the laser beam. This is the case if the photon energy of the scattering beam is much larger than the maximum kinetic energy gained by an electron in the electric field of the laser. This relation is given by:

$$\frac{hc}{\lambda i} \gg \frac{e^2 E_0^2}{2 m_e \omega_i^2}, \tag{4.13}$$

where, $\omega_i = \frac{2\pi c}{\lambda_i}$, m_e is the electron mass and E_0 can be calculated from the timed averaged value of the Poynting vector $\langle S \rangle$ through the equation:

$$\langle S \rangle = \frac{1}{2} \epsilon_0 c E_0^2 \Rightarrow E_0 = \sqrt{\frac{2\langle S \rangle}{\epsilon_0 c}}, \tag{4.14}$$

where $\langle S \rangle$ is equal to the time averaged power over the beam area $= \frac{\langle P \rangle}{A}$. In this work, the laser source provided 200 - 250 mJ of energy per pulse, into a focused scattering volume of diameter ~ 0.25 mm, over a ~ 5 ns pulse length. This yields an intensity ($\langle S \rangle$) in the range 10^{14} - 10^{15} Wm^{-2} and corresponding electric field amplitudes, E_0, of 300 - 900 MVm^{-1}. Substituting values into equation 4.13 gives the maximum kinetic energy to be 0.6 - 6 meV and the photon energy of the 532 nm scattering beam to be 2.33 eV. Hence equation 4.12 is justified and yields the highest fractional heating for high n_e, highest laser intensity I, and low T_e. In this work, the highest n_e measured with the corresponding lowest T_e is $\sim 10^{19}$ m^{-3} and 0.3 eV respectively. Substituting these values alongside with the highest laser intensity into equation 4.12 gives the worst case scenario, fractional heating of $\frac{\Delta T_e}{T_e}$ = 0.002. Hence, laser heating can be neglected in this work.

[2] The presence of an ion conserves the momentum in this process.

4.2.6.2 Pondermotive Acceleration

Along side electron heating, the incoming laser beam can cause density perturbations. Schneider [193] and Powis et al [194], considered the effect of the pondermotive force on electrons on low density, low temperature plasmas through a combination of calculations and simulations. The pondermotive force accelerates electrons through intensity gradients of the laser beam, from higher to lower electric field intensities throughout the wave period. This effect may perturb local plasma density and cause a decrease in the number of electrons in the scattering volume that contribute to the TS signal, resulting in inaccurate density measurements. The relative perturbation in local electron density from a Gaussian laser beam was found to be:

$$\frac{\Delta n_e}{n_e} \approx \frac{e^2 \lambda_i^2 I}{\epsilon_0 4\pi^2 c^3 \overline{e} T_e e m_e \left(1 + \frac{b_w^2}{2\lambda_D^2}\right)}, \tag{4.15}$$

where b_w is the focused laser beam width, $\overline{e}$ is Euler's number, λ_D is the Debye length and the other symbols have the same allocation as in equation 4.12. Equation 4.15 has it's maximum when n_e and T_e are low and I is high. The lowest n_e corresponding to the lowest T_e measured in this work is $\sim 10^{17}$ m^{-3} and 0.2 eV respectively. Substituting these values alongside with the highest laser intensity into equation 4.12 gives the worst case scenario, fractional density perturbation, $\frac{\Delta n_e}{n_e} = 0.003\%$. Hence, pondermotive effects can be neglected in this work and minimal density perturbations are expected to occur in the TS system.

It should be noted that using higher laser intensities (i.e higher powered lasers) results in a higher density perturbation, and as such, simply increasing the laser power in an attempt to gather a larger TS signal is not beneficial. Using lasers with large wavelengths also increases the perturbations. There exists a compromise between the laser intensity needed to gather enough scattering signal, but not to perturb the plasma. However the design choices in this work and the range of measured electron properties, allowed density perturbations to be insignificant. The largest error in density arose from transmission losses due to sputtered target material reducing transmission through the viewing port. This was discussed in section 4.2.5.

4.2.6.3 Photoionisation

Finally, effects of ionisation from the laser beam are considered. If the laser beam can provide enough energy to the neutrals and ions in the plasma, they can be ionised (or further ionised). Thus n_e increases, resulting in inaccurate density measurements. Photionisation can occur through direct (one photon) and multi photon excitation. The energy of a 532 nm photon is 2.33 eV, the first ionisation energies of argon and tungsten are 15.76 eV and 7.98 eV respectively. Therefore, direct ionisation of ground state atoms from a single photon is not possible. Direct ionisation can occur for excited species when the excited state energy (E_{ex}) is larger than the difference between the ionisation energy (E_i) and the photon energy (E_p): $E_{ex} \geq E_i$ - E_p. Such excited atomic states are expected to be negligible in this work. Multi photon excitation is much less likely due to the much lower cross section, however it's probability scales with laser intensity [195]. Photoionisation effects were expected to be insignificant in this work, however to confirm this, experiments were performed altering the laser power for different plasma conditions. The down side of this is, that for lower laser power, more data averaging is needed to acquire an adequate scattering signal and therefore, density overestimation has a greater effect on lower laser powered TS measurements. That said, it was found that the measured electron density was within $< 10\%$ of one another for different laser powers. This gives confidence that photoionisation effects could be neglected in this work.

4.2.7 Alterations and Considerations for Optical Emission Spectroscopy Measurements

Optical emission line data from the discharges was also obtained using the TGS, however in this case with a small aperture of diameter 3 mm placed behind the collection lens and the entrance slit changed to 0.1 mm to improve the spectral resolution. The spectrometers in the TGS were changed to the wavelength region of interest and the notch was removed. The emission line measurements were synchronised by the TTL signal from the HiPIMS generator, and the internal clock of the camera provided the necessary delay from the start of the pulse. The iCCD detector was gated for 5 μs at 50 Hz and data was accumulated over 20 s (1000 pulses) for both background and plasma measurements. The study concentrated on emission lines in neutral argon (Ar(I)) at 751.47 nm (transition $3s^2 3p^5 (^2P^0_{3/2}) 4p \rightarrow 3s^2 3p^5 (^2P^0_{3/2}) 4s$) and tungsten (W(I)) at 484.38 nm (transition of $5d^4 6s (^6D) 6p \rightarrow 5d^4 6s^2$). These are highlighted in table 4.2. An example spectrum for tungsten is shown in figure

4.12 Assuming a Gaussian fit to the line, a relative intensity could be calculated.

Species	λ **(nm)**	$\mathbf{A}_{ki}$ **(10^7 s^{-1})**	$\mathbf{E}_l$ **(eV)**	$\mathbf{E}_u$ **(eV)**	$\mathbf{E}_i$ **(eV)**
Ar(I)	751.47	4.5	11.62	13.27	15.76
W(I)	484.38	0.19	0.41	2.97	7.98

Table 4.2: Line emission data for the two wavelengths (λ) studied in this work. A_{ki} is the Einstein coefficient for spontaneous emission, E_l, E_u and E_i are the lower, upper and ionisation energies respectively. This table was created using data taken from the NIST Atomic Spectra Database [196].

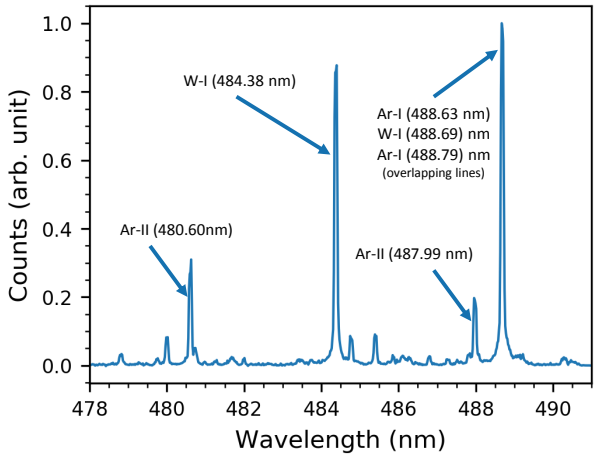

Figure 4.12: An example optical emission spectrum for emission lines in the region 478 nm – 491 nm taken at 10 μs into a HiPIMS pulse. Highlighted is the wavelength of interest of W(I) at 484.38 nm and several other strong emission lines in this region.

Several other lines were also used to track Ar(II) and W(II), but during the afterglow and positive pulse, the selected lines were undetectable and are emitted from this description. Numerous Ar(I) and W(I) lines were also used in preliminary investigations to compare to the selected lines in table 4.2. The trends found were consistent between lines of the same species, giving confidence that the lines are identified correctly, and the emission profiles are representative of instantaneous decay. The emission lines were chosen due to their relative strong intensity, high Einstein coefficients for instantaneous decay (A_{ki}), and they did not overlap significantly with any other strong emissions. The method of extracting a temporal scan was to set the spectrometer at the desired wavelength and alter the

delay of the camera with respect to the HiPIMS pulse. To minimise the transmission loss due to sputtering, the acquisition time was kept low, and each spectrum was normalised to the maximum intensity of that particular species scan. Repeated measurements were made using windows of different opacity (different lifetimes of the removable soda glass) for each wavelength scan to check the consistency of the temporal profiles measured. These were found to be consistent. Experiments were also performed with data acquisition starting at the beginning of the HiPIMS pulse, to the end of the desired temporal scan and vice versa. Co-plotting these scans allowed a quick comparison of the transmission losses due to sputtering in the measurement period. The temporal trends were found to be the same, inferring that this is negligible.

The OES experimental set up required little changes to the TS arrangement and allowed measurements to be made with ease. The normalised intensity scans were interpreted using the Corona model [197], where the intensity of the measured line emission (I) is a function of n_e, ground state density (n_g) and the coefficient of excitation rate Ex_R as a function of temperature (T_e):

$$I \propto n_e n_g Ex_R(T_e) \tag{4.16}$$

This simplistic approach assumes that excitation occurs through electron collisions and de-excite through spontaneous emission, where electron-impact de-excitation is negligible. This is the most common model used in low pressure, low temperature plasma [197]. From this basic model, one can interpret the normalised intensity scans in a qualitative manor. However, no direct comparison of Ar or W emission can be made using this technique, only the tends in their relative temporal scans are measured.

4.3 Emissive Probe

The emissive probe used in this study is described fully in the following section. Briefly, it consists of a 50 μm diameter thoriated tungsten wire, push-fitted into the probe stem, forming a semicircle protruding 2 mm. The tip was Heated until full electron emission was achieved, by a 50 Hz ac current supplied by a transformer circuit with current of 0.80 A. The probe had a spatial resolution of $\sim$ 2 mm and had a temporal resolution of below 100 ns (see section 4.3.2. The error in the plasma potential measurement was of the order of the voltage equivalent of the electron temperature. The emissive probe was fixed to

the chamber through a vaccuum flange, mounted parallel to the magnetron surface. The probe was moved in and out for radial (r-coordinate in figure 4.2) measurements and the magnetron was moved vertically up or down inside the chamber, to allow measurements at different height positions (z-coordinate in figure 4.2).

4.3.1 Probe Design

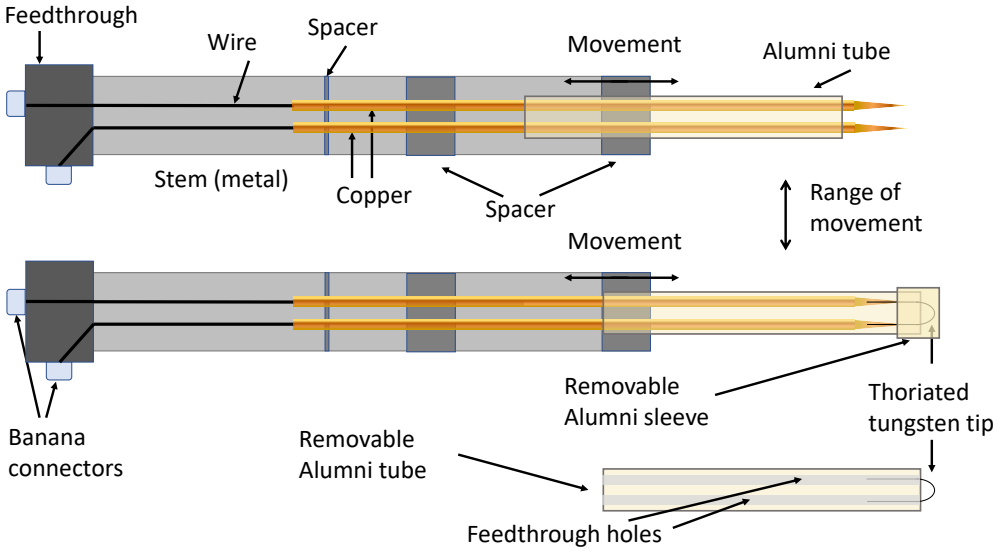

Figure 4.13: A schematic of the emissive probe design

Figure 4.13 shows a schematic of the full emissive probe design, highlighting how the tip attaches to the probe stem. A removable alumni ceramic tube, of diameter 5 mm and length 80 mm, connects the probe tip to the probe stem. The stem had a length of 50 cm and housed the copper wires. The tip consists of a 50 μm diameter thoriated tungsten wire (Goodfellows), formed into a semi-circle, protruding $\sim$ 2 mm out of the sleeve. The ceramic tube was slotted into the stem exposing the copper wires, which allowed the tip to be push fitted into the stem, forming a mechanical electrical connection. The ceramic tube was then pulled outward as to not expose the copper wires to the plasma. This range of movement is highlighted in figure 4.13. Tungsten was the metal of choice for the wire tip due to it's high melting point. The tungsten wire was doped with thorium oxide (0.6%), which reduces it's work function, emitting more electrons and is the most frequently used

emissive probe tip material [177]. A semi-cirlce shaped tip was used to eliminate any kinks which would reduce the lifetime of the probe when heated. The end of the ceramic tube was covered by a removable ceramic sleeve to reduce sputtering of target material on to the tip.

The probe stem housed the copper wires and had had a feed-through connection to the vacuum chamber, sealed through an O-ring. This allowed the probe to be inserted into the vacuum vessel at different positions. The inner probe was sealed using vacuum epoxy resin (Torr seal). The end of the stem had two banana connectors which were connected through a solder connection to the copper wires, which were connected to the heating circuit.

4.3.2 Heating Apparatus

The equipment used in this section is the same as that used by another PhD student (Matt Smith) and is presented in their thesis [198]. For completion, the heating circuit is presented and described in this section. The circuit used to heat and acquire V_p using the floating point method is shown in figure 4.14. It is a two stage transformer circuit, whereby a variable transformer (Zenith Variac) is connected to AC mains at 50 Hz and a second fixed transformer with a 26 turn ratio is isolated from ground. The circuit acts to step down the mains voltage, whilst allowing control of the heating current. The probe is connected to the second transformer using banana sockets (see figure 4.13). As this transformer windings are not in direct contact with the variable transformer (mains source), the probe is isolated from ground potential, allowing it to float. A centre tap was placed on the second isolated transformer, which was then connected to the oscilloscope (Tektronix DPO3034) via a 10 MΩ voltage probe (Tek P6139A). The current delivered to the probe was measured using a multimeter (Fluke 87V Industrial Digital Multimeter) and adjusting the Variac, allowed the current to be increased. This was done until V_f saturated.

This circuit allowed very fast changes in the measured potential to be followed, given that the time constant of the circuit, (τ) is small. Following the calculations done by Fujita and Yagura [199] and Bradley et al [200], it is found, that the time constant is a combination of the resistance across the sheath at the probe (R_S), the impedance of this sheath from the capacitance ($Z_s = 1/\omega C_s$), the capacitance to ground of the circuit (C_c) and the measuring resistance (R_m). Given that R_m is high, yielding a negligible current through it, the time constant is given by [200]:

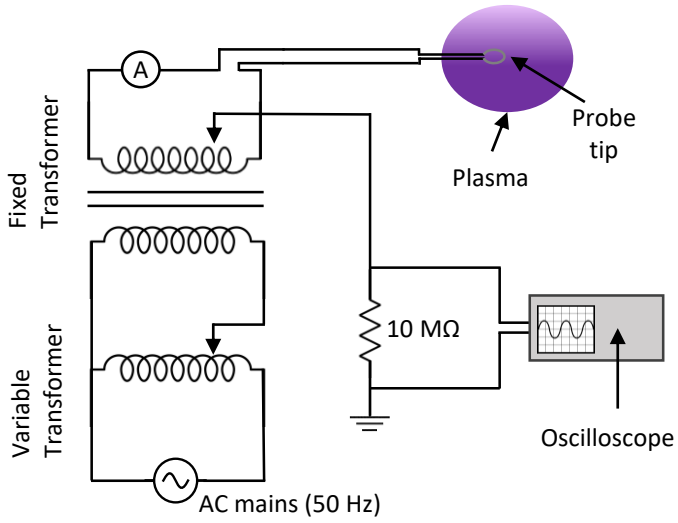

Figure 4.14: The circuit used to heat and measure V_p, showing the two stage transformer circuit, emissive probe and data acquisition apparatus.

$$\tau = \frac{R_s Z_s C_c}{(R_s + Z_s)} \tag{4.17}$$

Bradley et al [200], further found that for a small probe area, (the case in this experiment) C_s is small, resulting in a large Z_s compared to R_s. Which reduces equation 4.17 further. yielding a good estimate of τ to be:

$$\tau \approx R_s C_c \tag{4.18}$$

In this work, this reduction is justified by considering the contributions of R_s and Z_s. Considering the probe tip dimensions and typical plasma parameter values of $n_e = 10^{17}$ - 10^{18} m^{-3} and $T_e = 0.3$ - 3 eV, found in the positive pulse (see TS results in chapter 5). C_s is calculated using the probe area, (A_p) and the sheath distance, (d) which is of the order of the Debye length ($C_s = \frac{\varepsilon_o A_p}{\lambda_D}$). For the probe area and typical Debye lengths in this study, of the order 10^{-5} - 10^{-6} m, typical C_s values are found to be of the order $\approx 10^{-12}$, hence Z_s is large for transient changes in the plasma. R_s can be approximated from the potential drop across the floating sheath (V_s) to an emitting probe and the thermal current of electrons, (I_{es}). The voltage drop over the floating sheath was found to be of

the order $\sim \frac{T_e}{e}$ [177] and I_{es} can be found from:[3]

$$I_{es} = \frac{A_p e n_e}{4} \sqrt{\frac{8 k_B T_e}{\pi m_e}} \tag{4.19}$$

For the conditions stated above, R_s has a range of $\sim$ 10 - 200 Ω. Hence $R_s \ll Z_s$ is satisfied and equation 4.18 is valid. C_c was found from comparing a variable capacitor to the heating circuit. This was done by allowing the probe to float in a bipolar HiPIMS discharge and measuring the rise time of V_f during a positive pulse of magnitude 300 V. The heating circuit was then replaced with a variable capacitor and it's value was altered until the measured V_f profile matched that of the heating circuit. It was found that the heating circuit had an equivalent capacitance of 470 pF to ground. Combining R_s, with the measured C_c, of 470 pF, gives an estimation of τ to be $<$ 100 ns for all measurements performed. Therefore the designed apparatus can accurately follow changes in the measured potential.

4.3.3 Data Acquisition

The emissive probe entry position to the chamber is shown in figure 4.1 and is angled at 45° with respect to the LTS beam. The probe was centred in the chamber using a low powered laser beam which was aligned through the centre of the chamber. To measure radially above the magnetron surface, the probe was pulled out of the chamber relative to this centred position. To measure axial positions, the magnetron was moved vertically inside the chamber. It should be noted that for consistency between measurements, the probe tip was orientated parallel to the magnetron surface and had it's rotation fixed. This ensured that any magnetic field affects altering the probe behaviour would be comparable when changing operating parameters.

Before data acquisition can begin, it was first necessary to identify the heating current required for the measured potential to saturate, hence measuring V_p. After a stable plasma was created, the variac was adjusted to provide increasing current to the probe. For this work, the heating current was found to be sufficient when the potential measured closely follows the voltage overshoot of the positive pulse. This is shown in figure 4.15, for a 300 V, 300 μs positive pulse. The full current and voltage waveform is shown in figure 4.3. The emissive probe in this example was located on the centre-line, 25 mm away from the

[3]This is the same equation as 2.8 and is presented here again for the readers convenience

target surface (r = 0 mm, z = 25 mm). When increasing current is delivered to the probe, the measured potential quickly follows the shape and magnitude of the voltage overshoot, with time periods of the order calculated in section 4.3.2.

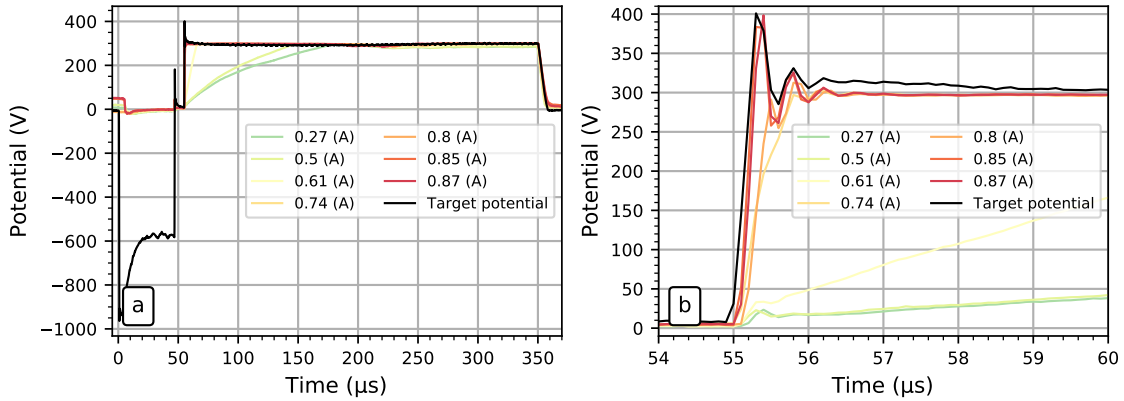

Figure 4.15: An example current calibration plot for a positive pulse of V_{pp} = 300 V of length 300 μs. (a) shows the full target voltage waveform, indicated by the black line and the measured probe potential for successive heating currents. (b) shows a zoomed in plot, highlighting the voltage overshoot period. The data was recorded as a single shot, on the oscilloscope.

To further confirm a fully emitting probe and V_p saturation, plots of the measured potential vs heating current were performed. Examples of these are shown in figure 4.16 for two "stable" time-periods of the plasma discharge. [4] Namely, these are t = 47 μs, a time period in the negative pulse, where the discharge current plateaus and t = 140 μs, a time period where the positive pulse voltage is stable.

As can be seen from figure 4.16, the measured probe potential begins to saturate at around $\sim$ 0.7 A but does not completely flatten. This is due to space charge effects increasing the effective collection area of the probe. As aforementioned, emissive probes using the floating technique typically float 1 - 1.5 T_e below V_p. In this specific example, the selected heating current was 0.8-0.85 A. This was a compromise between full emission (i.e the ability to track quick potential changes) and the probe life-time. It should be noted that this calibration procedure was performed for each new probe tip and measurement location. Once the probe had been found to saturate and the selected current range had been found, data can be saved using the oscilloscope and the temporal evolution of V_p

[4] Any changes in plasma potential between separate HiPIMS pulses, will provide errors in this method.

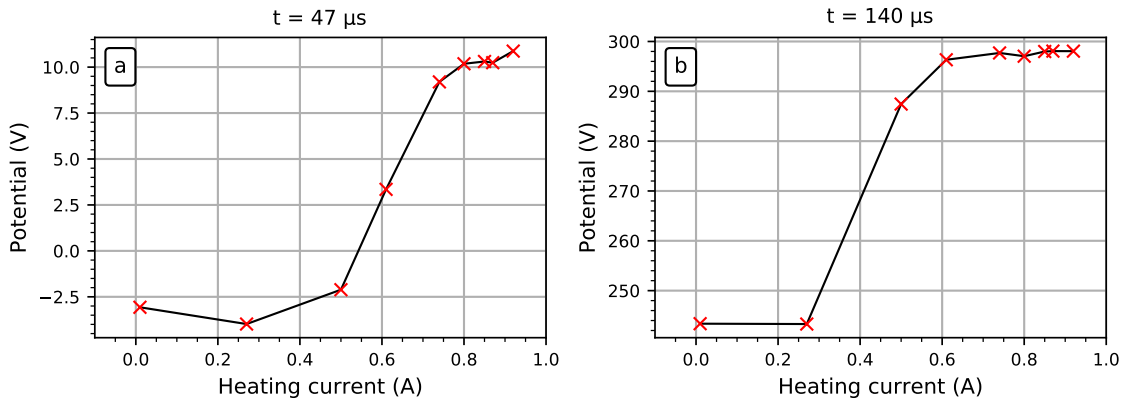

Figure 4.16: An example current calibration plot for the same conditions as in figure 4.15 at times (a) t = 47 μs, and (b) t = 140 μs. Shown here is the measured potential vs applied heating current.

can be inferred. In this work, data was averaged over 128 pulses. Frequent single shot acquisitions were also taken to check for consistency.

A final note is on the B field influence on measured V_p. It is possible that electrons released from the probe return due to magnetic field intersection, and affect the measured V_p. In this work, the orientation of the probe was fixed relative to the magnetron surface, however, due to the shape of the magnetic field, this did not result in a uniform field line intersection with the probe tip. A brief experiment was performed rotating the probe at full emission and comparing the measured V_p at 3 different angles of 0°, 45° and 90° parallel to the magnetron surface. This was done on the centre-line, close to the target (z = 15 mm), where the field is roughly at it's strongest. It was found that between differing probe orientations, the measured temporal V_p was in the range $\sim$ 2 -3 V of one and other throughout the bipolar HiPIMS pulse. This is an acceptable range, within accuracy of the probe. Measuring further away from the target will cause less of an effect as the magnetic field is weaker. Similar studies have concluded that the orientation of the probe does not effect the measured V_p significantly [200, 201]. The focus in this work was on the trends of V_p temporal evolution, rather than absolute values. For these reasons, magnetic effects due to probe alignment were deemed negligible.

4.4 2D Imaging

The experimental set up and data collection methods of the 2D imaging apparatus used in this study is described fully in the following section. The set up is relatively simple, with little alterations needed to take images. An iCCD camera was mounted on an optical rail in the location marked on figure 4.1 and was triggered by the TTL signal of the HIPIMS generator. The work done here used the full optical range of the iCCD and as such, the captured images are broad band rather than specific wavelengths.

4.4.1 Experimental Arrangement

A secondary iCCD camera (Andor istar DH334T-18U-C3), fitted with a 105 mm DG macro lens (sigma EX) was used to take time-resolved images of broad band optical emission of the plasma throughout the positive pulse on-time. The camera was mounted on a metal stand connected to an optical rail on the optical bench, which ensured the height of the camera was the same height as the magnetron window. The optical rail allowed the camera to be moved back and fourth, until the desired imaging area was found. The camera had an optical range of 200 - 940 nm and was focused on an object of known size, centred with respect to the magnetron inside the chamber. Figure 4.17, shows an example image taken during a focusing experiment. Here, a white plastic cuboid with circular grooves embedded on it's front facing surface was used to focus the camera optics. The cuboid had dimensions 20 x 20 x 20 mm^3 and was mounted onto the end of the emissive probe, centred by a low powered laser beam, aligned through the centre of the chamber. The camera lens was at a distance $\sim$ 1 m away from the centre of the chamber (cuboid).

To illuminate the otherwise dark chamber, a torch was shone inside the chamber for alignment/focusing purposes. This can be seen in figure 4.17 by the dark region in the bottom right hand corner. To avoid over-saturation of the iCCD, an image was taken using low exposure and no gain. In the case of figure 4.17, data was acquired over 0.1 s in the single scan mode (i.e one image taken with exposure 0.1 s). The captured image on the iCCD was inverted and had to have its vertical axis flipped. The camera had a pixel array of 1024 x 1024 and by using the focused square target, the conversion between pixels and image size can be found. The front facing side of the cuboid spanned over 188 pixels in both the x and y spatial axis, which gave a conversion of 1 pixel = $\frac{20x10^{-3}}{188} \approx 106$ μm (or equivalently, 1 mm = 9.4 pixels). This resulted in full images of dimensions $\sim$ 11 x 11 cm to be captured. Moving the camera further back with respect to the chamber, would have

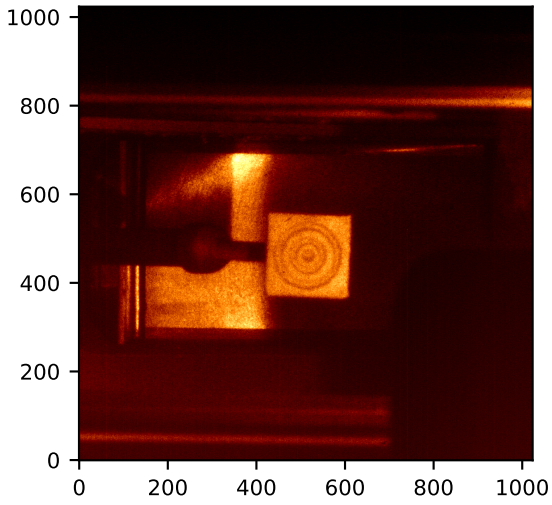

Figure 4.17: An image taken using the iCCD during the focusing procedure, with square target centred inside the vacuum chamber. The camera had a pixel array of 1024 x 1024.

allowed a larger image to be captured, however, this was not done as, spatial resolution would have been lost and efforts were made to avoid capturing the mechanical shutters, or reflections off of surfaces at the entrance port.

4.4.2 Data Acquisition and Analysis

After alignment and focusing of the camera had been achieved, images were taken. Initially, the shutters to the viewing port were closed and a stable plasma was created. Using the Andor Solis software, the camera was cooled to -30° and the lights of the laboratory were turned off, to minimise noise and ambient light in the signal. The shutters were then opened to allow the plasma to be viewed by the camera. Images were taken during the positive pulse with a gate width of 2 μs and acquired over 2 s (100 plasma pulse), synchronised by the TTL signal of the HiPIMS generator. The internal clock of the iCCD provided a delay that allowed temporal measurements to be made. Before each temporal scan, a preliminary scan was taken with no applied intensifier gain and low exposure time. This identified where, temporally, the brightest (most intense) images are expected to be found. Once this had been located, the gain of the camera was increased carefully, to not over-saturate or damage the iCCD, using the brightest time period found from the preliminary scan. The gain used during experiments was in the range 1000 - 2500, but

during a temporal scan was fixed at the selected gain for all temporal data acquisition. This allowed temporal images to be compared to one and other.

Chapter 5

Laser Thomson Scattering and Optical Emission Spectroscopy Investigation[1]

5.1 Introduction

Despite the excellent work to date in measuring the plasma parameters in asymmetric bipolar HiPIMS plasmas, as described in section 2.1.5.2, many of the probe and analysis techniques can be highly perturbing to the plasma, thus affecting results, or making interpretation difficult. In this chapter, the temporal evolution of electron properties in a bipolar HiPIMS discharge has been determined using laser Thomson scattering (LTS) for a range of argon pressures and positive voltage profiles, namely positive pulse height and duration. Measurements have been performed on the centre-line and above the main erosion groove of the magnetron (see section 4.2.4 for geometry details). As shown in section 4.2.6, the LTS technique is non-intrusive and, in the limit of incoherent scattering [174], allows the determination of the electron temperature T_e through acquisition of the electron velocity distribution function, and electron density n_e from the intensity of the scattered radiation. The LTS system has good spatial and temporal resolution (5 μs and 3.33 mm respectively), straightforward interpretation of the obtained spectra and easy to perform absolute density calibration.

[1]Some of the research presented in this chapter has been published in two peer-reviewed journal articles [1, 2] and have been reproduced for this thesis.

LTS has been used to determine the time-evolution of electron properties in HiPIMS [100, 102, 103] and DC [101] magnetron discharges. At the time of writing this thesis, this is the first LTS study of the asymmetric bipolar HiPIMS plasma, and the focus of this section is on how the positive pulse affects the electron density and temperature during the afterglow period. The LTS studies are complemented by optical emission spectroscopy to determine the temporal evolution of the important gas and metal emission line Ar(I) and W(I).

It should be recognised that some of the results presented in this chapter have been published [1, 2] and have been reproduced for this thesis.

5.2 Experimental Arrangement, Plasma Source and Diagnostics

The experimental arrangement including the vessel, magnetron and LTS system is detailed in chapter 4. In this study, discharges were operated at two pressures, 0.8 Pa and 1.6 Pa. These were driven by the in house built asymmetric bipolar generators. Example voltage and current waveforms used in this work are shown in figure 5.1 for a variation of positive pulse voltages and durations. In total, 3 positive pulse magnitudes were diagnosed in this work: 100, 200 and 300 V. The comparable unipolar case, with no positive pulse were also diagnosed. In each case an average pulse energy, power, and peak target power density of 1.8 J, 85 W $\sim$ 230 Wcm^{-2}. All discharges produced had a fixed repetition rate of 50 Hz and negative pulse length of $t_{np} = 50$ μs. One can see from figure 5.1 that increasing the positive pulse voltage and duration can marginally increase the current rise time and reduce the peak current during the negative pulse (main sputtering phase). As will be shown later, this may be due to lower residual electron densities being available in the afterglow to aid ignition of the next pulse when large positive pulses are utilised. The insert plot for current shows reverse negative currents of up to about 5 A to the cathode are generated when positive voltages are applied.

The magnetron anode ring protruded $\sim$ 7 mm from the target surface, therefore measurements no less than 15 mm from the target were made, to minimise stray light reflections entering the detection system. Time-resolved measurements were achieved by synchronising the laser, iCCD and plasma source (see section 4.2.5). Data was accumulated over 600–3000 laser pulses (60–300 s), with longer acquisition time needed to improve the sig-

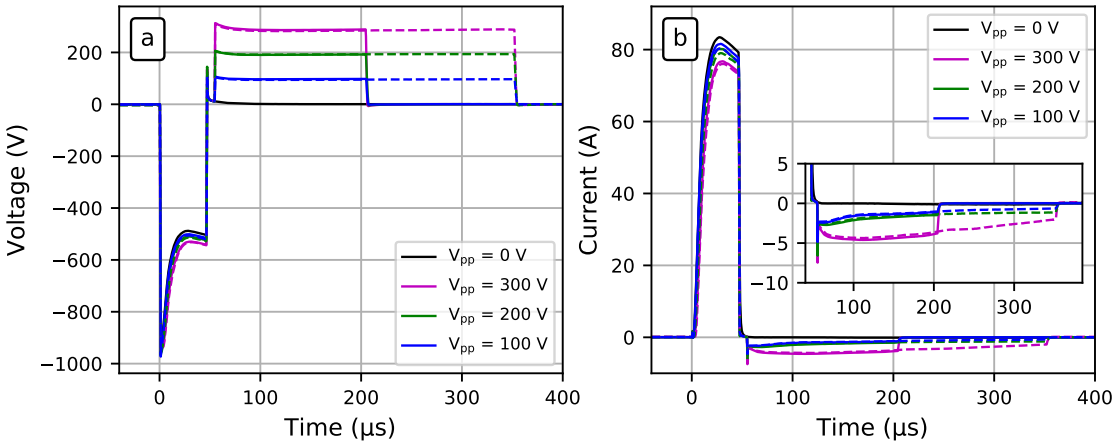

Figure 5.1: Example discharge voltage (a) and current (b) waveforms. The black curve represents the waveform of a uni-polar pulse of width 50 μs. Blue, green and magenta curves represent discharges with 150 μs (solid line) and 300 μs (dashed line) duration positive pulses of 100, 200 and 300 V respectively. The pulse cycle repetition rate is 50 Hz with an operating pressure of 1.6 Pa.

nal to noise ratios of low electron density and high temperatures measured during the positive pulse. The temporal resolution of this system was 5 μs.

The spectral resolution of the TS system was approximately 0.071 nm. The data outside of the notch filter region (531.5 -532.5 nm) is fitted to a Gaussian function to obtain the electron temperature. In this arrangement, the instrument could resolve electron temperatures down to 0.12 eV, and hence measurements into the deep afterglow of the HiPIMS pulse were not possible. Typical errors on the measured T_e values are in the range 2-6 %, found from the standard deviation of the Gaussian fit parameters. The absolute electron density was obtained through a calibration procedure by means of Rayleigh scattering from room temperature argon gas of known density. Typical errors on the measured n_e values are in the range 2-12 % found from the standard deviation of multiple Rayleigh scattering measurements at several pressures and propagation of errors from the Gaussian fit of the TS spectra.

Optical emission line data from the discharges was obtained using the triple grating spectrometer, however in this case with a small aperture of diameter 3 mm placed behind the collection lens to limit the solid angle of collection and the entrance slit changed to 0.1 mm to improve the spectral resolution. The emission line measurements were synchronised

by the TTL signal from the HiPIMS generator, and the internal clock of the camera provided the necessary delay from the start of the pulse. The ICCD detector was gated for $5\mu s$ at 50 Hz and data was accumulated over 20 s (1000 pulses) for both background and plasma measurements. The study concentrated on emission lines in neutral argon at 751.47 nm (transition $3s^2 3p^5(^2P^0_{3/2})4p \rightarrow 3s^2 3p^5(^2P^0_{3/2})4s$) and tungsten at 484.38nm (transition of $5d^4 6s(^6D)6p \rightarrow 5d^4 6s^2$). An example spectrum for tungsten was shown in figure 4.12, assuming a Gaussian fit to the line, a relative intensity was calculated.

The results presented in this chapter are separated in to two sub-sections, which describe measurements of plasma electron properties and optical emission, organised into their radial position with respect to the magnetron geometry: centre-line and above the racetrack respectively. To highlight the durations of the negative (t_{np}) and positive (t_{pp}) pulses, the figures are shaded with grey and blue regions respectively.

5.3 Centre-line Results

In this study[2], measurements of electron plasma properties and plasma emission were made for a range of discharge conditions, in order to understand the effect of the positive pulse on plasma behaviour. Plasmas were struck at two pressures, 0.8 Pa and 1.6 Pa (typical HiPIMS operating pressures). The pulse frequency was held at 50 Hz and the on-time t_{np} was kept constant at 50 μs. The positive voltage pulse durations and heights were varied, namely t_{pp} = 150 μs and 300 μs and V_{pp} = 0, 100, 200 and 300 V respectively. V_{pp} = 0 V case is just the normal unipolar HiPIMS case where no reverse pulse was added to the voltage signal. The delay between the negative and subsequent positive pulse was fixed at 8 μs.

5.3.1 Temporal Evolution of Electron Temperature and Density

In this section, the results of LTS measurements are presented in order to understand how the addition of the positive voltage pulse affected the temporal evolution of the electron plasma properties . Figure 5.2 shows the temporal evolution of T_e and n_e at the position of the magnetic null, z = 61 mm, with t_{pp} = 150 μs for the four V_{pp} cases. From figure 5.2 (a), a clear rise in electron temperature during the positive pulse period for the V_{pp} = 300 V case is present, with T_e starting to rise about 120 μs after positive pulse ignition from

[2]The results in this section have been presented in a peer reviewed journal [1].

0.44 eV to a peak of 0.93 eV. No such increase was seen for the other two positive pulse cases. This electron heating is rapidly terminated as the target is grounded at the end of the reverse voltage period at t = 208 μs, and is followed by cooling but with T_e values always higher than the other V_{pp} cases. These higher T_e values in the long afterglow are accompanied by lower electron densities as shown in figure 5.2 (b). That is, the density of these hotter electrons is decaying much faster once the target voltage rapidly transitions from a finite V_{pp} value to ground.

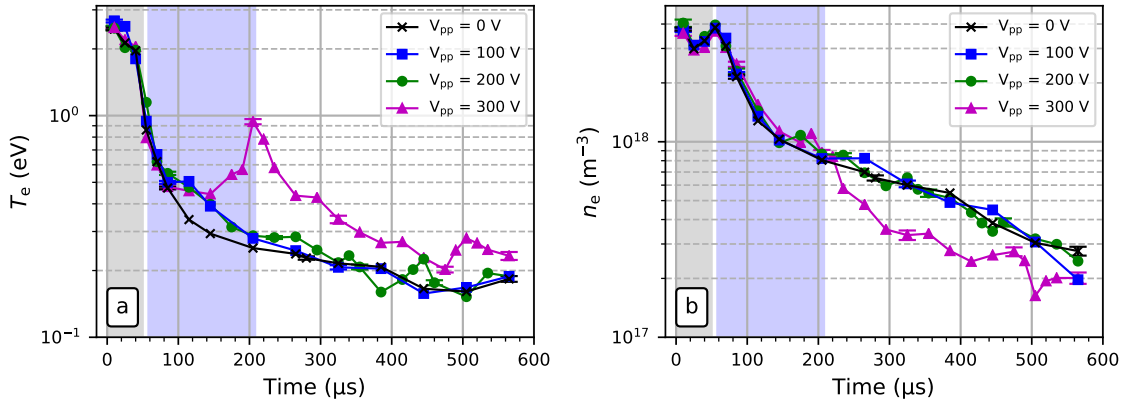

Figure 5.2: Plots of (a) the electron temperature T_e and (b) electron density n_e versus time at position z = 61 mm, for a negative pulse duration of t_{np} = 50 μs (grey region), positive pulse duration of t_{pp} = 150 μs (blue region) for V_{pp} = 0, 100, 200, and 300 V. The operating pressure was 1.6 Pa

Figure 5.3 shows what effect a lengthening of the positive pulse period had, with t_{pp} increased to 300 μs, with all the other operating conditions remaining fixed. In the V_{pp} = 300 V case, electron heating can now persist for longer with T_e peaking at t $\sim$ 240 μs with a value of $\sim$ 2.6 eV. This is followed by slow cooling in the remainder of the positive pulse period and the long afterglow. In contrast to results in figure 5.2 the V_{pp} = 200 V now does reveal a T_e rise but much delayed compared to the V_{pp} = 300 V case. The T_e heating is terminated by the end of the positive voltage period. Clearly, the higher the positive pulse voltage, the sooner the T_e rise occurs. For positive pulse voltages of V_{pp} = 100 V no T_e rise is seen at all, although this may happen for much longer t_{pp} duration's not explored here (see section 6.3). The electron density-time curves in figure 5.3 (b), show that, in the cases where electrons are heated their densities decrease more rapidly in the long afterglow, the phase where the target voltage goes to ground. Interestingly, there was

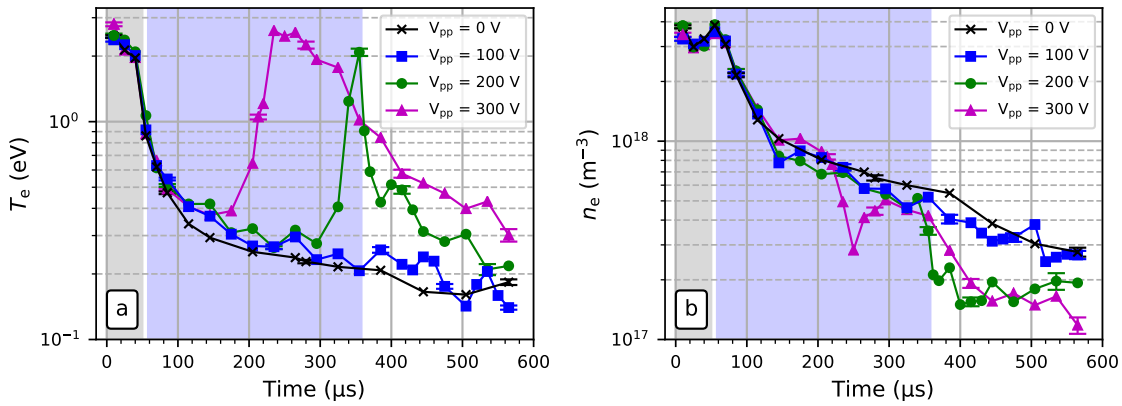

Figure 5.3: Plots of (a) the electron temperature Te and (b) electron density n_e versus time at position z = 61 mm for the same operating conditions as in figure 5.2 but with a positive pulse duration increased to t_{pp} = 300 μs.

a pronounced sharp dip in n_e in the afterglow t = 250 μs when the positive pulse of 300 V is applied. Figure 5.3 reveals that with high V_{pp} values, i.e 300 V, the electron temperatures in the whole of the afterglow are significantly raised compared to the conventional unipolar equivalent pulse where V_{pp} = 0.

The effect of halving the pressure from 1.6 Pa to 0.8 Pa on the T_e and n_e temporal profiles at position z = 61 mm is shown in figure 5.4 for the two positive pulse lengths, t_{pp} of 150 and 300 μs and V_{pp} = 300 V. High pressures lead to higher on-time electron densities (increase of 20 - 30 %) and lower electron temperatures at the end of the negative pulse (2.0 eV as opposed to 2.4 eV) as may be expected. For cases with no positive pulses applied (V_{pp} = 0 V), the electron temperatures were lower in the afterglow for lower pressure. With the application of a positive pulse, the peak in electron temperature was delayed for the higher pressure case and for t_{pp}= 300 μs, the heating at higher pressure takes longer to decay compared to the lower pressure discharge. After termination of the positive pulse, densities at both pressures decay quicker in comparison to the unipolar (V_{pp} = 0 V) case, with the P = 0.8 Pa showing the most exaggerated drop in density, thought to be due to the fact that there are less collisional processes, meaning the plasma can diffuse and escape the target vicinity.

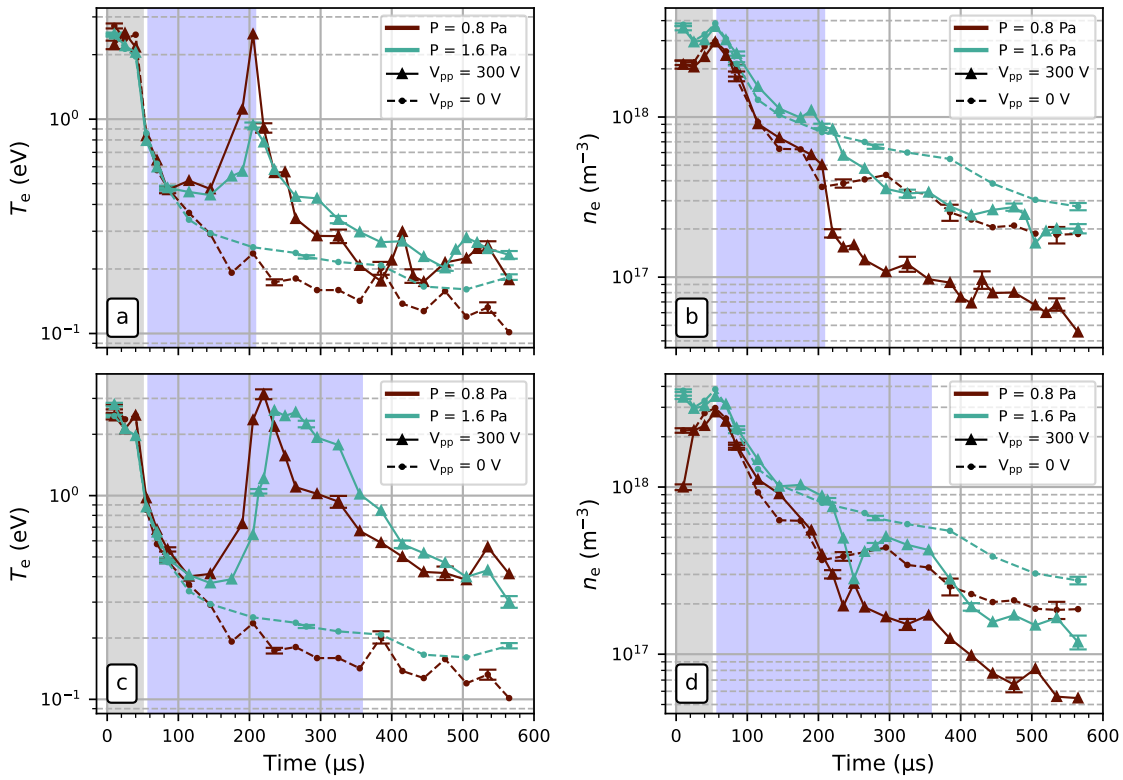

Figure 5.4: a-d. Plots of the electron temperature T_e (a,c) and electron density n_e (b,d) versus time measured at position z = 61 mm for a variation of positive pulse length and operation pressure. t_{pp} = 150 μs for plots a and b. t_{pp} = 300 μs for c and d. The two operating pressures are indicated in the legend.

The spatial variation of T_e and n_e were explored by making measurements closer the magnetron target, namely at position z = 15 mm, a scattering volume also on the discharge centre-line. This is the closest possible distance to the magnetron without suffering a significant stray light increase due to light reflections from the magnetron anode ring. Figure 5.5 shows the measured z = 15 mm position values of T_e and n_e values at an operating pressure of 1.6 Pa with t_{np} = 50 μs, t_{pp} = 300 μs for V_{pp} = 0 and 300 V. Plotted together on the same axis are those at z = 61 mm as a comparison (this data is also in figures 5.2, 5.3). At the closest distance to the target, for the z = 15 mm position, T_e was much lower during the negative driving pulse region of the HiPIMS discharge than those measured at z = 61 mm, irrespective of the positive pulse conditions, with T_e peaking at

about 1 eV rather than $\sim$ 2.4 eV. However, just into the afterglow regions (first 50 -100 μs) in all cases the T_e values were comparable and decay similarly. As seen at position z = 15 mm with a positive pulse of V_{pp} = 300 V significant transient electron heating was seen with T_e values peaking at 3 eV, a value marginally higher, but slightly delayed in time compared to measurements at z = 61 mm. As aforementioned, the electron density measurements for the V_{pp} = 300 V positive pulse case, measured at z = 61 mm, shows an unusual sharp dip in the afterglow at t = 250 μs, it somewhat mirrors the sharp peak in n_e at 270 μs seen in the same discharge measured at z = 15 mm. If these features are related, it shows an effect happens first at the magnetic null, then close to the target.

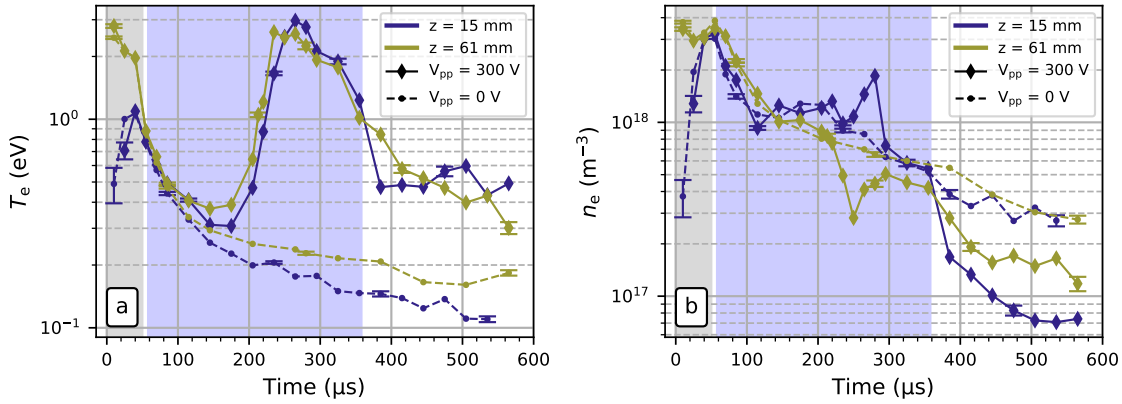

Figure 5.5: Plots of the electron temperature T_e (a) and density n_e (b) versus time measured at position z = 61 mm and z = 15 mm, for t_{pp} = 300 μs for V_{pp} = 0 and 300 V at an operating pressure of 1.6 Pa.

5.3.2 Temporal Evolution of Ar and W Optical Emission Lines

In this section, optical emission spectroscopy results are presented to complement the electron property results and to shed light on the main physical processes occurring in the positive pulse regions of the bipolar pulse regime, the study was conducted focusing on the dominant neutral lines for electronically excited argon, Ar(I) (λ = 751.47 nm) and tungsten W(I) (λ = 484.38 nm). No significant lines from ionised species Ar(II) and W(II) were detectable outside the negative pulse period of the HiPIMS discharge. To minimise the transmission loss due to sputtering, the acquisition time was kept low and to quantify the intensities, each spectrum was normalised to the maximum intensity of the temporal

scan of the particular species to produce a relative intensity for each.

Figure 5.6 shows the Ar (I) and W (I) relative intensities for (a) at position z = 15 mm and (b) at position z = 61 mm for the discharge conditions of t_{np} = 50 μs, V_{pp} = 300 V, t_{pp} = 300 μs with operating pressure of 1.6 Pa. Also plotted here is the LTS obtained electron temperature for the two corresponding discharges for comparison.

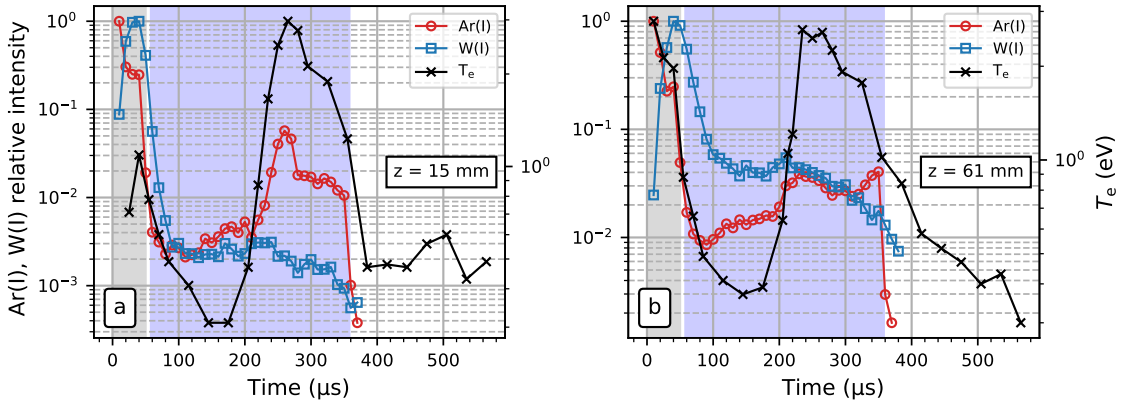

Figure 5.6: A plot of the temporal evolution of the Ar (I) and W (I) line intensities at z = 15 mm (a) and z = 61 mm (b) respectively together with the LTS obtained electron temperature for the case V_{pp} = 300 V, t_{pp} = 300 μs with a pressure 1.6 Pa obtained at positions z = 15 mm and z = 61 mm

During the negative voltage region of the HiPIMS pulse, the W (I) line intensity increased and the Ar (I) line decreased as the pulse evolves in time, consistent with the expected transition from an argon gas to tungsten metal dominated discharge regimes. It is clear from the plots at both positions that the Ar intensity profile follows the electron temperature. As T_e peaks in the positive pulse period so does the Ar line intensity. During this phase the electron density is falling (see figure 5.3), while the background neutral argon density is expected to increase as the argon streams back into the target region after rarefaction in the negative pulse [202]. This is evident in figure 5.6 between times 100 and 200 μs, as Ar increased whilst T_e decreased. The greater excitation of neutral argon by hotter afterglow electrons despite the fall in n_e leads to more light intensity. Just after termination of the positive pulse when the electrons cool rapidly the Ar (I) emission fell almost instantaneously below the threshold for detection.

The behaviour of the W (I) line intensity was somewhat different. It was constant during the first half of the positive pulse, but as T_e rises it decreases (unlike Ar (I) emission),

before falling to undetectable levels immediately after the positive pulse termination. This indicates that the neutral tungsten density may be falling during the same period as T_e rises. However, line intensities are very sensitive to changes in electron density and since n_e is falling in the same period, it is hard to speculate on exactly why the W (I) line intensities fall during electron heating.

In a number of HiPIMS experiments, it was found that thermalised metal atoms can remain in the discharge for considerable periods, persisting for hundreds of μs after pulse termination in the afterglow [203–205]. High densities of low energy W ions are trapped in the magnetic tunnel by the cathode sheath, with subsequent charge exchange collisions and elastic collisions reducing their energy further. Therefore, significant amounts of tungsten may be present near the target in the off time. However, following the Thompson distribution (see section 2.1.1.1), the most probable kinetic energy of sputtered neutrals is half the surface binding energy, therefore, most of the W atoms coming from the sputtering period will have exited the discharge within 40 μs. This was found from a simple calculation based on the most probable kinetic energy of sputtered neutrals to be of 11.8 eV [206], travelling a distance of 10 cm from the target. For high V_{pp} a new source of W could be from the grounded vessel walls.

During the on-time, target sputtered W will deposit on the walls. During the positive pulse period, the plasma potential is elevated to a value close to V_{pp} (see chapter 6), and so argon ions from the plasma can effectively sputter the walls through energetic bombardment, in the case shown in figure 5.6 with energies up to 300 eV. As the argon ion densities decay in the positive pulse period, where the plasma is not sustained from target processes, any new source of W from the sputtering of chamber wall material must necessarily fall. It is important to note that without the positive pulse present, no significant trace of Ar or W emission is detected in the afterglow. Energetic argon ion bombardment of the walls in the positive pulse period of the afterglow would liberate secondary electrons that are sheath accelerated to enter the plasma, with energies equivalent to V_{pp} and become thermalised in the decaying plasma. To investigate if the wall sheath potentials can, in the positive pulse period, influence the short- lived wall (re)sputtering and secondary electron release (leading to bulk heating) the temporal W (I) and Ar(I) intensities have been plotted for $V_{pp} = 0$, 100, 200 and 300 V in figure 5.7 (a) and (b) respectively.

In the absence of a positive pulse ($V_{pp} = 0$) both Ar (I) and W (I) lines decayed quickly in the afterglow falling below the detection limit at $t \sim 120$ μs. The $V_{pp} = 100$ V is similar however, W (I) emission persists to $t \sim 150$ μs. For higher positive pulse voltages, the W

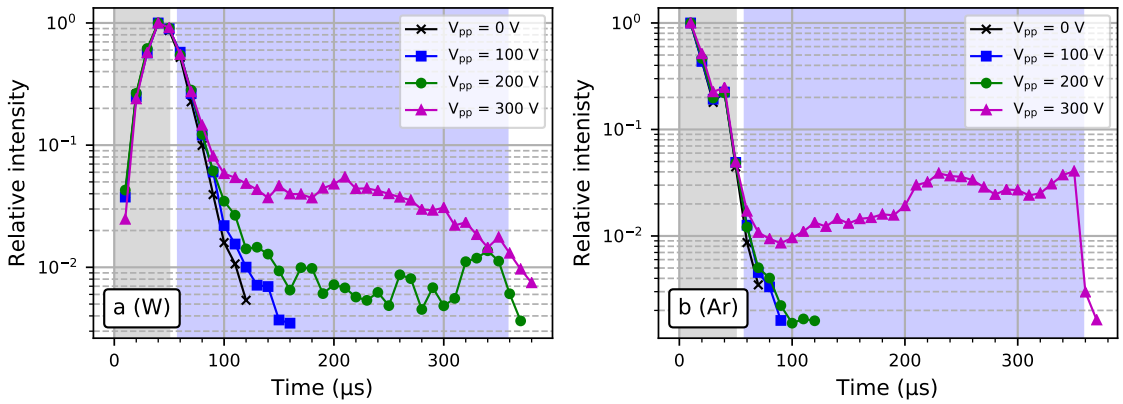

Figure 5.7: A plot of the temporal evolution of (a) W(I) and (b) Ar(I) line intensities for t_{pp}= 300 μs for changing positive pulse voltages V_{pp} = 0, 100, 200 and 300 V and P = 1.6 Pa measured at position z = 61 mm.

(I) line intensities remain strong for the whole pulse period with V_{pp} = 300 V revealing a larger signal consistent with broader peak T_e values as shown in figure 5.3. The gradual decay in W (I) line intensity is consistent with a decay in the density of source tungsten atoms originating from the walls, in the afterglow plasma. Ar (I) emission is only seen in the positive pulse period for the V_{pp} = 300 V case, a situation where transient but significant electron heating is occurring in the plasma.

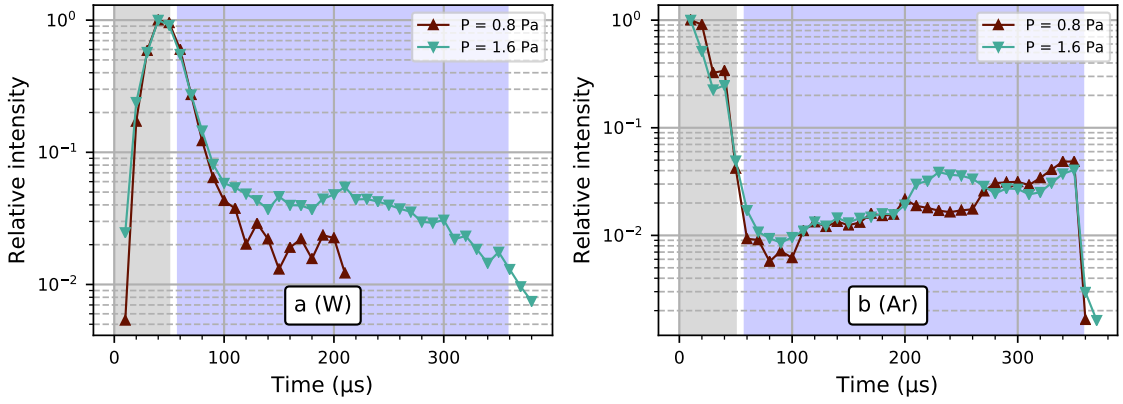

Figure 5.8: A plot of the temporal evolution of (a) W(I) and (b) Ar(I) line intensities, for t_{pp} = 300 μs for changing pressure for V_{pp} = 300 μs.

To examine what effect pressure has on the intensity of excited species in the discharge, measurements were performed at a lower pressure of 0.8 Pa as used previously in the LTS study. Data was collected at position z = 61 mm and figure 5.8 shows the effect of changing pressure on the chosen emission lines. For the 0.8 Pa case, the W (I) emission in the positive pulse becomes undetectable at $\sim$ 220 μs whereas at 1.6 Pa it persisted throughout. The Ar (I) plot shows that at both pressures, the emission is present in the positive pulse and increases towards the end before falling to zero after the positive pulse termination.

5.4 Racetrack Results

To complement the results in the previous section, which showed significant electron heating along the discharge centre-line in the positive pulse period, LTS and OES results made in a line above the racetrack are presented. The laser beam propagation was in the target surface plane. Moving the magnetron, up or down relative to the fixed laser beam alignment through the chamber, allowed axial measurements to be performed. The laser beam was focused in scattering volumes on an axial line at radius r = 48 mm (above the main erosion groove) at distances 15 mm to 65 mm from the target, in steps of 10 mm. The laser scattering vector ($\mathbf{k} = \mathbf{k_s}\text{-}\mathbf{k_i}$), was aligned perpendicular to the magnetrons magnetic B field. This corresponds to the component of the electron velocity distribution measured (see figure 4.10). Data was accumulated over 600 - 3000 laser pulses (60 – 300 s).

5.4.1 Temporal Evolution of Electron Temperature and Density

Initially the interesting case of a bipolar HiPIMS discharges with V_{pp} = 300 V and t_{np} = 50 and 300 μs are reported as an extension to the previous centre-line measurements. Figure 5.9 (a) and (b) respectively shows the temporal evolution of electron temperature T_e and density n_e for the 6 axial measurement positions above the racetrack plotted on the same axis.

From figure 5.9 (a), a rise in T_e during the positive pulse at all positions was present. The rise was seen to occur sooner, at positions further from the target, also reaching higher values. T_e peaks at a value of 2.2 eV at the z = 65 mm whilst at z = 15 mm the temperature only reaches 0.25 eV. This indicates there is a region of hot plasma some distance away from the target. The corresponding density plots, figure 5.9 (b), showed a significant drop in the middle of the magnetic trap during this heating phase. Positions close to and far

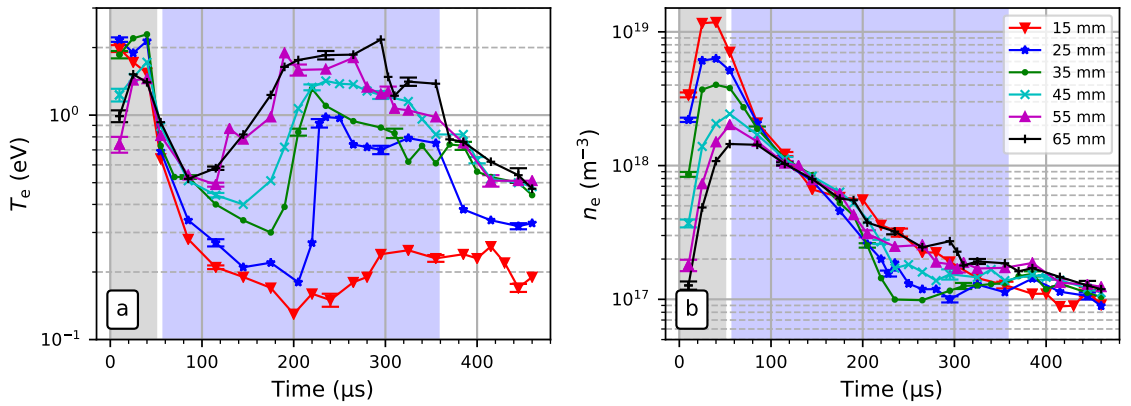

Figure 5.9: Plots of (a) the electron temperature T_e and (b) electron density n_e versus time at several position above the racetrack (r = 48 mm) with a positive pulse of V_{pp} = 300 V. The negative pulse duration t_{np} = 50 μs (grey region), positive pulse duration t_{pp}= 300 μs (blue region). The operating pressure was 1.6 Pa

from the target show the least density reduction in the positive pulse.

Figure 5.10 shows the data presented in figure 5.9, co-plotted with the comparable unipolar discharge electron properties. The data is separated into two subplots, indicating whether the measurement positions were inside or outside of the magnetic trap (see figure 4.2 for the location of the last closed flux surface). The electron temperature and electron density at the corresponding measurement positions are presented in columns. For the readers convenience, the data in each subplot is labelled with either "Bipolar" or "Unipolar".

Most notably from these plots are the large differences between measured densities during the positive pulse duration compared to the unipolar counterpart. The density inside the magnetic trap at z = 35 mm shows the largest difference, with an approximate 5 fold comparative density decrease. On the centre-line, no such density reduction was observed. There is a striking difference in T_e for the bipolar case in which large deviations from unipolar operation are present during the positive pulse. Close to the target (data shown in 5.10 (d)), T_e roughly follows the standard temperature decay found in the unipolar case, until the latter stages of the positive pulse, where T_e is measured to increase. Further away from the target the deviation happened sooner. Clearly, the conditions in the discharge had significantly changed in the positive pulse afterglow compared to unipolar operation.

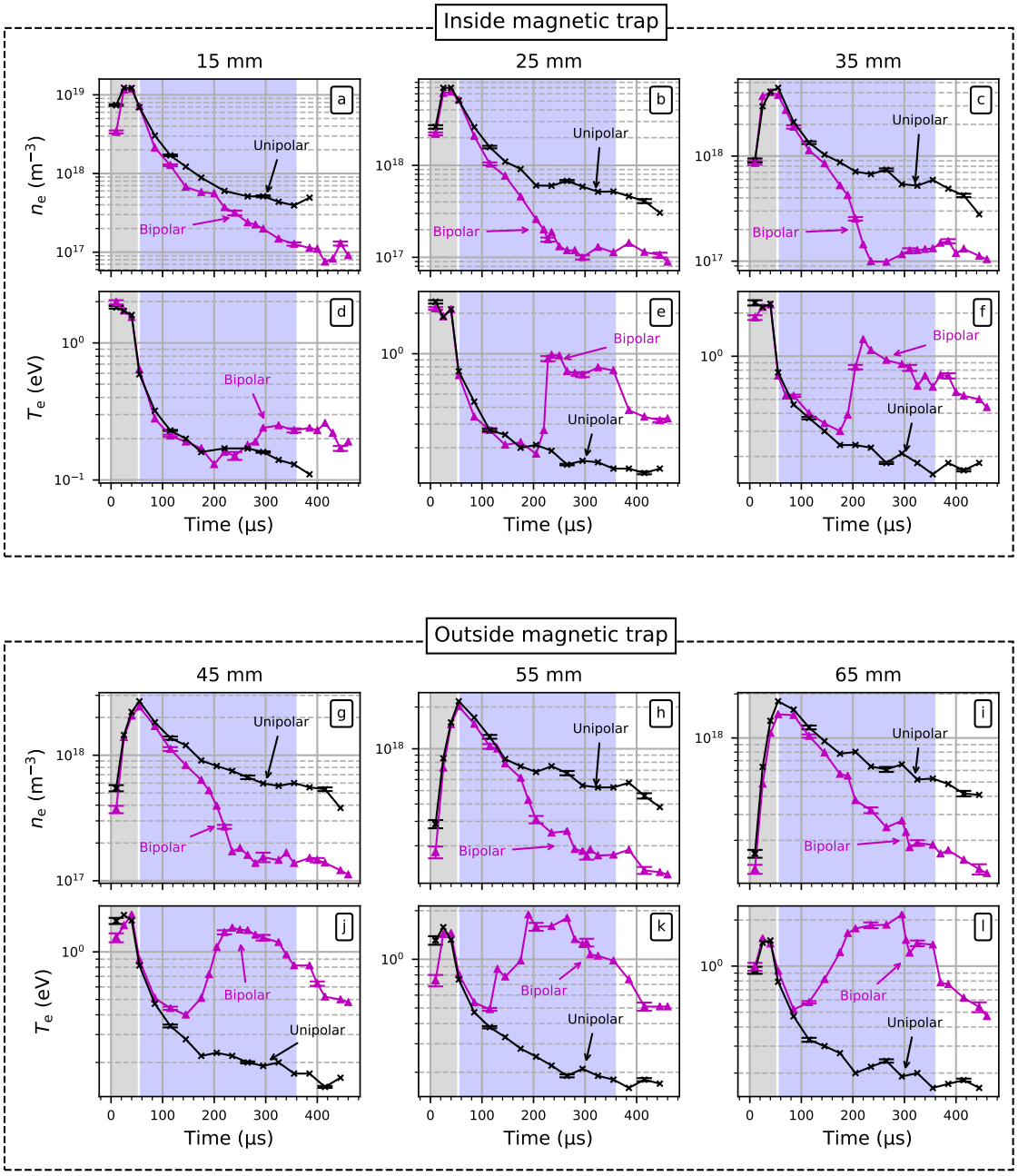

Figure 5.10: Comparison of figure 5.9 data, with the comparable unipolar HiPIMS case. The figure is split into two subplots indicating whether the measurement position was located inside or outside the magnetic trap.

The results indicated that hot plasma is present which is spatially asymmetric above the racetrack, with hotter temperatures measured further away from the target. Interestingly, temperature deviations arise sooner further away from the target.

To obtain a broader picture of the heating phenomenon and electron density reduction above the racetrack on application of the positive pulse, LTS measurements have been made for positive voltages V_{pp} of 100, 200 and 300 V at r = 48 mm and z = 35 mm. These are shown in 5.11, together with the unipolar V_{pp} = 0 V case.

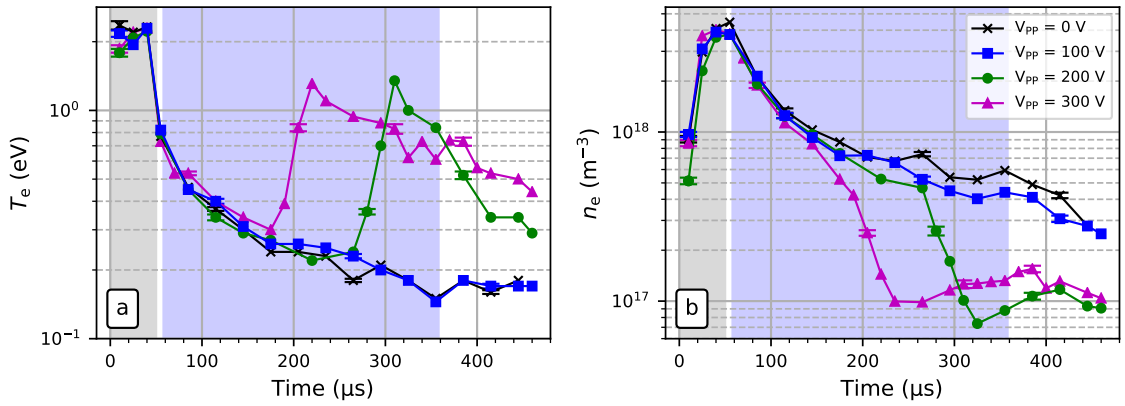

Figure 5.11: Plots of (a) the electron temperature T_e and (b) electron density n_e versus time measured in the centre of the magnetic trap (r = 48 mm, z = 35 mm) for V_{pp} = 0, 100, 200 and 300 V with all the other operating conditions the same as in Figure 5.9

Similar to the centre-line results, there was no measured T_e increase for the V_{pp} = 100 V case during positive pulse delivery. The V_{pp} = 200 V case shows a T_e increase towards the end of the positive pulse. The timings of this T_e rise is in line with what was measured centre-line (figure 5.3). The temperature rise occurred some 100 μs sooner with V_{pp} = 300 V than the 200 V case. With V_{pp} = 300 V the fall in electron density in the trap is most dramatic. With application of V_{pp} = 100 V there is little or no change in the n_e decay profile compared to the unipolar case. It is clear that for voltages greater 100 V the electrons become significantly denuded during the positive pulse, with measured values down by a factor of 5 of the comparable unipolar afterglow case.

5.4.2 Temporal Evolution of Ar and W Optical Emission Lines

Figure 5.12 shows OES data taken at the same positions above the racetrack as measured by TS, co-plotted with the comparable unipolar discharges. The data is separated into two subplots, indicating whether the measurement positions were inside or outside of the magnetic trap (see figure 4.2 for the location of the last closed flux surface). Similar to the centre-line results, at all measured positions above the racetrack, argon and tungsten lines are visible all the way through the duration of the positive pulse (labelled "Bipolar" in the plot). At all positions, the relative W optical emission decreases through the positive pulse, as was found in the the centre-line study, implying there was a decaying source of W in the discharge. Ar line emissions on the other hand show elevated intensities throughout the pulse. The relative intensities approximately follow the same trends as the measured T_e, with an increase in intensity coinciding with the measured increase in temperature. For the unipolar case, the intensities of Ar and W are undetectable soon after the negative pulse termination. This gave further indication that there is a region of hot plasma far away from the target, above the racetrack and the possibility of W re-sputtering from the walls.

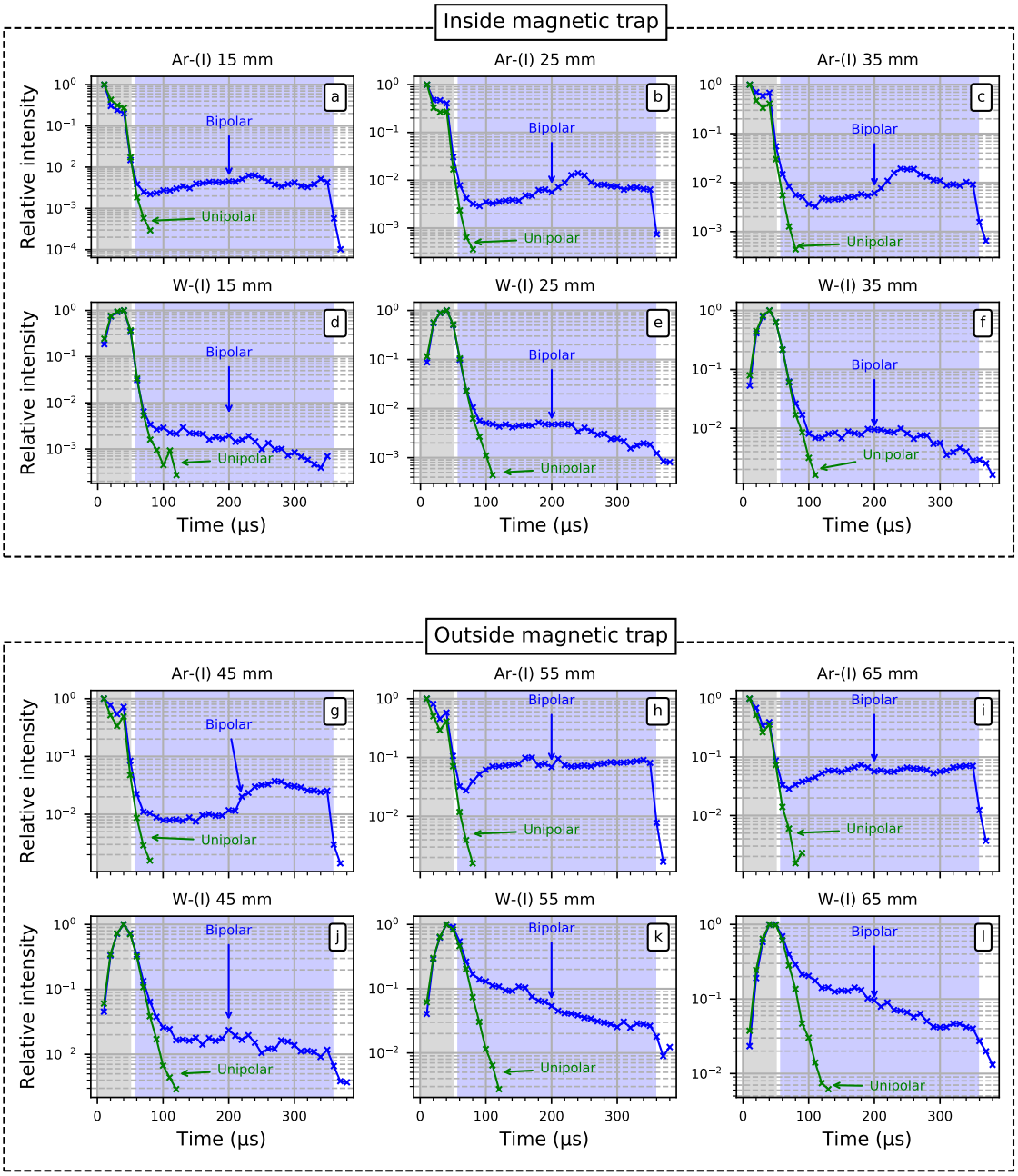

Figure 5.12: Comparison of OES (Ar and W) data, with the comparable unipolar HiPIMS case. The figure is split into two subplots indicating whether the measurement position was located inside or outside the magnetic trap.

5.5 Discussion

With application of a positive pulse in the discharge afterglow, TS measurements at two positions along the centre-line revealed a distinct transient rise and decay in electron temperature. The rise is seen to be delayed relative to the initiation of the positive pulse. The maximum acquired electron temperatures are more pronounced for longer positive pulse lengths and the delay in electron heating is shortened with increasing magnitude of positive pulse voltage. A two-fold increase in the gas pressure has only a marginal effect on the degree and timing of the electron heating phenomenon. The plasma to which the positive pulse is applied is essentially a decaying afterglow, as shown in all cases by the falling electron densities much the same as in the normal "off-time" (after glow) of unipolar HiPIMS operation.

Measurements above the racetrack, showed that the application of a 200 - 300 V positive pulse, led to a rise in electron temperature above the racetrack; similar to what is seen along the centre-line. Close to the target however, this rise is only modest. At successive distances above the racetrack position, the measured T_e rose to higher values and deviated sooner from the comparable unipolar case. The density of electrons within the magnetic trap during this heating period drops significantly compared to the unipolar (falling up to a factor 5). No such depletion in n_e is observed on the centre-line of the system. Clearly a region of hot plasma above the racetrack that is spatially inhomogeneous was present.

From other studies (see for example [89,132] and results presented in the next chapter) it was found that in the positive pulse phase, the plasma potential is raised rapidly above target, with comparable values to the applied V_{pp} magnitude. The bulk plasma then necessarily sits at a high potential relative to the grounded vessel walls, making the walls an effective cathode. Plasma ions will be accelerated across the wall sheaths (up to 300 V in this study) to both sputter the walls and liberate secondary electrons. For 300 eV argon ions, the sputter yield of tungsten is in the range 0.3 to 0.43 [207].This is relatively low compared to typical on-time rates, but given the high plasma density, it is expected that significant amounts of W will be sputtered from the grounded chamber walls.

The hot secondary electrons injected into the bulk decaying plasma will excite the gas and metal present. The subsequent release of a photon through deexcitation was captured in the optical emission study for both argon and tungsten. It was found that a measurable concentration of tungsten in the discharge during this "reverse" phase was present, as residual low energy target liberated tungsten left over from its creation in the on-time is

excited. It is also speculated that for high V_{pp}, excitation of re-sputtered tungsten from the walls may be adding to the intensity of the emission. The W (I) emission signal however decays, presumably due to the continuous reduction in the number of argon ions available to sputter the walls and the continuous loss of long lived, on-time tungsten, as the whole bulk plasma decays. At termination of the positive pulse, the W (I) line and Ar (I) intensity drops very rapidly, as the wall sheath potential and any W re-sputtering collapses. For the unipolar discharges, the W intensity is quickly undetectable after the negative pulse termination, in the afterglow.

The observed transient electron heating during positive pulses (for amplitudes greater or equal to 200 V) may be explained in terms of the creation of secondary emitted electrons at the wall. These electrons will be accelerated across the wall sheath, losing energy through inelastic collisions with bulk plasma species and thermalising to form an effectively hot group with a distribution of energies indistinguishable from a Maxwellian. A schematic of this scenario for $V_{pp} = 300$ V is shown in figure 5.13, where the bulk plasma potential is assumed to be 300 V and the chamber walls (as well as a substrate) are grounded. The figure also shows the re-sputtering of tungsten from the vessel walls.

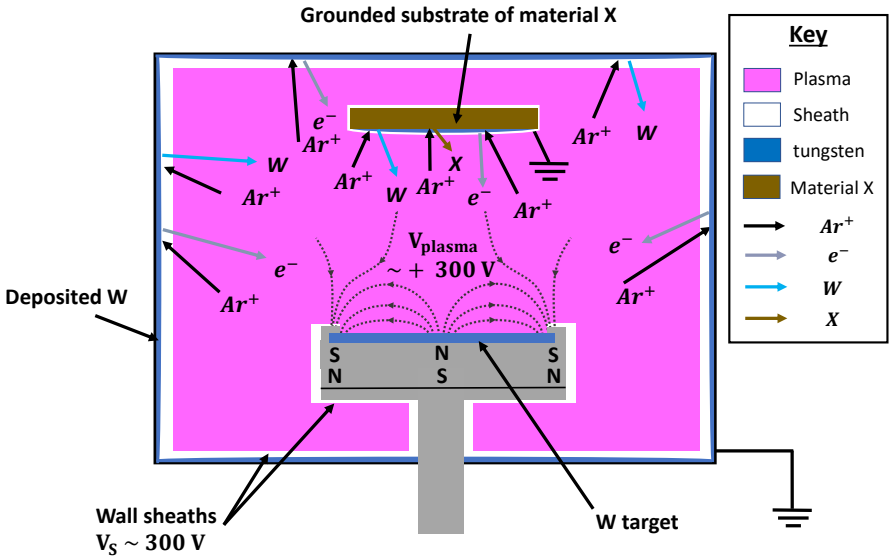

Figure 5.13: A schematic of a sputtering system where V_p is elevated to $\sim V_{pp}$ during the positive pulse. Shown here is the case of $V_{pp} = 300$ V with a grounded chamber substrate. The species involved are labelled in the key.

The slowing down and thermalisation (equipartition) times for sheath accelerated secondary electrons in the bulk plasma can be calculated following an expression stated in Spitzer [208]. For example, assigning an effective energy of T_e = 300 eV to sheath accelerated secondary electrons (in the case described in figure 5.3), then on initiation of the positive pulse and entering the bulk plasma of electron density $\sim 10^{18}$ m^{-3} and temperature $k_B T_e$ /e of $\sim$ 1 eV, these electrons will have a slowing down time $\tau_s \sim 70$ μs and equipartition time $\tau_{eq} \sim 100$ μs. From figures 5.2, 5.3 and 5.11, it is seen that given sufficient duration of the positive pulsing period and for $V_{pp} \geq 200$ V, a distinct peak in T_e is observed during the positive voltage period. It is difficult to know exactly why the temperature peaked, however, the energy flux of secondary electrons acting as a source of heating in the bulk is reduced during the afterglow. With a decaying source of energy this may have lead to a peak in electron temperature.

Wall-sheath accelerated secondary electrons generated in the positive pulse may not necessarily acquire the background bulk electron temperature but heat the plasma locally to form a hot group as observed in the LTS measurements. These electrons must necessarily cross open magnetic field lines of the relatively weak field downstream of the target to reach the measurement point, undergoing collisions with neutral gas, taking a finite time to do so. This time can be estimated by simple consideration of the classical cross–field diffusion coefficient of particles across B fields, given by:

$$D = \frac{k_B T_e}{m_e \nu (1 + \omega_c^2 \tau^2)}, \tag{5.1}$$

where τ is the average collision time (inverse of the momentum stopping collision frequency υ, calculated using the cross-section for collisions and electron thermal speed[3]), ω_c is the gyro radius given by $\frac{qB}{m}$. In the limit $(\omega_c \tau)^2 \gg 1$ (valid in this study), this expression reduces to:

$$D = \frac{k_B T_e \nu}{m_e \omega_c^2}. \tag{5.2}$$

The time for electrons to traverse distance L across the field can be stated as $\tau_D = \frac{L^2}{D}$. Assume a heated population of $\frac{k_B T_e}{e}$ = 3 eV (approximately equal to the maximum temperature measured in figure 5.3 in the positive pulse afterglow), a magnetic field strength of

[3] $\upsilon = n\sigma V_{th}$ where, n is the density of the neutral gas, σ is the cross section of electron and argon atom collision = 4.96 x $10^{-20} m^2$ for 3 eV electrons [209] and V_{th} is the thermal speed = $\sqrt{(\frac{k_B T_e}{m_e})}$

B = 10 mT and L = 5 cm, taken from the magnetron field topology, τ_D is estimated to be ~ 1000 μs. This is somewhat longer than the delay times measured. The exact mechanism for electron diffusion in the positive pulse period is unknown, however, assuming similar rates to those found during the on-time in other magnetron experiments [210, 211], namely Bohm diffusion, the diffusion coefficient can take the form:

$$D = \frac{1}{16}\frac{k_B T_e}{eB}, \tag{5.3}$$

then the corresponding time to reach the measurement position is ~ 130 μs. Therefore combining the thermalisation and cross field diffusion times may explain the delay in measured heating effect after initiation of the positive pulse.

The results in this chapter show that increasing V_{pp} reduces the delay time in the observed rise in T_e. From figure 5.3, the $V_{pp} = 300$ V positive pulse gives a delay time of ~ 140 μs (from positive pulse initiation) but for $V_{pp} = 200$ V it is ~ 260 μs. At $V_{pp} = 100$ V it is longer than the positive pulse duration itself (see chapter 6). Fast electron slowing down and equipartition times increase with increasing electron energy [208], however, the diffusion times for electrons across the B-field decrease. It seems from the measured trends (see figure 5.3), that the delay in local electron heating is more strongly governed by diffusion. This may explain the situation measured above the racetrack, where at further away positions, the temperature rise occurs sooner than positions closer to the target. The magnetic field above the racetrack quickly reduces at increasing distance (see figure 4.2), and hence the field electrons must transverse to the measurement position is less and would therefore result in quicker diffusion.

The fact that argon emission intensity increases and follows the electron temperature profile in the positive pulse indicates, that the hot electrons are exciting the neutral argon. The increased argon emission could be evidence of another discharge ignition, where now the target is positively biased, and the grounded walls act as an effective cathode. Hippler et al [124, 125] and Kozák et al [108], have also seen such a reappearance of background gas optical emission in the positive pulse and they too allude to the possibility of a reverse discharge where the electrons are returned to the cathode, gaining energy from the difference in potential between positive target and the local plasma. The presence of W line emission in the positive pulse, suggested to be wall re-sputtered material, entering the discharge may lead to some unwanted contamination of the plasma.

5.6 Conclusion

The temporal-evolution of electron temperature T_e, electron density n_e and argon and tungsten emission has been measured in bipolar HiPIMS discharges using incoherent laser Thomson scattering and optical emission spectroscopy. The results showed significant, but transient, electron heating takes place in the afterglow when a positive pulse of magnitude greater or equal to 200 V is applied, both on the centre-line and above the racetrack. Rises in T_e are delayed with respect to the initiation of the positive pulse and decrease with positive voltage. The rise in electron temperature was not observed for positive pulse lengths of 150 μs, at $V_{pp} = 100$ V and 200 V, however the $V_{pp} = 200$ V showed heating when an increased positive pulse length of $t_{pp} = 300$ μs was used. The delays were explained by considering the time taken for diffusion of hot secondary electrons, released from the grounded vacuum vessel walls to diffuse to the measurement position. Thomson scattering provided high fidelity electron property measurements with negligible perturbation to the plasma itself, making it a reliable unambiguous diagnostic tool.

During the positive pulsing period of $V_{pp} = 300$ V and $t_{pp} = 300$ μs, centre-line TS measurements revealed similar electron heating trends, both close to, and far away from the positive target, both rising and peaking almost identically. Comparing electron density measurements for comparable unipolar and bipolar HiPIMS pulses shows that during the positive pulse, the electron density on the centre-line had undergone little perturbation, maintaining roughly the same densities as those found in the normal afterglow. Measurements above the racetrack however, showed an inhomogeneous spatial variation in both electron density and temperature. Electron density measured inside the magnetic trap during the positive afterglow, show large reductions (by a factor of 5) compared to the normal afterglow. T_e was found to rise earlier and peak higher at successive distances away from target. This indicated hot plasma was present, that was spatially inhomogeneous above the target.

OES measurements showed increased argon emission during the positive pulse, both above the racetrack and centre-line, in agreement with the proposed formation of hot plasma. Evidence of excited metal species in the positive pulse region which are not present in the normal afterglow, indicated the possibility of a new source of tungsten. This was suggested to be from re-sputtering of deposited tungsten from the chamber walls. Ar ions fall through the large sheath potential provided by the elevated V_p, energetically bombarding the walls, sputtering W and ejecting secondary electrons from the surface.

The observed effects in the positive pulse are understood in terms of the generation of a transient "reverse" discharge, in which secondary electrons generated at the grounded vessel walls due to ion bombardment heat the bulk electrons. Large wall sheath potentials may lead to re-sputtered tungsten entering the discharge. Such a contaminating effect may not be an ideal feature in bipolar HiPIMS operation.

Chapter 6

Plasma Potential and 2D Imaging Investigation[1]

6.1 Introduction

Following on from the work presented in the previous chapter, results of plasma potential measurements and 2D images are presented. Plasma potential measurements were performed with an emissive probe, operated in the floating point regime as described in section 2.4, allowed fast potential changes to be measured. 2D images were taken using a fast gated iCCD camera, allowing broad band optical output to be measured throughout the positive pulse, revealing the physical characteristics of the reverse discharge. This chapter is split up into two sections: (6.2), focuses on the conditions measured by TS and OES, with $t_{pp} \leq 300$ μs. (6.3) examines the effect of longer positive pulses with $t_{pp} \geq 1$ ms. The experimental arrangement has been described in detail in chapter 4. All discharges used for this chapter, unless stated other wise, were produced in 1.6 Pa of argon gas. The negative pulse had a duration of $t_{np} = 50$ μs and pulses had a repetition rate of 50 Hz.

It should be recognised that some of the results presented in this chapter have been published [2] and have been reproduced for this thesis.

[1] Some of the research presented in this chapter has been published in a peer-reviewed journal article [2] and have been reproduced for this thesis.

6.2 Short Positive Pulse Results

This section is concerned with positive pulses of length t_{pp} = 300 μs, corresponding to the discharges diagnosed in chapter 5 by LTS and OES.

6.2.1 Plasma Potential Measurements

Figure 6.1 shows the measured plasma potential, (V_p) during the positive pulse of duration, t_{pp} = 300 μs, for V_{pp} = 100, 200, and 300 V. The waveforms of the discharges are shown in figure 5.1. The emissive probe was centred inside the chamber and the magnetron had a height of z = 61 mm - the same location (r = 0 mm, z = 61 mm) as TS measurements presented previously. Evident from this plot is the fast rise of V_p, closely following the target potential (V_t) for all positive pulse magnitudes. The measured plasma potential exceeds the target potential by several volts during the early stages of the positive pulse. Interestingly, V_{pp} = 200, 300 V shows a V_p drop during the positive pulse, with the V_{pp} = 300 V dipping $\sim$ 100 μs before V_{pp} = 200 V. After the dip in measured V_p, it rises again but stays below V_t. The V_{pp} = 100 V shows no dip in V_p. It is clear from figure 6.1 that the plasma potential at this position has been significantly raised, to values corresponding to the applied V_{pp}. If a grounded substrate was placed at this position, ions would bombard the surface, accelerated through the large potential difference, equivalent to V_p.

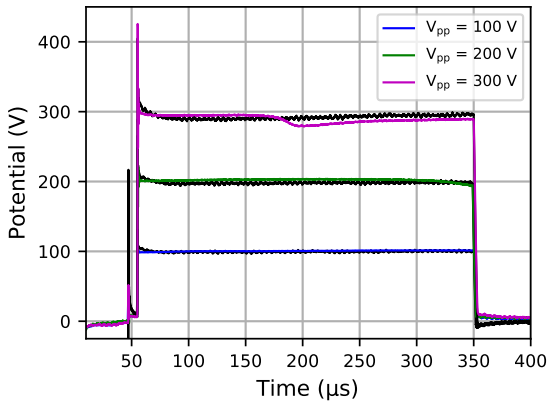

Figure 6.1: Plots of V_p versus time at position r = 0 mm, z = 61 mm, during the positive pulse of duration, t_{pp} = 300 μs, for V_{pp} = 100, 200, and 300 V. The current and voltage waveforms are shown in figure 5.1. The target potential is co-plotted (black lines) for each V_{pp}.

Given that measurements of the temporal V_p, T_e and n_e have been performed at this position, the bombarding ion flux and ion energy flux densities to a grounded substrate, placed at this position in the chamber, throughout the pulsing period can be calculated through equations 6.1 and 6.2, respectively:

$$\Gamma_i = 0.61 n_e \left(\frac{k_B T_e}{M_i} \right)^{\frac{1}{2}}, \tag{6.1}$$

$$Q_i = 0.61 n_e \left(\frac{k_B T_e}{M_i} \right)^{\frac{1}{2}} E_i, \tag{6.2}$$

$$\underbrace{E_i \sim k_B T_e}_{negative\ pulse} \qquad \underbrace{E_i = eV_p}_{positive\ pulse}$$

where n_e, T_e is the electron density and temperature found from TS, M_i is the ion mass, $(\frac{k_B T_e}{M_i})^{\frac{1}{2}}$ is the Bohm velocity and E_i is the ion energy. The additional factor of 0.61 arises due to the potential drop in the pre-sheath [4, p. 275]. To accelerate ions to the Bohm velocity requires a potential drop of $\mid \phi_s \mid \geq \frac{1}{2} k_B T_e$ over the pre-sheath. For a Maxwellian plasma, this gives the density of ions at the sheath edge as $n_s = n_i e^{(\phi_s / k_B T_e)}$ $= n_i e^{(1/2)} = 0.61 n_i$ ($n_i \approx n_e$ through quasineutrality).

Figure 6.2 shows the results of these calculations with respect to a centred grounded substrate, placed at r = 0 mm, z = 61 mm, inside the vacuum chamber throughout the pulsing period. The discharge waveforms were the same as shown in figure 5.1, with t_{np} = 50 μs (grey region), and t_{pp} = 300 μs (blue region) for V_{pp} = 0, 100, 200, and 300 V. In these calculations, M_i was allocated to be that of Ar, as the concentrations of ions was unknown throughout the pulse. As expected from equation 6.1, there is little change in the ion flux density to the substrate (figure 6.1(a)) between all V_{pp} values. V_{pp} = 300 V shows the largest change due to the elevated electron temperature during the positive pulse. A small increase is found at the end of the V_{pp} = 200 V. However figure 6.1(b) shows a significant increase in the ion energy flux to the substrate. During the negative pulse, the ion energy (E_i) was assumed to be $\sim k_B T_e$.

During the positive pulse, E_i will be equivalent to the drop in sheath potential from the bulk plasma to the grounded substrate ($E_i = eV_p - V_{ground} \approx eV_p$). For V_{pp} = 100, 200 and 300 V, during the positive pulse, a large increase (up to 3 orders of magnitude) in the energy flux to the grounded substrate is obtained, compared to the unipolar V_{pp} = 0 V case. As expected, with increasing V_{pp}, the flux is greater.

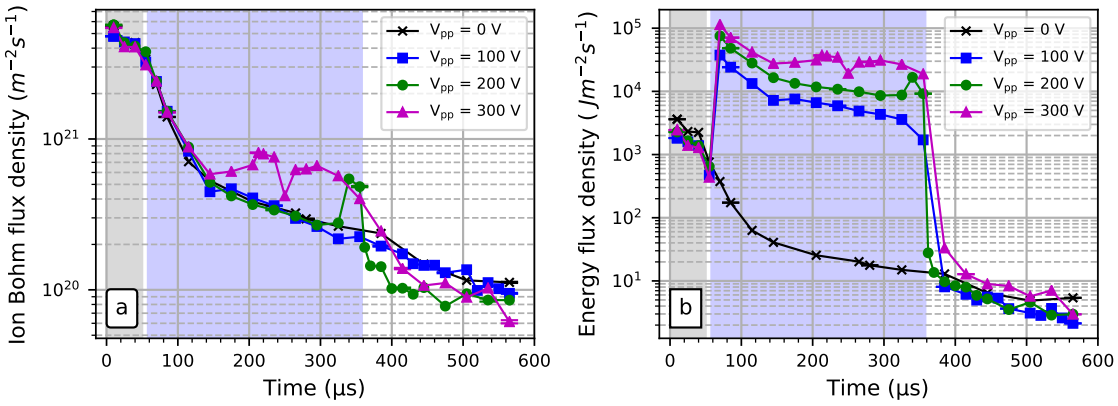

Figure 6.2: Plots of (a) Ion Bohm flux density and (b) Energy flux density versus time at position r = 0 mm, z = 61 mm, for a positive pulse of duration, t_{pp} = 300 μs, for V_{pp} = 0, 100, 200, and 300 V. This figure was created using TS data from figure 5.3 and V_p data from figure 6.1.

Since a growing substrate will receive ion fluxes through the entire bipolar HiPIMS waveform, over many successive pulses, it is informative to calculate the time-averaged values of Γ_i and Q_i. These are shown in table 6.1 and were time-averaged over time periods t = 0 to t = 358 μs, thus averaging over the entire duration of the negative and positive pulse. It is clear that the time-averaged bombarding flux density, $\langle\Gamma_i\rangle$ is only marginally increased for increasing V_{pp}. The time-averaged energy flux density however, is greatly increased, with V_{pp} = 300 V showing an $\sim$ x 85 greater flux than the comparable V_{pp} = 0 V case. Clearly, the inclusion of a positive pulse in HiPIMS operation would have significant effects on thin film production, enhancing the film growth. For example, Avino et al [212] reported an improved densification in their films, with the inclusion of a positive pulse.

$\mathbf{V_{pp}}$ **(V)**	$\langle\Gamma_i\rangle$ **(m^{-2} s^{-1})**	$\langle\mathbf{Q}_i\rangle$ **(Wm^{-2})**
0	1.04 $\times 10^{21}$	3.4 $\times 10^{2}$
100	1.05 $\times 10^{21}$	7.3 $\times 10^{3}$
200	1.12 $\times 10^{21}$	1.6 $\times 10^{4}$
300	1.20 $\times 10^{21}$	2.9 $\times 10^{4}$

Table 6.1: The calculated time-averaged values of $\langle\Gamma_i\rangle$ and $\langle Q_i\rangle$ for the cases shown in figure 6.2.

Figure 6.3 shows the results of an emissive probe scan, tracking the plasma potential along the centre-line (a), r = 0 mm and, above the racetrack (b), r = 48 mm at regular intervals. The measurements were taken from 15 mm from the target surface and extended to a 65 mm distance in steps of 10 mm, during a bipolar HiPIMS discharge with a 300 μs, 300 V positive pulse (see figure 5.1 for the waveform). It should be reiterated here that the probe had a fixed position, and the magnetron was moved vertically in the chamber relative to the fixed probe.

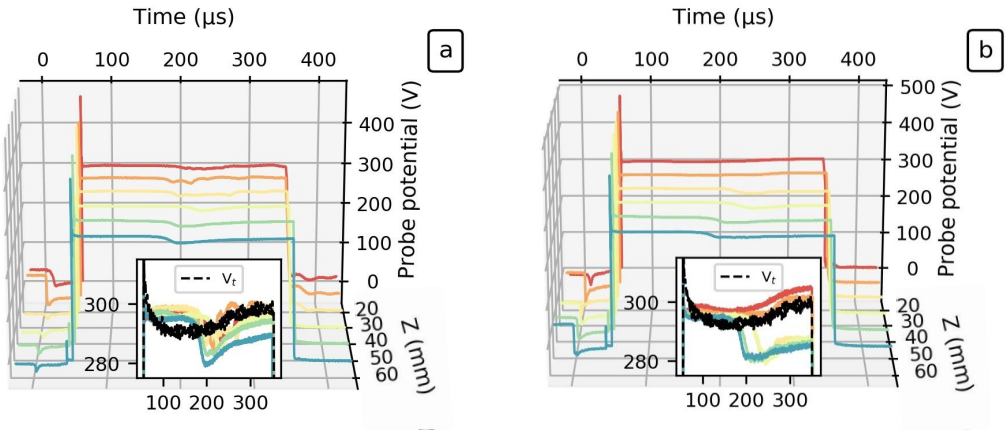

Figure 6.3: A plot of the temporal evolution of the the plasma potential profile throughout a V_{pp} = 300 μs, 300 V bipolar HiPIMS discharge ignited at 1.6 Pa of argon gas at several distances from the target. The target potential V_t is also plotted for comparison. (a) the centre-line and (b) the racetrack

Plasma potential measurements of the racetrack during the on-time are inherently difficult due to the transient particle dynamics, high magnetic field and large proportions of energetic electrons. It was found that close to the target; the measured probe voltage failed to lock to a fixed potential and instead was heavily influenced by the heating cycle of the probe. The values shown in figure 6.3 are therefore not representative of the true potential during this time period and caution should be made when interpreting the on-time values. However, during the positive pulse, the probe operated as expected as detailed in section 4.3.3. Since this thesis was focused on positive pulse dynamics, no further inquiries were made into the plasma potential behaviour inside the racetrack during the on-time and is omitted from the following discussion.

Each plot has an insert magnifying the time period of the positive pulse with target potential plotted in black. During the early stages of the positive pulse, the plasma potential

rises sharply at all positions, taking < 1 μs to reach the target potential. Soon after, the measured plasma potential at each position exceeds the target potential by several volts. Interestingly, the potential dip during the positive pulse, as found in figure 6.1, is present at all positions on the centre-line (see subplot in figure 6.3(a)), with the furthest away position showing the greatest dip. This is not the case above the racetrack (see subplot in figure 6.3(b)) as for positions close to the target, no V_p dip is found. As will be shown in the following sections, this indicated that restructuring of the plasma occurred during the positive pulse delivery.

As aforementioned, in some studies a distinct moving potential gradient, analogous to a double layer, has been reported during the positive pulse, extending outward from the target surface into the bulk plasma. To examine whether such structures were present in the system used in this work, a contour plot of the early stages of the positive pulse (where one would expect a double layer to form if present) is presented in figure 6.4. Shown here is the case for $V_{pp} = 300$ V and was created using data from figure 6.3. It is clear from these plots that the plasma potential rises almost uniformly across all the measured positions with little to no delay at each position, indicating no significant structure is present along the measured positions. The large values of > 400 V seen in the plots are where V_p follows the target voltage overshoot and the initial voltage ripple at the initiation of the positive pulse.

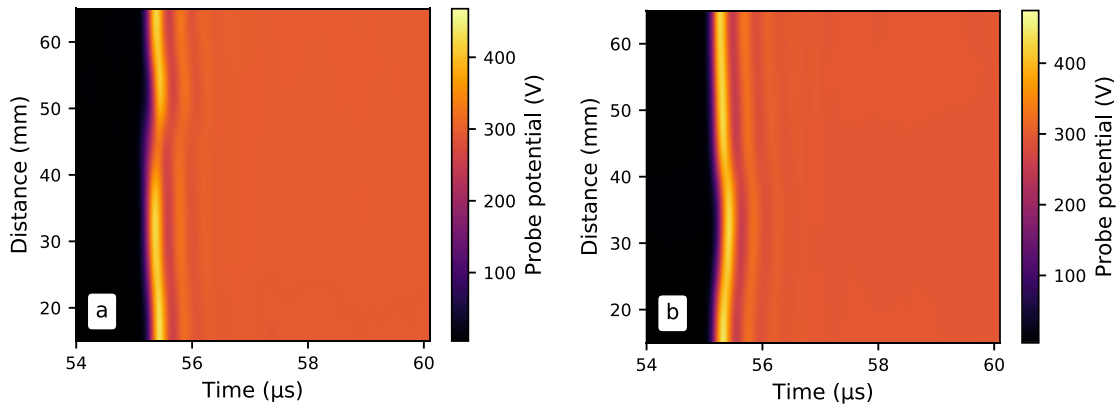

Figure 6.4: Contour plots of the early stages of the positive pulse, showing the measured V_p magnitude. (a) the centre-line and (b) the racetrack

6.2.2 2D Imaging

It has been suggested in [108, 124, 125, 133] that during the positive pulse of a BP-HiPIMS plasma, a reverse discharge ignites. This section presents direct evidence of this phenomenon, observed using time-resolved broad band 2D optical imaging. To compare data taken at different temporal periods, images were normalised to the maximum intensity found within the set of images taken. This was done in post processing of the data, using a Python script that loaded all the iCCD data arrays taken during that particular temporal scan, and found the maximum pixel count (intensity). Each pixel is then normalised to this maximum. This is similar to the analysis procedure performed for OES measurements (see section 4.2.7) and as the same conditions were used for each scan, resulted in relative intensity images. Images obtained at different times throughout the discharge are readily comparable to each other; sharing a common intensity scale. As with the OES procedure, acquisition time was kept to a minimum to minimise the transmission loss due to sputtering and the need to change the soda glass.

Figure 6.5 shows broad band images taken during the positive pulse of length $t_{pp} = 300$ μs, during the bipolar HiPIMS discharges (waveforms shown in figure 5.1). The left hand set of images shows $V_{pp} = 200$ V and the right hand side shows $V_{pp} = 300$ V. The images taken are in the range t = 180 μs to t = 380 μs. In general, a clear structure develops during the positive pulse. This provided direct evidence of the ignition of a secondary discharge, with timings directly corresponding to the onset of electron heating measured by TS presented previously. As the reverse discharge develops it takes the shape of a dewdrop anchored on the target centre. Note, the target is now acting as an anode. This discharge is squeezed to the centre-line by the lobes of the trap magnetic field. Early images during the positive pulse (t $\leq$ 180 μs), not shown, reveal a homogeneous dark chamber with relatively low optical output. The images shown have a striking resemblance to the fireballs imaged by Chauhan et al [126] (shown in figure 2.10) in their DC magnetron system.

Similar to the TS results, where the measured electron heating for the $V_{pp} = 200$ V (figure (5.3) occurred ~ 100 μs after the $V_{pp} = 300$ V comparable case, 2D imaging clearly shows the same delay in ignition. Once ignition occurred, the intensity and shape of the discharge is not uniform. Taking the case of $V_{pp} = 300$ V, it is clear that the discharge evolved through time, increasing its visual expanse in the z direction. Furthermore, the intensity of the images are not uniform throughout the positive pulse, with intensity di-

minishing towards the end of the pulse, mirroring the evolution of T_e measured by TS. It should be highlighted again that the images are accumulated over 100 plasma pulses with an exposure time of 2 μs and thus presents the combined intensity from the summed pixel count.

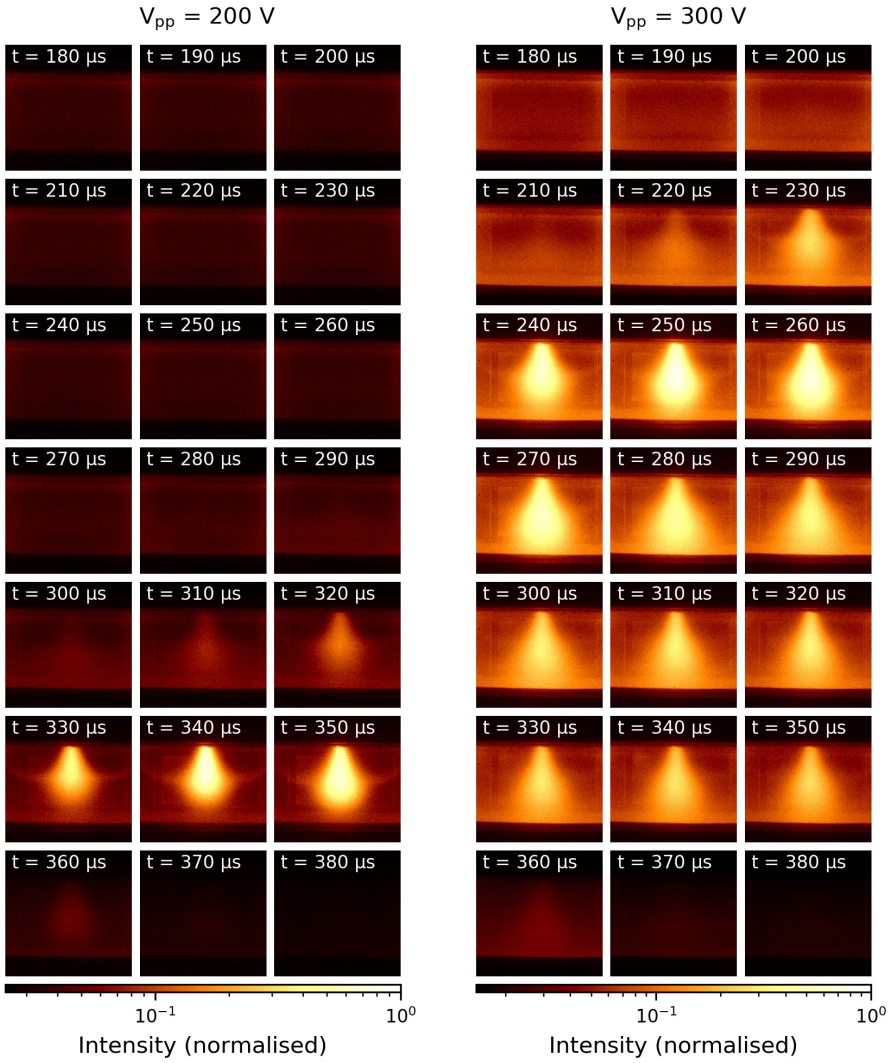

Figure 6.5: Broad band iCCD images taken during the positive pulse (t_{pp} = 300 μs) of a bipolar discharge of (left) V_{pp} = 200 V and (right) V_{pp} = 300 V for time periods t = 180 μs to t = 380 μs. The magnetron is mounted vertically, facing downward.

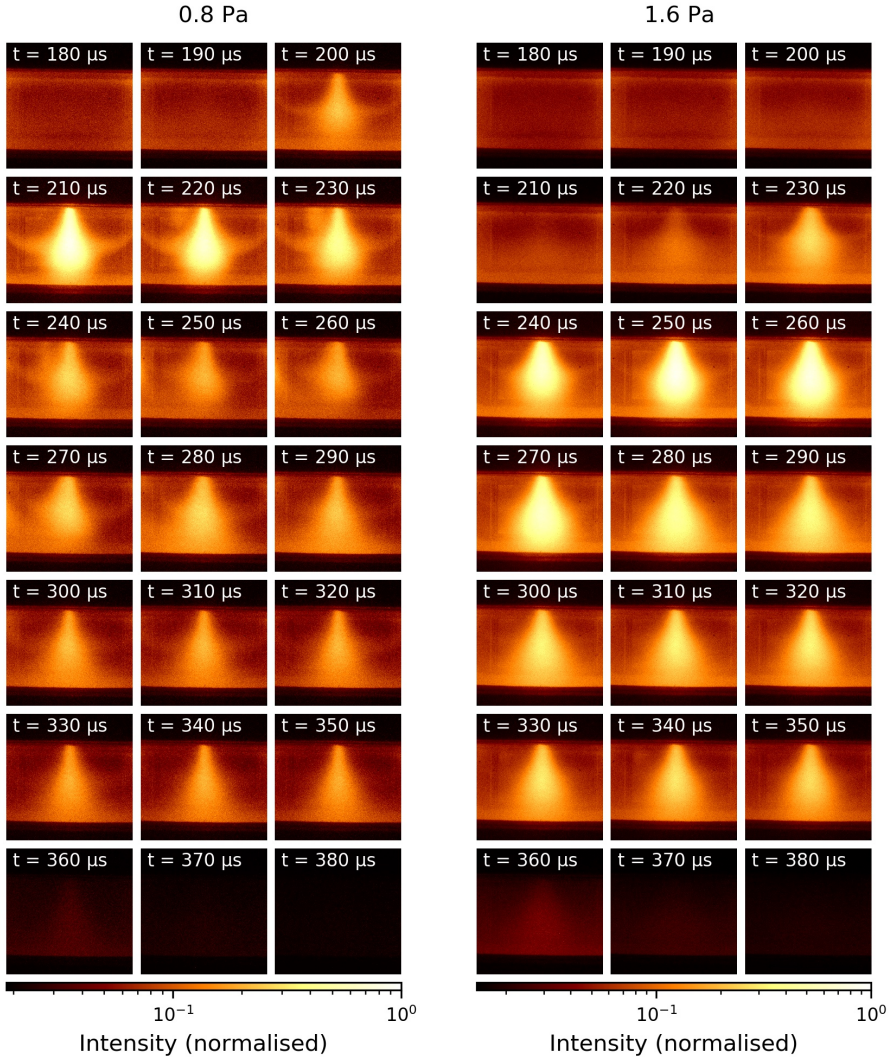

Figure 6.6: Broad band iCCD images taken during the positive pulse of a bipolar discharge (t_{pp} = 300 μs, V_{pp} = 300 V) of (left) P = 0.8 Pa and (right) P = 1.6 Pa for time periods t = 180 μs to t = 380 μs.

Figure 6.6 shows comparative braodband imaging bipolar pulses of t_{pp} = 300 μs, V_{pp} = 300 V, ignited at 0.8 Pa (left) and 1.6 Pa (right). These have identical conditions to those measured by TS in figure 5.4 (c,d). Immediately obvious is the earlier ignition for the 0.8 Pa case, igniting $\sim$ 20 μs before the discharge with 1.6 Pa backing gas. This is inline with the rise in electron temperature measured by TS. Most notably, between the

two discharge conditions, is the difference in relative intensities. Both discharges have an initial peak in brightness before an intensity drop during the positive pulse, however the 0.8 Pa discharge has significant light emission decay compared to the 1.6 Pa. This was also reflected in the electron temperature measurements as shown in figure 5.4. For the lower pressure case, the T_e decayed much faster in the positive pulse than the higher pressure case. This strongly linked rising electron temperatures to the ignition and evolution of the secondary reverse discharge.

6.2.3 Image Relation to TS and Plasma Potential

The results presented in this section analyses some of the iCCD images presented previously, linking the temporal evolution of the discharge to the measured T_e, n_e and V_p. Figure 6.7 shows iCCD images taken during the positive pulse for a V_{pp} = 300 V (shown also in figure 6.5). In the images the magnetic field direction (shape) and the positions at which the LTS measurements were made are marked with black arrows and blue crosses respectively. Figure 6.7 (a) shows an image taken in the relatively early stages of the ig-

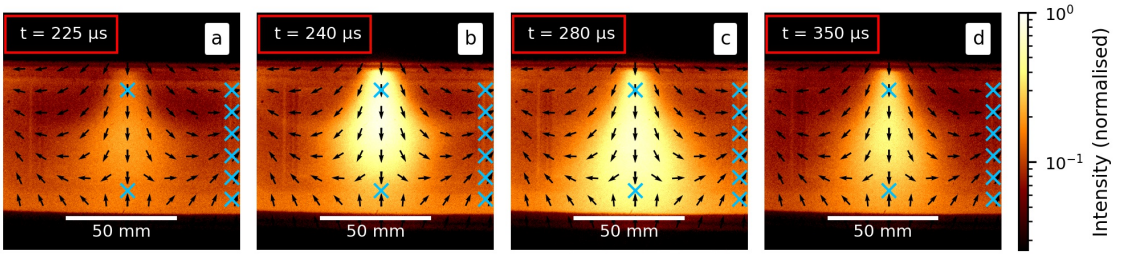

Figure 6.7: iCCD images taken during the positive pulse of a bipolar discharge of V_{pp} = 300 V at a) 225 μs, b) 240 μs, c) 280 μs and d) 350 μs) after the initiation of the negative pulse. The magnetron is mounted vertically, facing downward. The magnetron anode ring protrudes $\sim$ 7 mm from the target surface.

nition of this secondary discharge (t = 225 μs), where a bright central region began to be illuminated. A relatively dark region also appeared in the magnetic trap, as the electron density in this region has been depleted (see figure 5.10). Figure 6.7 (b) shows the brightest observed broad band emission during the reverse discharge, taken at t = 240 μs. Evident in this image are the glowing wings, extending from the central column of light emission, with analogous shape to the magnetron B-field. This bright region is due to magnetised electrons which follow the field lines as they are attracted to the now positive target, stim-

ulating emission via collisions with the background gas. Figure 6.7 (c) shows time step t = 280 μs, where the plasma extends further downstream in the z direction, illuminating more of the chamber and giving the reverse discharge a more triangular shape. Figure 6.7 (d) shows a time period just before the positive pulse termination (t = 350 μs), where the electron temperature measured by LTS has dropped from its initial peak. This is apparent in the image, as the intensity of the glow has decreased and the plasma ceased its extension in the z direction. The discharge returns to the original dewdrop shape.

To investigate the difference in electron parameter behaviour between positions on the centre-line and above the racetrack, LTS measurements of T_e and n_e at 4 different locations are shown in figure 6.8. Presented here are two positions on the centre-line (r = 0) one close to the target at z = 15 mm, and the other downstream z = 61 mm (see figure 6.8 (a-d)). These results are also presented in chapter 5. The equivalent two positions above the racetrack (r = 48 mm) are inside the magnetic trap at z = 15 mm and outside the trap at z = 65 mm, figure 6.8 (e-h). Two discharge cases are considered, bipolar HiPIMS with V_{pp} = 300 V and the unipolar case V_{pp} = 0 V. In terms of electron heating, the main result is that during the positive pulse, electron heating can be seen at all positions on the centre-line (figure 6.8 (a) and (b)), however above the racetrack this phenomenon is seen outside the magnetic trap (figure 6.8 (f)). Close to the target inside the magnetic trap, little heating is observed (figure 6.8 (e)). On the centre-line the application of the positive pulse does not change the electron density n_e compared to the unipolar case (figure 6.8 (c) and (d)). However, above the racetrack n_e is significantly reduced (figure 6.8 (g) and (h)).

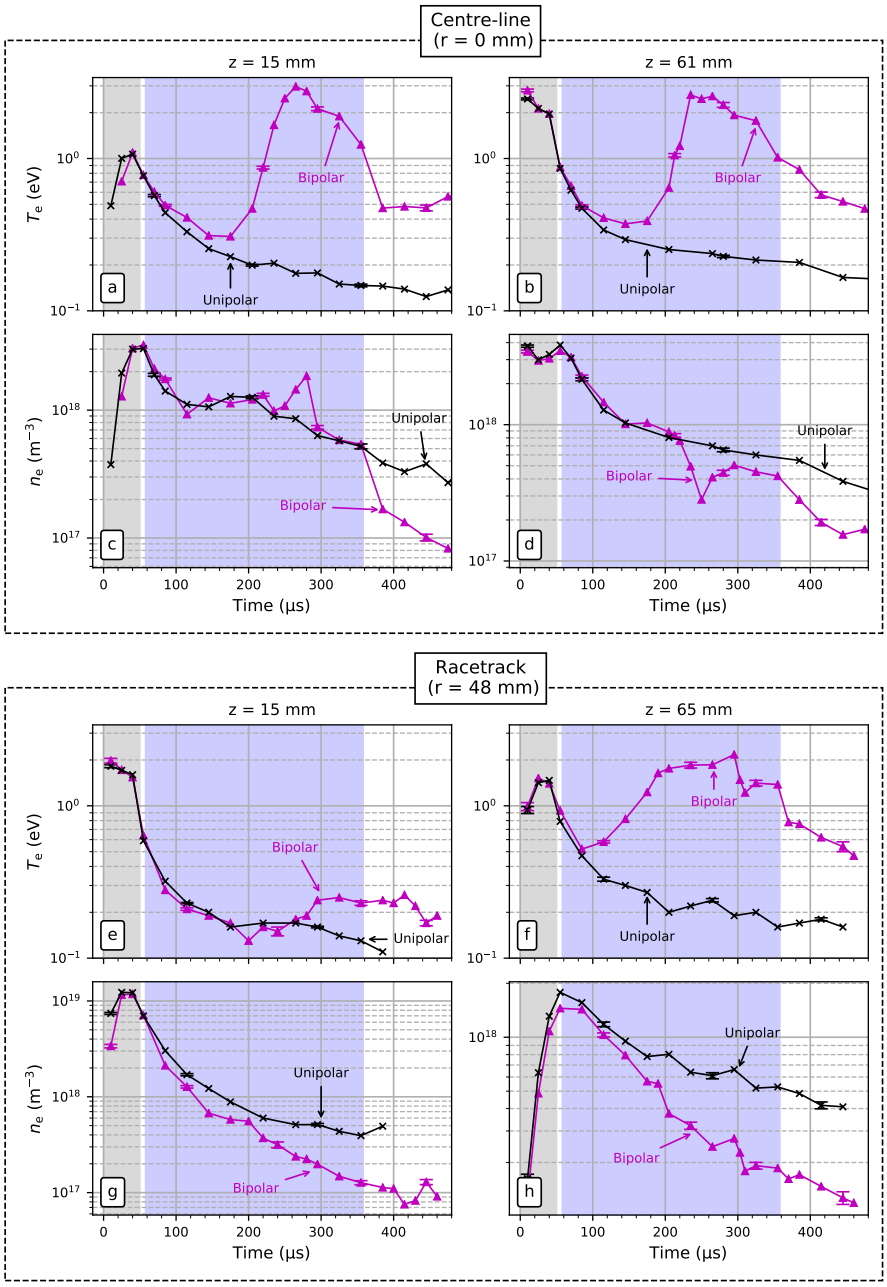

Figure 6.8: Plots of electron density n_e and electron temperature T_e versus time at comparable axial positions on the centre-line and above the race track groove, r = 48 mm, for V_{pp} = 300 V (triangle symbol) and the comparable unipolar (cross symbol) pulses. (a,c,e,g) z = 15 mm, (b,d,f,h) z = 61,65 mm.

Figure 6.9 shows the relation between V_p, T_e and image intensity for the conditions showed in figure 6.5 (V_{pp} = 300 V , t_{pp} = 300 μs). The measurement position of both the TS (T_e) and emissive probe (V_p) were on the centre-line (r = 0 mm) at a height of z = 61 mm, whereas the image intensity values are presented as an average of the entire image. This figure has two important features. Firstly, it is clear that the measured electron temperature is directly correlated with the image intensity as would to be expected. Secondly, the plasma potential dip, shown also in figure 6.1, appears to have a direct correlation with both T_e and image intensities. V_p at this location reaches it's minimum approximately at the same time the measured electron temperature rises. Soon there after, the reverse discharge was visible on the iCCD images.

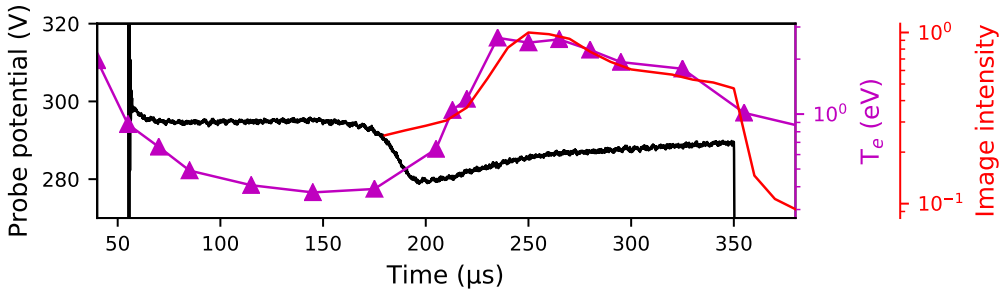

Figure 6.9: Co-plots of V_p, T_e made at r = 0 mm, z = 61 mm and average image intensity during the positive pulse of a bipolar HiPIMS discharge of V_{pp} = 300 V, t_{pp} = 300 μs.

Kozák et al [108] also measured a potential dip towards the end of their positive pulse (V_{pp} = 100 V and t_{pp} = 200 μs), 100 mm away from the target and simultaneous increase in excited Ar and Ti species (see figure 2.9). It should be noted that for the same measurement positions, but with V_{pp} = 200 V (discharges imaged in figure 6.5), the same trends were observed. This directly linked a change in local (centre-line) potential to the ignition of the reverse discharge, indicated by elevated electron temperatures and bright light emission.

As mentioned previously and shown in figure 6.3, plasma potential profiles during the duration of the positive pulse, both on the centre-line and above the racetrack, showed subtle differences in their temporal evolution. Most notably, was the difference in magnitude of the potential dip at increasing distances away from the target. To examine this further, V_p measurements were made at several radial and axial positions during the positive pulse for V_{pp} = 300 V, in an attempt to understand the temporal and spatial evolution of V_p. These are shown in figure 6.10.

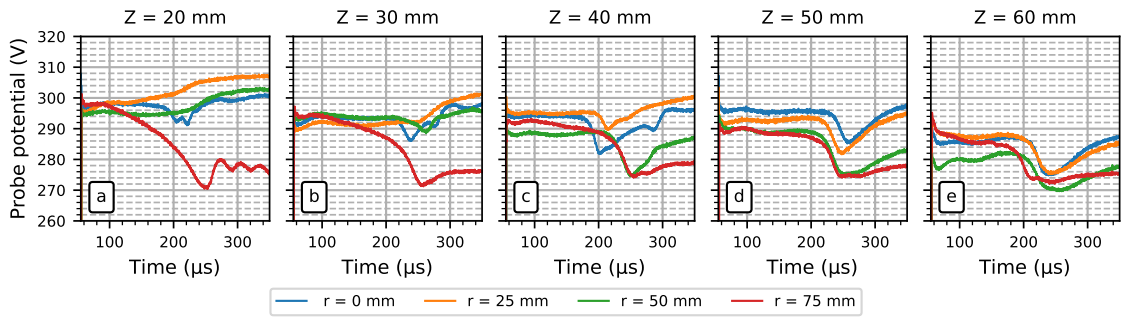

Figure 6.10: Plasma potential measurements made during the positive pulse of a bipolar HiPIMS discharge with of $V_{pp} = 300$ V, $t_{pp} = 300$ μs, for different axial and radial positions.

Scans were taken at 5 axial positions, at z = 20, 30, 40, 50, 60 mm (figure 6.10 a,b,c,d,e respectively) and 4 radial positions (r = 0, 20, 50, 75 mm). The scan encompassed the entire radius of the 150 mm diameter tungsten target and the predominant axial span of the reverse discharge as seen from iCCD images. Most notably, in all axial plots, the plasma potential reached it's lowest values furthest away from the centre-line. Also evident is the lower overall V_p measured at increasing distances from the target.

It is instructive to plot the data in figure 6.10 as time segmented 3D plots [2], to provide visual representation of the V_p structure throughout the positive pulse and reverse ignition evolution. This is shown in figure 6.11 for time periods of 200 - 340 μs, where the reverse discharge is visible on the iCCD. In order to produce the plots in figure 6.11, the radial measurements are mirrored on the centre-line to give a full representation of V_p over the target surface. This assumed radial symmetry of the discharge. The measured value of V_p at each position is plotted, with magnitude indicated by the colour bar. From these plots it is clear that an inhomogeneous V_p structure formed during the positive pulse, with lower potentials found further away from the target (z direction) and radially. A similar structure was also found by Zanáška et al [133] during phase C (see section 2.1.5.2) of their bipolar pulse, with double layer structure above the target. The high potential side inside the trap reached values close to the applied target voltage and outside the trap settled to values of V_{pp} - $\sim$ 40 V. Similar to the situation measured in this work, the measured potential structure lasted until the end of their positive pulse and expanded slightly throughout the pulse.

[2] Due to the lack of data points, a contour plot was deemed unsuitable

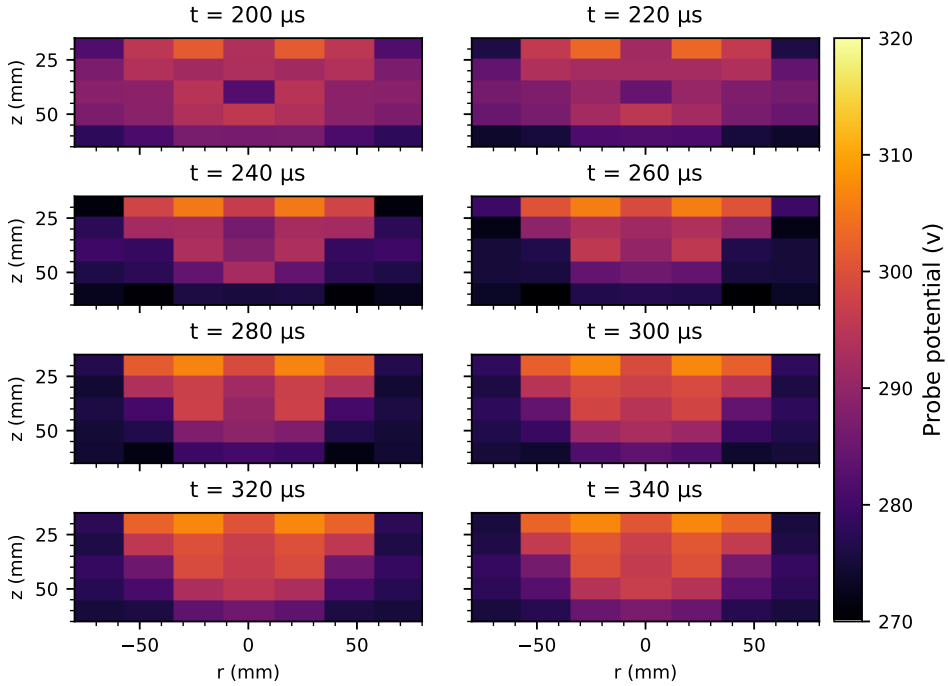

Figure 6.11: Plots of plasma potential measurements made during the positive pulse of V_{pp} = 300 V, t_{pp} = 300 μs. Data was taken from figure 6.10.

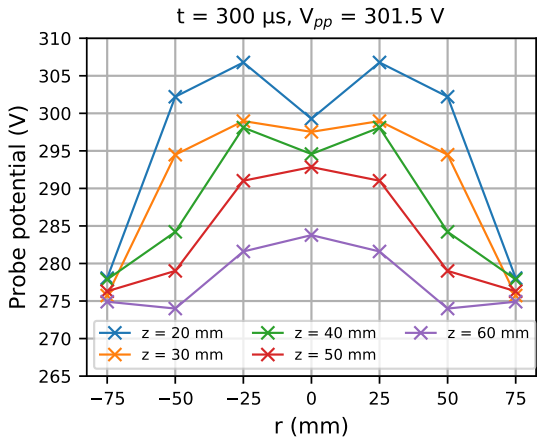

Figure 6.12: Radial V_p plots at different z positions at time t = 300 μs. For reference, the target potential during this time period is V_{pp} = 301.5 V.

The potential structure is further explored in figure 6.12. The V_p structure is presented for t = 300 μs, as a 2D plot with the radial coordinates on the x axis and the probe potential on the y axis. The separated z coordinate data is plotted and indicated by the legend. Radially, at each z position, there is a potential step, extending from the centre-line radially outward. The potential step from r = 0 mm to r = 75 mm ranges from $\sim$ 8 V to $\sim$ 25 V across the z axis. Axially, a similar potential step is also present, for example taking the line r = 0 mm, between z = 20 mm and z = 60 mm, a potential step of $\sim$ 16 V is found. The potential steps measured may give insight to the mechanisms responsible for maintaining the reverse discharge.

6.3 Long Positive Pulse Results

This section is concerned with positive pulses of length $t_{pp} \geq 1$ ms. The repetition rate and negative pulse length was fixed at 50 Hz and $t_{np} = 50$ μs. From the discharges diagnosed with $t_{pp} = 300$ μs there was an apparent relation between the reverse discharge ignition (found from T_e, V_p and optical imaging) and the magnitude of the positive pulse. However, the $V_{pp} = 100$ V showed no such ignition during the 300 μs positive pulse. The aim of this short study was to determine whether the reverse discharge would ignite, even at low V_{pp}, given a long enough positive pulsing period. Thomson scattering measurements of such long positive pulses were not possible, due to electron densities reaching values below the detection limit of the system during the positive afterglow period. Therefore, this section includes only iCCD images and V_p measurements.

6.3.1 2D Imaging

The imaging procedure was the same as described previously, however, the gain of the iCCD needed to be increased for the lower V_{pp} values compared to that used previously. This was a combination of transmission loss from the optical viewing port and the relatively dimmer emission. Figure 6.13 shows iCCD images taken during the positive pulse of a bipolar HiPIMS discharge ($t_{pp} \geq 1$ ms) for $V_{pp} = 100$ V (a) , 40 V (b) and 20 V (c). The figure shows the early stages of the reverse discharge evolution, showing the ignition and it's early temporal evolution. The gain of the camera was kept the same for each temporal scan, meaning that images in a set can be compared. However as aforementioned, no direct comparison between the different discharge conditions can be made, only trends in their

relative intensities can be inferred.

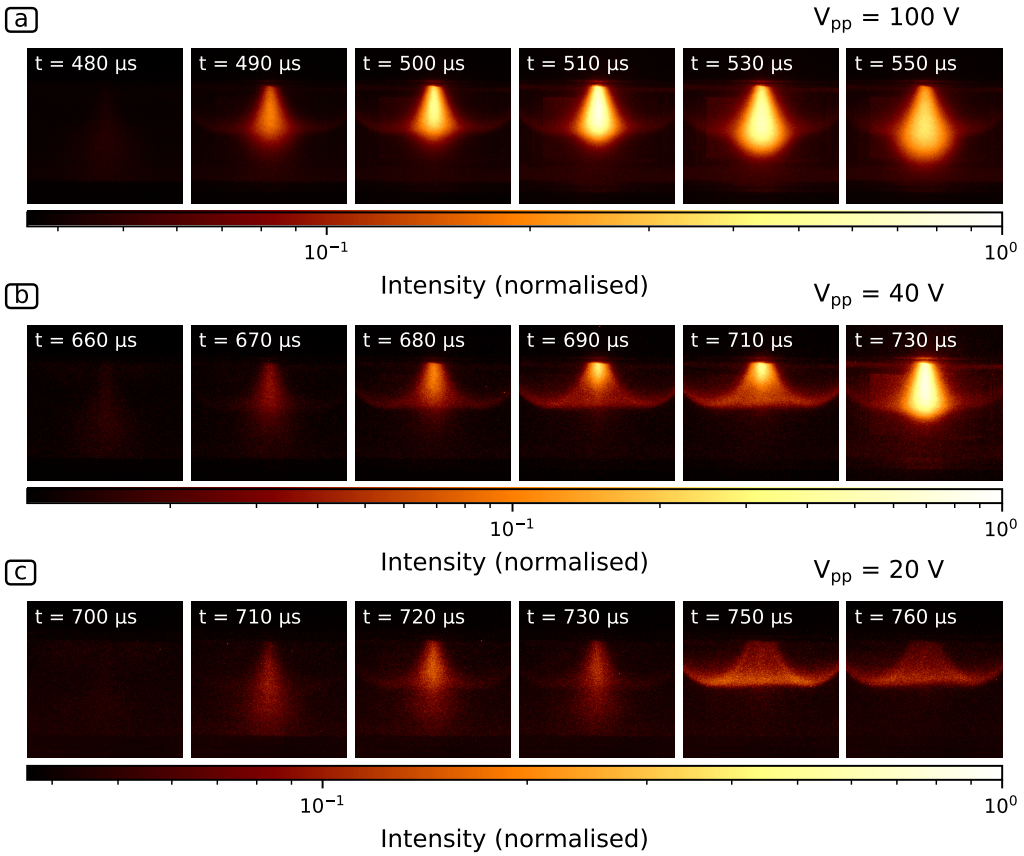

Figure 6.13: iCCD images taken during the positive pulse of bipolar discharges ($t_{pp} \geq 1$ ms), with V_{pp} = 100 V (a), 40 V (b) and 20 V (c), showing the early temporal evolution.

Interestingly, for the V_{pp} = 100 V case, an elongated positive pulse period did result in the formation of a reverse discharge, igniting at $\sim$ t = 490 μs. This was $\sim$ 180 μs longer than the V_{pp} = 200 V, and $\sim$ 270 μs after the V_{pp} = 300 V discharges. Furthermore, ignition is observed at V_{pp} = 40 and 20 V, but these occurred even later in time. The early evolution of the V_{pp} = 100 V is very similar to the 200, 300 V positive pulse cases, however, the evolution of the V_{pp} = 40 and 20 V show different structure. The V_{pp} = 100 V showed the familiar dew drop shape whereas, the V_{pp} = 40 and 20 V show little extension downstream from the target. Instead, the discharge is attached predominantly to the target centre-line and lobes of the magnetic trap. Figure 6.14 shows an image of

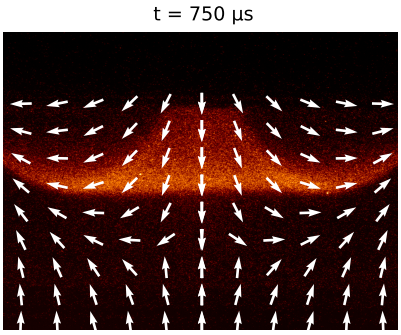

Figure 6.14: Figure 6.13 (c) at t = 750 μs, expanded with magnetic field vectors plotted.

V_{pp} = 20 V at t = 750 μs, with the magnetic field vectors overlaid. The discharge is shaped by the magnetic field, with illuminated wings following the field vectors. Glowing wings were also present in images of discharges with V_{pp} = 300, 200 and 100 V, however, the intense emission from the central column of the discharge dominated. Clearly, at low positive pulse magnitudes, the conditions during the positive afterglow, stunt the expanse of the central discharge.

6.3.2 Ignition

It was found that a local change in V_p was an indication of secondary discharge ignition. As was shown in figure 6.9, the measured V_p, above the centre-line initially sits at a slightly higher potential than that of the target, before reducing to a minimum value. The potential dip occurred simultaneously to the measured increase in T_e and increased light emission, captured on the iCCD. Therefore measurements of V_p (or V_f) would provide a quick indication of when the discharge formed during the positive pulse. For ease of measurement, the (emissive) probe was disconnected from it's heating circuitry and it's floating potential was measured using the voltage probe. Figure 6.15 provides the time stamp of the V_f dip found from measurements made at r = 0 mm, z = 61 mm for long positive pulse lengths of varying V_{pp} magnitudes[3]. The dip was located from differentiating the measured V_f oscilloscope data twice and returning the corresponding time stamp of the maximum. For each V_{pp} magnitude, the fireball was captured on the iCCD with formation occurring shortly after the returned time stamp found from figure 6.15. Before the dip,

[3]The data points represent the time from the start of the negative pulse, t = 0.

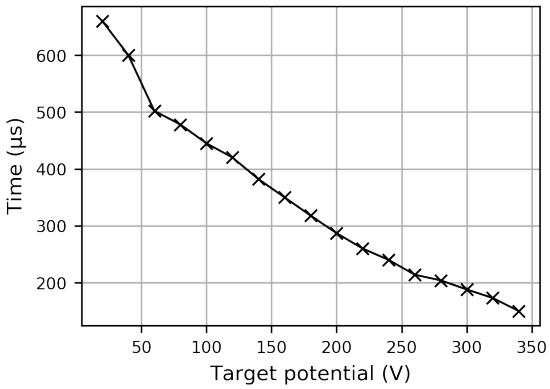

Figure 6.15: A plot of the measured temporal V_f dip at z = 61 mm on the centre-line for successive V_{pp} magnitudes.

homogeneous darkness was imaged on the iCCD, thus confirming the observed trends in figure 6.15. Clearly there exists a link between positive pulse magnitude and the time taken for the secondary discharge to form, with lower applied V_{pp} magnitudes taking longer to ignite.

6.4 Discussion

Upon delivery of the positive pulse, it was shown that V_p rises rapidly at all measured positions in the discharge, following the target voltage closely. There was no evidence to suggest the presence of any (cathode directed) electron accelerating double layer structures created during application of the positive pulse. Such double layer structures are however, seen in other magnetron systems operating under similar conditions [114, 116], responsible for ion acceleration towards the substrate. The highly elevated V_p has significant consequences on the calculated bombarding ion energy flux densities (Q_i) to a grounded substrate as ions are accelerated across the substrate sheath with energies equivalent to V_{pp}. With application of a V_{pp} = 300 V, 300 μs positive pulse, $\langle Q_i \rangle$ increased $\sim$ x 85 of the comparable unipolar pulse.

2D imaging revealed the temporal evolution of the reverse discharges, showing their shape and spatial extent. The plasma clearly redistributes inside the chamber and is heavily shaped by the magnetic field of the magnetron. Similar shaped discharges have also been found by Kozák et al [108] (see figure 2.9), in their unbalanced magnetron bipolar

HiPIMS system. The secondary plasma found in this system was deemed to be a fireball. A fireball is defined as an anode-plasma interaction in which a discharge originates on the anode and extends into the bulk plasma [128]. 2D imaging revealed such a structure is present during the positive pulse of the bipolar HiPIMS system. During the positive voltage phase, a bright dewdrop structure formed, with intense light emission stemming from the centre-line, shaped by the magnetic field topology of the magnetron. Relatively dark regions appeared outside the centre-line close to the target, inside the magnetic trap. LTS measurements showed that these areas have significant density reduction. Close to the target above the racetrack, little electron heating is observed (see figure 6.8).

LTS measurements for V_{pp} = 300 V, t_{pp} = 300 μs, presented in chapter 5, show a rise in electron temperature, within the positive pulse at each measured position. The rise in T_e above the racetrack at z = 15 mm is however, notably stunted. Along the centre-line, the increase in T_e occurs at t $\sim$ 180 μs, for both z = 15 mm and 61 mm. However, the start of the T_e rise above the racetrack is dependent on distance. The z = 65 mm shows the earliest increase, at t $\sim$ 120 μs with latest increase at z = 15 and 25 mm, occurring at t $\sim$ 200 μs. This means, by the time the fireball ignites (t = 220 μs), T_e has risen in all locations. T_e continues to rise till it reaches a maximum at t = 240 μs, this peak correlates with the brightest intensity image as measured by the iCCD camera, linking the fireball ignition to rising electron temperatures. When a V_{pp} = 200 V positive pulse is used, the increase in T_e occurs $\sim$ 100 μs later than the V_{pp} = 300 V case. The observed ignition found from 2D imaging, reflected the same delay.

Using relatively long positive pulses of length $t_{pp} \geq$ 1 ms, a fireball-like structure was found for V_{pp} magnitudes ranging from 340 - 20 V. With successively lower target voltages, the structure appeared on the iCCD later in time after the initiation of the positive pulse. Clearly, there was a time dependant mechanism responsible for the redistribution and bifurcation to the fireball state. Given that both optical output and the T_e of the reverse discharge reduced during the positive pulse, it might be assumed it is not self-sustaining. However, iCCD images of a bipolar pulse with, t_{np} = 50, V_{pp} = 300 V, t_{pp} = 2 ms (not included), show that the discharge is visible until the pulse terminated. A self-sustaining fireball was observed by Chauhan et al [126], using a type-2 unbalanced magnetron with argon gas, with a constant DC positive bias (350 - 550 V) applied to the target (see figure 2.10). Both of these suggest that the fireball is capable of self-sustaining despite the observed cooling and dimming. It should be noted for discharges with $V_{pp} <$ 150 V and t_{pp} = 2 ms, the fireball terminated before the end of the positive pulse, with no significant

light emission captured by the iCCD.

Returning to the equations presented in section 2.2.3, taken from [126], the type of sheath formed during the positive pulse can be estimated. The target used in this work was 150 mm in diameter, with a resultant area of 17.67 x 10^{-3} m^2. Considering the situation in figure 5.3, where, during the lifetime of the fireball, the electron density and temperature is of the order 10^{18} m^{-3} and $\sim$ 3 eV respectively, the electron current (found from equation 2.8), I_{es} = 820 A. This is obviously very large and much greater than the discharge current of the order I_D = 1 A (see figure 5.1). If one takes the effective area of the anode to be the restricted area formed by the magnetic field lines, the area of collection is vastly reduced. Considering the visible glow of the images taken, and the visual span of the glow connected to the anode gives an estimate of this area. From the images presented in this chapter, it was found that the reduced effective area[4] was $\sim$ 1.4 x 10^{-5} m^2. For the same parameters as before, this results in an electron current of $I_{es} \sim 0.65$ A. This satisfies equation 2.9 (c) ($I_{es} < I_D$) and an electron sheath is possible. Similar arguments can also be made using the equations in [127] (equation 2.10), but the exact wall area of the vacuum chamber was hard to estimate due to it's unique design.

It is interesting that, although significant electron heating was observed (reported in section 5.4) downstream of the target within the magnetic trap (15 < z < 45 mm), with application of 200 and 300 V positive voltages, the broad band emission from this region of the plasma is weak, with the bright fireball existing primarily on the centre-line. As discussed in chapter 5, energetic secondary electron release from the vessel walls may contribute to fireball ignition, as the plasma potential V_p rises rapidly everywhere in the plasma close to the value of V_{pp}. It is hypothesised that these secondary electrons, created at the vessel walls through ion bombardment, are accelerated through the wall sheath potential into the bulk plasma. For these hot electrons to enter the magnetic trap, they must cross the field lines, which effectively insulate the bulk plasma from the racetrack region of the target. This low thermal conduction path for electrons leads necessarily to a temperature gradient, with cooling from the outer regions (z = 45 mm) of the trap towards to the target (z = 15 mm) as can been deduced from LTS measurements in chapter 5 (figure 5.9). This may explain the reduced optical emission close to the target (which is acting as a thermal and conductive sink). By contrast, along the centre-line electrons are unimpeded by the magnetic field and no electron temperature gradient is observed.

[4]This is only a rough estimate as defining the glowing area proved difficult.

Relatively high electron temperatures along the centre-line may be responsible for the strong optical emission from this region.

One possibility for hot electrons in the trap at distances far from the target (not associated with secondary electrons from the wall) may be due to the existence of gradients or double layers in the electric potential structure, established by ionisation in the anode sheath; the mechanism responsible for fireball discharges as discussed in section 2.2.2. Similar to Chauhan et al [126] and Zanáška et al [133], radial and axial steps in plasma potential were found to be present over the spatial extent of the fireball. The potential step was of the approximate order of the ionisation energy of the background argon gas which may give some insight into the sustaining mechanism of the fireball.

Regardless of V_{pp} magnitude, a reverse fireball-like plasma ignited during the positive pulse. For low positive pulse magnitudes, the shape of the reverse discharge is significantly different, with smaller extent into the vacuum chamber. LIF studies [99, 130] for similar experimental arrangements and comparable pulses have shown that the magnitude of the applied positive pulse significantly alters ion density evolution. During the positive pulse, the ionisation zone (above the racetrack) significantly shrunk compared to the unipolar pulses and ion acceleration, away from the target was observed. For increasing V_{pp} magnitudes, these effects are more rapid. It can be speculated that the observed time dependant redistribution of ions may have been responsible for the observed delays in fireball ignition. For low V_{pp} pulses, the plasma necessarily takes longer to redistribute inside the chamber, with prolonged ion path to the vessel walls and secondary electron path to the bulk plasma. Hence, bifurcation into the observed fireball state would appear later in time.

Unlike other fireball literature (see section 2.2 and references therein), where the plasma density inside the fireball increases and is measured to be higher than the bulk plasma, only a modest increase in density in locations inside the visual glow was measured by the TS apparatus. Thus, the reverse discharge present in the decaying afterglow may have different features to a classic plasma fireball. However, consistent with fireball literature is the measured higher density on the centre-line (visible glow) compared to regions above the emptying magnetic trap (see figure 6.8). Further spatial diagnostic work would be needed to determine the full density profile and explore the presented phenomenon in the decaying afterglow.

Whatever the cause, this reverse discharge with characteristics analogous to that of a plasma fireball, may be detrimental in industrial thin film production, since its effect on the sputter disposition process is yet unclear. The depletion of electron density, shown in

figure 6.8, would indicate that ions are being removed from the bulk plasma to maintain quasi-neutrality. Ions, leaving the plasma will be accelerated to a grounded substrate. Given the delay between the appearance of the fireball and the end of the negative pulse, ion bombardment will be performed by background gas, not the target material. This may enhance the ion-assisted process [213, 214], however it is likely to have a detectable effect on the deposited films, increasing ion power flux to the growing film. There was evidence from optical emission studies that elevated plasma potentials in positive pulse period may lead to some wall sputtering (chapter 5 and [1]). The development of a burning fireball on the discharge centre-line rooted to the target, may result in a source of unwanted metallic species at high V_{pp} magnitudes.

6.5 Conclusion

Using broad band 2D optical imaging and emissive probe measurements, direct evidence of the ignition of discharges with characteristics (length and shape) of a fireball during the positive pulse of bipolar HiPIMS has been provided. The fireball does not form immediately on the initiation of the positive pulse. With increasing V_{pp}, the fireball appeared sooner on the iCCD, with respect to the positive pulse initiation. It is heavily shaped by the magnetic field structure of the magnetron, sitting primarily on the magnetron centre-line, attached to the positive target. Reverse fireball-like discharges were imaged at positive pulse magnitudes as low as 20 V.

The formation of a fireball in the experimental system used in this work may be explained following the discussion by Chauhan et al [126]. In their system, fireballs form due to a constriction of the target surface area during the afterglow. The magnetised electrons follow the magnetic field lines, unable to cross into the magnetic trap, sinking at the positive target surface. This resulted in the formation of an electron sheath which necessarily increases the effective collection area of the anode. They observed a double layer both axially and radially through the fireball and bulk plasma. The situation in bipolar HiPIMS however, is further complicated due to the fact that the positive pulse is delivered to a dense HiPIMS pulse afterglow.

Plasma potential measurements, using an emissive probe combined with T_e and n_e found from TS, allowed the fluxes of ions to a substrate to be estimated throughout the bipolar waveform. V_p was found to rise almost instantaneously at all measured positions when the positive pulse was delivered to the target, closely following the target voltage

shape and magnitude. For $V_{pp} = 300$ V, this resulted in a vast increase in the time averaged energy flux density, compared to unipolar operation. Although no double layer structure was found during the initiation of the positive pulse, a potential structure developed during the fireball phase, similar to what was observed by Zanáška et al [133]. This may be responsible for sustaining the fireball throughout the positive pulse in this system.

This ignition of a fireball-like discharge, during the positive pulse delivery, may well be an unwanted side effect in bipolar HiPIMS configuration. The exact mechanisms that produce and sustain the fireball are still not fully understood: It could for instance be due to the generation of energetic electrons by bulk plasma electric fields above the target centre, close to the anode or, from hot electrons produced via secondary electron emission from the walls.

Chapter 7

Conclusions and Suggested Further Work

7.1 Discussion of Results and Summary of Findings

This thesis was concerned with characterising bipolar HiPIMS discharges using plasma diagnostic techniques, with focus on the positive afterglow dynamics. Results from Thomson scattering, optical emission spectroscopy, emissive probe and broad band 2D imaging have been presented. All of these techniques combined allowed temporal measurements of T_e, n_e, V_p, optical emission and visual structure of bipolar HiPIMS discharges to be obtained. To the authors knowledge, the results presented in this thesis are the first use of Thomson scattering in diagnosing bipolar HiPIMS and at the time of writing, is the only study. The diagnostic project led to the discovery of fireball-like discharges appearing during the positive pulse delivery in the bipolar HiPIMS magnetron system.

The incoherent laser Thomson scattering system used in this work enabled high fidelity electron property measurements on bipolar HiPIMS discharges to be made, with negligible perturbing effects to the plasma. The interpretation of the data is unambiguous, with simple data analysis. The LTS results revealed that during the positive pulse period of the bipolar HiPIMS waveform, significant electron heating was observed both on the centre-line and above the target racetrack. The heating was found to appear later in time during the positive pulse for successively lower positive pulse magnitudes. Centre-line measurements revealed that at positions z = 15 mm and z = 61 mm, T_e rose simultaneously, peaking at comparable values with little change in n_e compared to the unipolar case. However

above the racetrack, little heating was observed at z = 15 mm. T_e above the racetrack, rose sooner at greater distance from the target and n_e dropped 5 fold in the magnetic trap compared to unipolar pulsing. The increases in T_e was deemed to be a signature of a secondary discharge.

Optical emission spectroscopy was used to track the temporal evolution of line emissions of gas and metal species inside the plasma. This required little alteration to the experimental design. The results presented in this thesis focused on two visible, distinguishable line emissions of Ar(I) and W(I) and presented as relative intensities, where a temporal profile was normalised to the maximum in that particular scan. Ar(II) and W(II) emission lines were also tracked, but during the positive pulse, it was found that the intensities of emission dropped to undetectable levels. It was revealed that, compared to the unipolar pulse, Ar(I) was detectable through the positive pulse when positive pulses $\geq$ 200 V were used. The relative intensities of Ar(I) followed the trends observed in T_e at all positions measured, whereas W(I) intensity decayed throughout the positive pulse. The reappearance of argon emission during the positive pulse provided further evidence of the presence of a reverse discharge in the bipolar HiPIMS positive afterglow. Excited tungsten emission suggested that a new source of metal species may have been created in the plasma. This was explained by re-sputtering of tungsten from the chamber walls through bombardment of ions falling through the large sheath potential.

An emissive probe was used to track the temporal and spatial evolution of plasma potential. The system had time resolution of $<$ 100 ns, and measured V_p within $\sim$ 1.5 T_e. Measurements revealed that on the initiation of the positive pulse, V_p rose simultaneously to the target waveform, matching the applied V_{pp}. During the early positive pulse, V_p was measured at values greater than the applied target potential. Later in the positive pulse, a dip in V_p was measured, with minimum values found at approximately the same time as T_e was seen to rise by LTS measurement. Spatial measurements revealed that V_p rose instantaneously at all measured positions and calculations of ion flux and ion energy flux densities showed a large increase to a grounded substrate. No moving double layer was found during the positive pulse, however some evidence was found that suggested a structure formed during the positive pulse with similarities seen in other fireball literature. Centre-line V_f measurements provided an estimate of when, temporally, a reverse discharge would be expected to ignite in the system at a given V_{pp} magnitude.

2D broad band optical imaging was performed throughout the positive pulse for different positive pulse lengths and magnitudes. Images were taken over 100 plasma pulses with

a an exposure of 2 μs. The images revealed the structure of the reverse discharge, which was indistinguishable from fireballs imaged in other literature. The fireballs produced were anchored to the positive target and shaped by the magnetic field of the magnetron with little emission seen in the magnetic trap. The light intensity, elevated T_e and V_p dip were all seen to be correlated temporally, with a T_e increase occurring at approximately the same time as a V_p dip. Fireball establishment is delayed relative to the initiation of the positive pulse, with the delay time shortening with increased V_{pp} and have lifetimes extending to the end of the positive pulse. Images of bipolar HiPIMS discharges revealed that a fireball-like discharge ignited in the positive pulse for V_{pp} magnitudes as low as 20 V.

It was speculated that secondary electron release from the vessel walls through ion bombardment may be responsible for the formation of the fireball. During the positive pulse, the target is acting as an anode and V_p was found to elevate to values comparable to V_{pp}, at all measured positions. In this scenario, the grounded vessel walls are the cathode, effectively biased at -V_p relative to the bulk plasma. Ions are accelerated through the wall sheath potentials, liberating secondary electrons and for large V_{pp} magnitudes, possibly re-sputtering deposited material. The electrons extracted at the walls will be accelerated through the wall sheath into the bulk plasma, where they thermalise. The positive target acts as a sink for the electrons, with their paths determined by the magnetic field structure. Electron path to the target through the magnetic trap is impeded as they can not readily cross the field lines. On the centre-line however, there is a direct path to the target. This gives the fireball the unique shape as shown by 2D (broad band) imaging, with the glow situated primarily on the discharge centre-line.

From the literature, it has been shown that at the visible boundary of the fireball glow there is a potential step (double layer) with magnitude analogue to the first ionisation energy of the backing gas. Electrons and ions will be accelerated across this layer and is the mechanism responsible for sustaining the discharge. In this work, there was evidence of a similar structure forming during the fireball lifetime, which may explain how the discharge was sustained for long positive pulses. Comparing the target current and estimated electron saturation current during the positive pulse period, allowed the determination of the sheath present at the anode boundary. This was found to be an electron rich sheath. During the positive pulse, the magnetic field of the magnetron significantly reduces the target surface area and the subsequent electron sheath increases the effective area of collection.

The fireballs are ignited in a decaying HiPIMS plasma afterglow and the mechanisms

that produce and sustain the fireballs are not yet fully understood. Secondary electron release from the walls and the formation of an electron sheath and double layer in the system may go some way to explain the presence of a fireball in the bipolar HiPIMS system however, more work is needed to fully understand the phenomena presented in this thesis. Regardless of the cause, the fireball may be parasitic to bipolar HiPIMS operation, as the effects on thin film growth is currently unknown. The possibility of re-sputtering material deposited on the vessel walls for high V_{pp} magnitudes would give further unwanted coating conditions.

7.2 Future Work

It is clear from the results presented in this thesis that further work is needed to fully understand the mechanisms involved that ignite and sustain a fireball, during the positive afterglow of bipolar HiPIMS systems. A more pressing question is, what effect both large positive pulse magnitudes and presence of a fireball may have on deposited films. It was shown that the plasma potential of the bulk plasma quickly matches that of the positive pulse in the afterglow and hence, ions incident on a (grounded) substrate and vacuum vessel walls would be bombarded with energies comparable to V_p. This may result in re-sputtering of deposited material, providing a new source of metal ions in the plasma. Secondary electron emission and fireball production could provide a new source of argon ions in the afterglow which would be accelerated to the substrate through the sheath potential. Experiments growing films on substrates placed in bipolar HiPIMS systems, where a fireball was present, would be needed to fully understand it's effect.

Although the laser Thomson scattering system provided accurate electron property measurements, unparalleled by conventional invasive diagnostics, in this system, it inherently had a relatively high density detection limit. This meant that electron property measurements could not be made deep into the positive afterglow and the fireballs produced at low V_{pp} magnitudes could not be diagnosed. A diagnostic study utilising techniques that could measure lower plasma densities or alterations to the current system enabling lower density plasma to be measured would be beneficial.

Due to time constraints, the emissive probe study was kept short and focused on the $V_{pp} = 300$ V positive pulse case, with limited measurement positions. An extensive spatio-temporal V_p scan would be useful to determine the full potential structure throughout the positive pulse at differing positive pulse magnitudes. This may give insight into the

mechanisms that both ignite and sustain the fireball and may also reveal the differences in shape and spatial extent seen by 2D imaging between high and low V_{pp} magnitudes.

Broad band 2D imaging provided excellent images of the fireball and its temporal evolution. The next stage would be the use of optical filters placed between the viewing port and camera lens, enabling light of a specific wavelength range to be collected. With correctly selected filters, it would be possible to track ion and neutral emission throughout the pulse, providing details on the composition of the plasma. A further extension to this would be the use of an Abel inversion technique applied to the images post processing (see for example [96]). The technique takes advantage of radial symmetry and would provide radial emission profiles, showing the true radial profile of the fireball. Optical imaging spectroscopy as a means to gather bulk n_e and T_e values could also be explored as in [198].

The results presented in this thesis predominantly covered bipolar HiPIMS discharges with varying positive pulse lengths and magnitudes. The negative pulse length, power and delay between negative and positive pulses were fixed. A direct extension of this research would therefore be to explore this parameter space and diagnose the subsequent positive afterglows. The experiments used a circular planar unbalanced magnetron as the plasma source, with tungsten target situated in an argon atmosphere. Experiments using different magnetic field structures (and or different shaped magnetrons) would be an interesting study to validate the sheath structure suggested by Chauhan et al [126] as the effective collection area of the target could be altered. Furthermore, the effect of magnetic field on the fireball shape and extent could be examined. Experiments with different target materials with different atomic masses and sputtering yields could be of interest to further examine the re-sputtering effects suggested in this work. A brief experiment with other inert backing gasses would be of interest, to see if the potential steps found in this work scale with first ionisation energies.

References

[1] M. A. Law, F. Lockwood Estrin, M. D. Bowden, and J. W. Bradley, "Diagnosing asymmetric bipolar hipims discharges using laser thomson scattering," *Plasma Sources Science and Technology*, vol. 30, no. 10, p. 105019, 2021.

[2] M. A. Law, F. Lockwood Estrin, P. M. Bryant, M. D. Bowden, and J. W. Bradley, "Evidence for fireballs in bipolar hipims plasmas," *Plasma Sources Science and Technology*, vol. 32, no. 2, p. 025015, 2023.

[3] I. Langmuir, "Oscillations in ionized gases," *Proceedings of the National Academy of Sciences of the United States of America*, vol. 14, no. 8, p. 627, 1928.

[4] F. F. Chen *et al.*, *Introduction to plasma physics and controlled fusion*, vol. 1. Springer, 1984.

[5] C. Tendero, C. Tixier, P. Tristant, J. Desmaison, and P. Leprince, "Atmospheric pressure plasmas: A review," *Spectrochimica Acta Part B: Atomic Spectroscopy*, vol. 61, no. 1, pp. 2–30, 2006.

[6] A. Bogaerts, E. Neyts, R. Gijbels, and J. Van der Mullen, "Gas discharge plasmas and their applications," *Spectrochimica Acta Part B: Atomic Spectroscopy*, vol. 57, no. 4, pp. 609–658, 2002.

[7] J. T. Gudmundsson and D. Lundin, "Introduction to magnetron sputtering," in *High Power Impulse Magnetron Sputtering*, pp. 1–48, Elsevier, 2020.

[8] F. Paschen, "Ueber die zum funkenübergang in luft, wasserstoff und kohlensäure bei verschiedenen drucken erforderliche potentialdifferenz," *Annalen der Physik*, vol. 273, no. 5, pp. 69–96, 1889.

[9] J. S. Townsend, *Electrons in gases*. Hutchinson' Scientific and Technical Publications, London, 1947.

[10] M. A. Lieberman and A. J. Lichtenberg, *Principles of plasma discharges and materials processing*. John Wiley & Sons, 2005.

[11] A. H. Simon, "Chapter 7 - sputter processing," in *Handbook of Thin Film Deposition (Fourth Edition)* (K. Seshan and D. Schepis, eds.), pp. 195 – 230, William Andrew Publishing, fourth edition ed., 2018.

[12] J. T. Gudmundsson, A. Anders, and A. von Keudell, "Foundations of physical vapor deposition with plasma assistance," *Plasma Sources Science and Technology*, 2022.

[13] J. E. Mahan, *Physical vapor deposition of thin films*. John Wiley and Sons Inc, 2000.

[14] M. W. Thompson, "Ii. the energy spectrum of ejected atoms during the high energy sputtering of gold," *Philosophical Magazine*, vol. 18, no. 152, pp. 377–414, 1968.

[15] A. Goehlich, N. Niemöller, and H. Döbele, "Determination of angle resolved velocity distributions of sputtered tungsten atoms," *Journal of nuclear materials*, vol. 266, pp. 501–506, 1999.

[16] A. Anders, "Tutorial: Reactive high power impulse magnetron sputtering (r-hipims)," *Journal of applied physics*, vol. 121, no. 17, p. 171101, 2017.

[17] V. V. Serikov and K. Nanbu, "The analysis of background gas heating in direct current sputtering discharges via particle simulation," *Journal of applied physics*, vol. 82, no. 12, pp. 5948–5957, 1997.

[18] H. D. Hagstrum, "Auger ejection of electrons from tungsten by noble gas ions," *Physical Review*, vol. 96, no. 2, p. 325, 1954.

[19] H. D. Hagstrum, "Theory of auger ejection of electrons from metals by ions," *Physical Review*, vol. 96, no. 2, p. 336, 1954.

[20] R. Baragiola, E. Alonso, J. Ferron, and A. Oliva-Florio, "Ion-induced electron emission from clean metals," *Surface Science*, vol. 90, 1979.

[21] A. Anders, J. Andersson, and A. Ehiasarian, "High power impulse magnetron sputtering: Current-voltage-time characteristics indicate the onset of sustained self-sputtering," *Journal of Applied Physics*, vol. 102, no. 11, p. 113303, 2007.

[22] D. Mattox, "Particle bombardment effects on thin-film deposition: A review," *Journal of Vacuum Science & Technology A: Vacuum, Surfaces, and Films*, vol. 7, no. 3, pp. 1105–1114, 1989.

[23] J. Bradley, H. Bäcker, Y. Aranda-Gonzalvo, P. Kelly, and R. Arnell, "The distribution of ion energies at the substrate in an asymmetric bi-polar pulsed dc magnetron discharge," *Plasma sources science and technology*, vol. 11, no. 2, p. 165, 2002.

[24] R. P. B. Viloan, J. Gu, R. Boyd, J. Keraudy, L. Li, and U. Helmersson, "Bipolar high power impulse magnetron sputtering for energetic ion bombardment during tin thin film growth without the use of a substrate bias," *Thin Solid Films*, vol. 688, p. 137350, 2019.

[25] W. Ensinger, "Low energy ion assist during deposition—an effective tool for controlling thin film microstructure," *Nuclear Instruments and Methods in Physics Research Section B: Beam Interactions with Materials and Atoms*, vol. 127, pp. 796–808, 1997.

[26] S. Rossnagel and J. Cuomo, "Ion beam bombardment effects during films deposition," *Vacuum*, vol. 38, no. 2, pp. 73–81, 1988.

[27] J. S. Colligon, "Energetic condensation: Processes, properties, and products," *Journal of Vacuum Science & Technology A: Vacuum, Surfaces, and Films*, vol. 13, no. 3, pp. 1649–1657, 1995.

[28] K. Sarakinos and L. Martinu, "Synthesis of thin films and coatings by high power impulse magnetron sputtering," in *High Power Impulse Magnetron Sputtering*, pp. 333–374, Elsevier, 2020.

[29] E. Kay, "Magnetic field effects on an abnormal truncated glow discharge and their relation to sputtered thin-film growth," *Journal of Applied Physics*, vol. 34, no. 4, pp. 760–768, 1963.

[30] W. Gill and E. Kay, "Efficient low pressure sputtering in a large inverted magnetron suitable for film synthesis," *Review of Scientific Instruments*, vol. 36, no. 3, pp. 277–282, 1965.

[31] G. Bräuer, B. Szyszka, M. Vergöhl, and R. Bandorf, "Magnetron sputtering–milestones of 30 years," *Vacuum*, vol. 84, no. 12, pp. 1354–1359, 2010.

[32] J. S. Chapin, "The planar magnetron," *Research Development*, vol. 25, no. 1, pp. 37–40, 1974.

[33] J. S. Chapin, "Sputtering process and apparatus," US Patent 4,166,018 A, August 28, 1979.

[34] D. Krüger, K. Köhn, S. Gallian, and R. P. Brinkmann, "Reconstruction of the static magnetic field of a magnetron," *Physics of Plasmas*, vol. 25, no. 6, p. 061207, 2018.

[35] J. Bradley, S. Thompson, and Y. A. Gonzalvo, "Measurement of the plasma potential in a magnetron discharge and the prediction of the electron drift speeds," *Plasma Sources Science and Technology*, vol. 10, no. 3, p. 490, 2001.

[36] R. K. Waits, "Planar magnetron sputtering," *Journal of Vacuum Science and Technology*, vol. 15, no. 2, pp. 179–187, 1978.

[37] P. J. Kelly and R. D. Arnell, "Magnetron sputtering: a review of recent developments and applications," *Vacuum*, vol. 56, no. 3, pp. 159–172, 2000.

[38] J. T. Gudmundsson, "Physics and technology of magnetron sputtering discharges," *Plasma Sources Science and Technology*, vol. 29, no. 11, p. 113001, 2020.

[39] B. Window and N. Savvides, "Unbalanced dc magnetrons as sources of high ion fluxes," *Journal of Vacuum Science & Technology A: Vacuum, Surfaces, and Films*, vol. 4, no. 3, pp. 453–456, 1986.

[40] B. Window and N. Savvides, "Charged particle fluxes from planar magnetron sputtering sources," *Journal of Vacuum Science & Technology A*, vol. 4, no. 2, pp. 196–202, 1986.

[41] R. De Gryse, J. Haemers, W. Leroy, and D. Depla, "Thirty years of rotatable magnetrons," *Thin Solid Films*, vol. 520, no. 18, pp. 5833–5845, 2012.

[42] A. Anders, "Physics of arcing, and implications to sputter deposition," *Thin Solid Films*, vol. 502, no. 1-2, pp. 22–28, 2006.

[43] J. Sellers, "Asymmetric bipolar pulsed dc: the enabling technology for reactive pvd," *Surface and Coatings Technology*, vol. 98, no. 1-3, pp. 1245–1250, 1998.

[44] V. Kouznetsov, K. Macak, J. M. Schneider, U. Helmersson, and I. Petrov, "A novel pulsed magnetron sputter technique utilizing very high target power densities," *Surface and coatings technology*, vol. 122, no. 2-3, pp. 290–293, 1999.

[45] D. Lundin, T. Minea, and J. T. Gudmundsson, *High Power Impulse Magnetron Sputtering: Fundamentals, Technologies, Challenges and Applications*. Elsevier, 2019.

[46] M. Samuelsson, D. Lundin, J. Jensen, M. A. Raadu, J. T. Gudmundsson, and U. Helmersson, "On the film density using high power impulse magnetron sputtering," *Surface and Coatings Technology*, vol. 205, no. 2, pp. 591–596, 2010.

[47] J. Paulitsch, M. Schenkel, T. Zufraß, P. Mayrhofer, and W.-D. Münz, "Structure and properties of high power impulse magnetron sputtering and dc magnetron sputtering crn and tin films deposited in an industrial scale unit," *Thin Solid Films*, vol. 518, no. 19, pp. 5558 – 5564, 2010.

[48] F. Magnus, A. S. Ingason, O. Sveinsson, S. Olafsson, and J. Gudmundsson, "Morphology of tin thin films grown on sio2 by reactive high power impulse magnetron sputtering," *Thin Solid Films*, vol. 520, no. 5, pp. 1621–1624, 2011.

[49] J. Gudmundsson, N. Brenning, D. Lundin, and U. Helmersson, "High power impulse magnetron sputtering discharge," *Journal of Vacuum Science & Technology A: Vacuum, Surfaces, and Films*, vol. 30, no. 3, p. 030801, 2012.

[50] U. Helmersson, M. Lattemann, J. Bohlmark, A. P. Ehiasarian, and J. T. Gudmundsson, "Ionized physical vapor deposition (ipvd): A review of technology and applications," *Thin solid films*, vol. 513, no. 1-2, pp. 1–24, 2006.

[51] A. Anders, "Discharge physics of high power impulse magnetron sputtering," *Surface and Coatings Technology*, vol. 205, pp. S1 – S9, 2011. PSE 2010 Special Issue.

[52] P. Vašina, M. Meško, L. De Poucques, J. Bretagne, C. Boisse-Laporte, and M. Touzeau, "Study of a fast high power pulsed magnetron discharge: role of plasma deconfinement on the charged particle transport," *Plasma Sources Science and Technology*, vol. 17, no. 3, p. 035007, 2008.

[53] A. Anders, J. Andersson, and A. Ehiasarian, "High power impulse magnetron sputtering: Current-voltage-time characteristics indicate the onset of sustained self-sputtering," *Journal of Applied Physics*, vol. 102, no. 11, p. 113303, 2007.

[54] A. Butler, N. Brenning, M. A. Raadu, J. T. Gudmundsson, T. Minea, and D. Lundin, "On three different ways to quantify the degree of ionization in sputtering magnetrons," *Plasma Sources Science and Technology*, vol. 27, no. 10, p. 105005, 2018.

[55] J. Gudmundsson, "Ionization mechanism in the high power impulse magnetron sputtering (hipims) discharge," in *Journal of Physics: Conference Series*, vol. 100, p. 082013, IOP Publishing, 2008.

[56] J. Hopwood and F. Qian, "Mechanisms for highly ionized magnetron sputtering," *Journal of Applied Physics*, vol. 78, no. 2, pp. 758–765, 1995.

[57] S. Rossnagel, "Gas density reduction effects in magnetrons," *Journal of Vacuum Science & Technology A: Vacuum, Surfaces, and Films*, vol. 6, no. 1, pp. 19–24, 1988.

[58] C. Huo, D. Lundin, M. A. Raadu, A. Anders, J. T. Gudmundsson, and N. Brenning, "On sheath energization and ohmic heating in sputtering magnetrons," *Plasma Sources Science and Technology*, vol. 22, no. 4, p. 045005, 2013.

[59] D. Hoffman, "A sputtering wind," *Journal of Vacuum Science & Technology A: Vacuum, Surfaces, and Films*, vol. 3, no. 3, pp. 561–566, 1985.

[60] S. Kadlec, "Simulation of neutral particle flow during high power magnetron impulse," *Plasma Processes and Polymers*, vol. 4, no. S1, pp. S419–S423, 2007.

[61] D. Lundin, N. Brenning, D. Jädernäs, P. Larsson, E. Wallin, M. Lattemann, M. A. Raadu, and U. Helmersson, "Transition between the discharge regimes of high power impulse magnetron sputtering and conventional direct current magnetron sputtering," *Plasma Sources Science and Technology*, vol. 18, no. 4, p. 045008, 2009.

[62] J. Andersson and A. Anders, "Gasless sputtering: Opportunities for ultraclean metallization, coatings in space, and propulsion," *Applied Physics Letters*, vol. 92, no. 22, p. 221503, 2008.

[63] J. Andersson and A. Anders, "Self-sputtering far above the runaway threshold: an extraordinary metal-ion generator," *Physical review letters*, vol. 102, no. 4, p. 045003, 2009.

[64] A. Anders, J. Čapek, M. Hála, and L. Martinu, "The 'recycling trap': a generalized explanation of discharge runaway in high-power impulse magnetron sputtering," *Journal of physics D: Applied physics*, vol. 45, no. 1, p. 012003, 2011.

[65] D. Christie, "Target material pathways model for high power pulsed magnetron sputtering," *Journal of Vacuum Science & Technology A: Vacuum, Surfaces, and Films*, vol. 23, no. 2, pp. 330–335, 2005.

[66] N. Brenning, C. Huo, D. Lundin, M. A. Raadu, C. Vitelaru, G. Stancu, T. Minea, and U. Helmersson, "Understanding deposition rate loss in high power impulse magnetron sputtering: I. ionization-driven electric fields," *Plasma Sources Science and Technology*, vol. 21, no. 2, p. 025005, 2012.

[67] N. Brenning, A. Butler, H. Hajihoseini, M. Rudolph, M. A. Raadu, J. T. Gudmundsson, T. Minea, and D. Lundin, "Optimization of hipims discharges: The selection of pulse power, pulse length, gas pressure, and magnetic field strength," *Journal of Vacuum Science & Technology A: Vacuum, Surfaces, and Films*, vol. 38, no. 3, p. 033008, 2020.

[68] A. Mishra, P. Kelly, and J. Bradley, "The evolution of the plasma potential in a hipims discharge and its relationship to deposition rate," *Plasma Sources Science and Technology*, vol. 19, no. 4, p. 045014, 2010.

[69] H. Hajihoseini, M. Čada, Z. Hubička, S. Ünaldi, M. A. Raadu, N. Brenning, J. T. Gudmundsson, and D. Lundin, "The effect of magnetic field strength and geometry on the deposition rate and ionized flux fraction in the hipims discharge," *Plasma*, vol. 2, no. 2, pp. 201–221, 2019.

[70] J. Čapek, M. Hála, O. Zabeida, J. Klemberg-Sapieha, and L. Martinu, "Deposition rate enhancement in hipims without compromising the ionized fraction of the deposition flux," *Journal of Physics D: Applied Physics*, vol. 46, no. 20, p. 205205, 2013.

[71] H. Hajihoseini and J. T. Gudmundsson, "Vanadium and vanadium nitride thin films grown by high power impulse magnetron sputtering," *Journal of Physics D: Applied Physics*, vol. 50, no. 50, p. 505302, 2017.

[72] J. McLain, P. Raman, D. Patel, R. Spreadbury, J. Uhlig, I. Shchelkanov, and D. Ruzic, "Linear magnetron hipims high deposition rate magnet pack," *Vacuum*, vol. 155, pp. 559–565, 2018.

[73] V. Tiron, I.-L. Velicu, I. Mihăilă, and G. Popa, "Deposition rate enhancement in hipims through the control of magnetic field and pulse configuration," *Surface and Coatings Technology*, vol. 337, pp. 484–491, 2018.

[74] M. Rudolph, N. Brenning, M. A. Raadu, H. Hajihoseini, J. T. Gudmundsson, A. Anders, and D. Lundin, "Optimizing the deposition rate and ionized flux fraction by tuning the pulse length in high power impulse magnetron sputtering," *Plasma Sources Science and Technology*, vol. 29, no. 5, p. 05LT01, 2020.

[75] T. Shimizu, M. Zanáška, R. Villoan, N. Brenning, U. Helmersson, and D. Lundin, "Experimental verification of deposition rate increase, with maintained high ionized flux fraction, by shortening the hipims pulse," *Plasma Sources Science and Technology*, vol. 30, no. 4, p. 045006, 2021.

[76] B.-S. Lou, W.-T. Chen, W. Diyatmika, J.-H. Lu, C.-T. Chang, P.-W. Chen, and J.-W. Lee, "Effect of target poisoning ratios on the fabrication of titanium oxide coatings using superimposed high power impulse and medium frequency magnetron sputtering," *Surface and Coatings Technology*, vol. 421, p. 127430, 2021.

[77] N. Brenning, H. Hajihoseini, M. Rudolph, M. A. Raadu, J. T. Gudmundsson, T. M. Minea, and D. Lundin, "Hipims optimization by using mixed high-power and low-power pulsing," *Plasma Sources Science and Technology*, vol. 30, no. 1, p. 015015, 2021.

[78] Z. Hubička, J. T. Gudmundsson, P. Larsson, and D. Lundin, "2 - hardware and power management for high power impulse magnetron sputtering," in *High Power Impulse Magnetron Sputtering* (D. Lundin, T. Minea, and J. T. Gudmundsson, eds.), pp. 49–80, Elsevier, 2020.

[79] A. Kozyrev, N. Sochugov, K. Oskomov, A. Zakharov, and A. Odivanova, "Optical studies of plasma inhomogeneities in a high-current pulsed magnetron discharge," *Plasma Physics Reports*, vol. 37, no. 7, pp. 621–627, 2011.

[80] A. Hecimovic and A. Von Keudell, "Spokes in high power impulse magnetron sputtering plasmas," *Journal of Physics D: Applied Physics*, vol. 51, no. 45, p. 453001, 2018.

[81] N. Britun, T. Minea, S. Konstantinidis, and R. Snyders, "Plasma diagnostics for understanding the plasma–surface interaction in hipims discharges: a review," *Journal of Physics D: Applied Physics*, vol. 47, no. 22, p. 224001, 2014.

[82] H. M. Mott-Smith and I. Langmuir, "The theory of collectors in gaseous discharges," *Physical review*, vol. 28, no. 4, p. 727, 1926.

[83] R. Hippler, M. Cada, and Z. Hubicka, "Time-resolved Langmuir probe diagnostics of a bipolar high power impulse magnetron sputtering discharge," *Applied Physics Letters*, vol. 116, 2 2020.

[84] E. Johnson and L. Malter, "A floating double probe method for measurements in gas discharges," *Physical Review*, vol. 80, no. 1, p. 58, 1950.

[85] T. Welzel, T. Dunger, H. Kupfer, and F. Richter, "A time-resolved langmuir double-probe method for the investigation of pulsed magnetron discharges," *Journal of applied physics*, vol. 96, no. 12, pp. 6994–7001, 2004.

[86] S.-L. Chen and T. Sekiguchi, "Instantaneous direct-display system of plasma parameters by means of triple probe," *Journal of Applied Physics*, vol. 36, no. 8, pp. 2363–2375, 1965.

[87] H. Yu, L. Meng, M. M. Szott, J. T. McLain, T. S. Cho, and D. N. Ruzic, "Investigation and optimization of the magnetic field configuration in high-power impulse magnetron sputtering," *Plasma sources science and technology*, vol. 22, no. 4, p. 045012, 2013.

[88] S. Sharma, D. Gahan, P. Scullin, J. Doyle, J. Lennon, R. K. Vijayaraghavan, S. Daniels, and M. Hopkins, "Measurement of deposition rate and ion energy distribution in a pulsed dc magnetron sputtering system using a retarding field analyzer with

embedded quartz crystal microbalance," *Review of Scientific Instruments*, vol. 87, no. 4, p. 043511, 2016.

[89] F. Walk, R. Valizadeh, and J. W. Bradley, "Ion energy analysis of a bipolar hipims discharge using a retarding field energy analyser," *Plasma Sources Science and Technology*, 2022.

[90] J. Benedikt, A. Hecimovic, D. Ellerweg, and A. Von Keudell, "Quadrupole mass spectrometry of reactive plasmas," *Journal of Physics D: Applied Physics*, vol. 45, no. 40, p. 403001, 2012.

[91] R. Snyders, R. Gouttebaron, J. Dauchot, and M. Hecq, "Mass spectrometry diagnostic of dc magnetron reactive sputtering," *Journal of Analytical Atomic Spectrometry*, vol. 18, no. 6, pp. 618–623, 2003.

[92] M. Mišina, J. W. Bradley, H. Bäcker, Y. Aranda-Gonzalvo, S. K. Karkari, and D. Forder, "Investigation of the pulsed magnetron discharge by time-and energy-resolved mass spectrometry," *Vacuum*, vol. 68, no. 2, pp. 171–181, 2002.

[93] M. Bowes, *Plasma diagnosis of reactive high power impulse magnetron sputtering (HiPIMS) discharges*. PhD thesis, University of Liverpool, 2014.

[94] R. P. B. Viloan, M. Zanáška, D. Lundin, and U. Helmersson, "Pulse length selection for optimizing the accelerated ion flux fraction of a bipolar hipims discharge," *Plasma Sources Science and Technology*, vol. 29, no. 12, p. 125013, 2020.

[95] S. Gueron and M. Deutsch, "A fast abel inversion algorithm," *Journal of applied physics*, vol. 75, no. 9, pp. 4313–4318, 1994.

[96] B. Liebig, N. S. J. Braithwaite, P. Kelly, and J. Bradley, "Spatial and temporal investigation of high power pulsed magnetron discharges by optical 2d-imaging," *Thin Solid Films*, vol. 519, no. 5, pp. 1699–1704, 2010.

[97] M. Palmucci, N. Britun, S. Konstantinidis, and R. Snyders, "Rarefaction windows in a high-power impulse magnetron sputtering plasma," *Journal of Applied Physics*, vol. 114, no. 11, p. 113302, 2013.

[98] C. Vitelaru, L. De Poucques, T. Minea, and G. Popa, "Space-resolved velocity and flux distributions of sputtered ti atoms in a planar circular magnetron discharge," *Plasma Sources Science and Technology*, vol. 20, no. 4, p. 045020, 2011.

[99] N. Britun, M. Michiels, T. Godfroid, and R. Snyders, "Ion density evolution in a high-power sputtering discharge with bipolar pulsing," *Applied Physics Letters*, vol. 112, no. 23, p. 234103, 2018.

[100] P. J. Ryan, J. W. Bradley, and M. D. Bowden, "Comparison of Langmuir probe and laser Thomson scattering for electron property measurements in magnetron discharges," *Physics of Plasmas*, vol. 26, 7 2019.

[101] P. J. Ryan, J. W. Bradley, and M. D. Bowden, "Comparison of Langmuir probe and laser Thomson scattering for plasma density and electron temperature measurements in HiPIMS plasma," *Physics of Plasmas*, vol. 26, 4 2019.

[102] S. Tsikata, B. Vincent, T. Minea, A. Revel, and C. Ballage, "Time-resolved electron properties of a HiPIMS argon discharge via incoherent Thomson scattering," *Plasma Sources Science and Technology*, vol. 28, 3 2019.

[103] T. Dubois, S. Tsikata, and T. Minea, "Dynamic features of the electron drift and electron properties in a hipims discharge," *Plasma Sources Science and Technology*, vol. 31, no. 11, p. 115018, 2022.

[104] B. Wu, I. Haehnlein, I. Shchelkanov, J. McLain, D. Patel, J. Uhlig, B. Jurczyk, Y. Leng, and D. N. Ruzic, "Cu films prepared by bipolar pulsed high power impulse magnetron sputtering," *Vacuum*, vol. 150, pp. 216–221, 2018.

[105] V. Tiron, E. L. Ursu, D. Cristea, D. Munteanu, G. Bulai, A. Ceban, and I. L. Velicu, "Overcoming the insulating materials limitation in HiPIMS: Ion-assisted deposition of DLC coatings using bipolar HiPIMS," *Applied Surface Science*, vol. 494, pp. 871–879, 11 2019.

[106] M. G. Cho, U. Kang, S. H. Lim, and S. Han, "a-phase tantalum film deposition using bipolar high-power impulse magnetron sputtering technique," *Thin Solid Films*, p. 139668, 2023.

[107] J. A. Santiago, I. Fernández-Martínez, T. Kozák, J. Capek, A. Wennberg, J. M. Molina-Aldareguia, V. Bellido-González, R. González-Arrabal, and M. A. Monclús, "The influence of positive pulses on HiPIMS deposition of hard DLC coatings," *Surface and Coatings Technology*, vol. 358, pp. 43–49, 1 2019.

[108] T. Kozák, A. D. Pajdarová, M. Čada, Z. Hubička, P. Mareš, and J. Čapek, "Ion energy distributions at substrate in bipolar HiPIMS: Effect of positive pulse delay, length and amplitude," *Plasma Sources Science and Technology*, vol. 29, 6 2020.

[109] A. Vetushka and J. W. Bradley, "The current-density distribution in a pulsed dc magnetron deposition discharge," *Journal of Physics D: Applied Physics*, vol. 40, no. 7, p. 2037, 2007.

[110] S. Karkari, A. Vetushka, and J. Bradley, "Measurement of the plasma potential adjacent to the substrate in a midfrequency bipolar pulsed magnetron," *Journal of Vacuum Science & Technology A: Vacuum, Surfaces, and Films*, vol. 21, no. 6, pp. L28–L32, 2003.

[111] P. Poolcharuansin, B. Liebig, and J. Bradley, "Plasma parameters in a pre-ionized hipims discharge operating at low pressure," *IEEE transactions on plasma science*, vol. 38, no. 11, pp. 3007–3015, 2010.

[112] S. Konstantinidis, J. Dauchot, M. Ganciu, A. Ricard, and M. Hecq, "Influence of pulse duration on the plasma characteristics in high-power pulsed magnetron discharges," *Journal of applied physics*, vol. 99, no. 1, p. 013307, 2006.

[113] T. Nakano, C. Murata, and S. Baba, "Effect of the target bias voltage during off-pulse period on the impulse magnetron sputtering," *Vacuum*, vol. 84, no. 12, pp. 1368–1371, 2010.

[114] I.-L. Velicu, G.-T. Ianoş, C. Porosnicu, I. Mihăilă, I. Burducea, A. Velea, D. Cristea, D. Munteanu, and V. Tiron, "Energy-enhanced deposition of copper thin films by bipolar high power impulse magnetron sputtering," *Surface and Coatings Technology*, vol. 359, pp. 97–107, 2019.

[115] R. P. B. Viloan, U. Helmersson, and D. Lundin, "Copper thin films deposited using different ion acceleration strategies in hipims," *Surface and Coatings Technology*, vol. 422, p. 127487, 2021.

[116] V. Tiron and I. L. Velicu, "Understanding the ion acceleration mechanism in bipolar HiPIMS: The role of the double layer structure developed in the after-glow plasma," *Plasma Sources Science and Technology*, vol. 29, no. 1, 2020.

[117] L. P. Block, "A double layer review," *Astrophysics and Space Science*, vol. 55, no. 1, pp. 59–83, 1978.

[118] C. Charles, "A review of recent laboratory double layer experiments," *Plasma Sources Science and Technology*, vol. 16, no. 4, 2007.

[119] J. Keraudy, R. P. B. Viloan, M. A. Raadu, N. Brenning, D. Lundin, and U. Helmersson, "Bipolar HiPIMS for tailoring ion energies in thin film deposition," *Surface and Coatings Technology*, vol. 359, pp. 433–437, 2 2019.

[120] M. Han, Y. Luo, L. Tang, J. Gu, H. Li, Y. Xu, S. Luo, and L. Li, "Plasma flux and energy enhancement in bp-hipims discharge via auxiliary anode and solenoidal coil," *Plasma Sources Science and Technology*, vol. 30, no. 11, p. 115002, 2021.

[121] M. Han, Y. Luo, L. Li, J. Gu, Y. Xu, and S. Luo, "Optimizing the ion diffusion in bipolar-pulse hipims discharge (bp-hipims) via an auxiliary anode," *Plasma Sources Science and Technology*, vol. 30, no. 9, p. 095016, 2021.

[122] M. Han, Y. Luo, L. Li, H. Li, Y. Xu, and S. Luo, "Ion energy distribution and non-linear ion dynamics in bp-hipims and acbp-hipims discharge," *Plasma Sources Science and Technology*, vol. 31, p. 025016, feb 2022.

[123] Y. Luo, M. Han, Y. Su, H. Li, D. Li, L. Tang, D. Deng, J. Gu, X. Yan, Y. Xu, S. Luo, and L. Li, "Adjustment of high-energy ion flux in bp-hipims via pulsed coil magnetic field: plasma dynamics and film deposition," *Plasma Sources Science and Technology*, vol. 31, p. 095015, oct 2022.

[124] R. Hippler, M. Cada, V. Stranak, and Z. Hubicka, "Time-resolved optical emission spectroscopy of a unipolar and a bipolar pulsed magnetron sputtering discharge in an argon/oxygen gas mixture with a cobalt target," *Plasma Sources Science and Technology*, vol. 28, 11 2019.

[125] R. Hippler, M. Cada, and Z. Hubicka, "Time-resolved diagnostics of a bipolar HiPIMS discharge," *Journal of Applied Physics*, vol. 127, p. 203303, 5 2020.

[126] S. Chauhan, M. Ranjan, M. Bandyopadhyay, and S. Mukherjee, "Droplet shaped anode double layer and electron sheath formation in magnetically constricted anode," *Physics of Plasmas*, vol. 23, no. 1, p. 013502, 2016.

[127] S. Baalrud, N. Hershkowitz, and B. Longmier, "Global nonambipolar flow: Plasma confinement where all electrons are lost to one boundary and all positive ions to another boundary," *Physics of plasmas*, vol. 14, no. 4, p. 042109, 2007.

[128] S. D. Baalrud, B. Scheiner, B. T. Yee, M. M. Hopkins, and E. Barnat, "Interaction of biased electrodes and plasmas: sheaths, double layers, and fireballs," *Plasma Sources Science and Technology*, vol. 29, no. 5, p. 053001, 2020.

[129] F. Avino, A. Sublet, and M. Taborelli, "Evidence of ion energy distribution shift in hipims plasmas with positive pulse," *Plasma Sources Science and Technology*, vol. 28, no. 1, p. 01LT03, 2019.

[130] M. Michiels, T. Godfroid, R. Snyders, and N. Britun, "A poly-diagnostic study of bipolar high-power magnetron sputtering: role of electrical parameters," *Journal of Physics D: Applied Physics*, vol. 53, no. 43, p. 435205, 2020.

[131] M. Michiels, K. Leonova, T. Godfroid, R. Snyders, and N. Britun, "Magnetic field topology for altering ion density in bipolar sputtering," *Applied Physics Letters*, vol. 121, no. 5, p. 051603, 2022.

[132] A. D. Pajdarová, T. Kozák, Z. Hubička, M. Čada, P. Mareš, and J. Čapek, "Plasma parameters in positive voltage pulses of bipolar HiPIMS discharge determined by Langmuir probe with a sub-microsecond time resolution," *Plasma Sources Science and Technology*, vol. 29, 8 2020.

[133] M. Zanáška, D. Lundin, N. Brenning, H. Du, P. Dvořák, P. Vašina, and U. Helmersson, "Dynamics of bipolar hipims discharges by plasma potential probe measurements," *Plasma Sources Science and Technology*, vol. 31, no. 2, p. 025007, 2022.

[134] H. Du, R. Shu, R. Boyd, A. le Febvrier, U. Helmersson, P. Eklund, and D. Lundin, "Evolution of microstructure and properties of tinbcralhfn films grown by unipolar and bipolar high-power impulse magnetron co-sputtering: The role of growth temperature and ion bombardment," *Surface and Coatings Technology*, p. 129389, 2023.

[135] R. Ganesan, I. Fernandez-Martinez, B. Akhavan, D. Matthews, D. Sergachev, M. Stueber, D. McKenzie, and M. Bilek, "Pulse length selection in bipolar hipims for high deposition rate of smooth, hard amorphous carbon films," *Surface and Coatings Technology*, vol. 454, p. 129199, 2023.

[136] J.-F. Tang, Y.-J. Tsai, C.-H. Huang, C.-Y. Lin, F.-C. Yang, J.-J. Hwang, and C.-L. Chang, "Effects of process parameters on optical characteristics of diamond-like carbon thin films deposited using high-power impulse magnetron sputtering," *Thin Solid Films*, vol. 690, p. 137562, 2019.

[137] Š. Batková, J. Čapek, J. Rezek, R. Čerstvỳ, and P. Zeman, "Effect of positive pulse voltage in bipolar reactive hipims on crystal structure, microstructure and mechanical properties of crn films," *Surface and Coatings Technology*, vol. 393, p. 125773, 2020.

[138] V. Tiron, M. A. Ciolan, G. Bulai, D. Cristea, and I.-L. Velicu, "Effect of pulsing configuration and magnetic balance degree on mechanical properties of crn coatings deposited by bipolar-hipims onto floating substrate," *Coatings*, vol. 11, no. 12, p. 1526, 2021.

[139] K. Bobzin, T. Brögelmann, N. Kruppe, G. Eichenhofer, and C. Schulze, "Influence of a short reverse positive hppms pulse on the deposition of craln," *Surface and Coatings Technology*, vol. 423, p. 127625, 2021.

[140] I. Langmuir, "The interaction of electron and positive ion space charges in cathode sheaths," *Physical review*, vol. 33, no. 6, p. 954, 1929.

[141] T. An, R. Merlino, and N. D'Angelo, "Cylindrical anode double layers ('firerods') produced in a uniform magnetic field," *Journal of Physics D: Applied Physics*, vol. 27, no. 9, p. 1906, 1994.

[142] S. Baalrud, B. Longmier, and N. Hershkowitz, "Equilibrium states of anodic double layers," *Plasma Sources Science and Technology*, vol. 18, no. 3, p. 035002, 2009.

[143] E. Ahedo, "Current–voltage response of anodic plasma contactors with external ionization," *Physics of Plasmas*, vol. 3, no. 11, pp. 3875–3884, 1996.

[144] M. Strat, G. Strat, and S. Gurlui, "Basic processes in discharge plasma double layers," *Journal of Physics D: Applied Physics*, vol. 32, no. 1, p. 34, 1999.

[145] M. Sanduloviciu and E. Lozneanu, "On the generation mechanism and the instability properties of anode double layers," *Plasma physics and controlled fusion*, vol. 28, no. 3, p. 585, 1986.

[146] Y.-S. Park, Y. Lee, K.-J. Chung, and Y. Hwang, "Characterization of plasma ion source utilizing anode spot with positively biased electrode for stable and high-current ion beam extraction," *Review of Scientific Instruments*, vol. 82, no. 12, p. 123303, 2011.

[147] A. Barkan and R. Merlino, "Confinement of dust particles in a double layer," *Physics of Plasmas*, vol. 2, no. 9, pp. 3261–3265, 1995.

[148] R. Stenzel, J. Gruenwald, C. Ionita, and R. Schrittwieser, "Pulsating fireballs with high-frequency sheath–plasma instabilities," *Plasma Sources Science and Technology*, vol. 20, no. 4, p. 045017, 2011.

[149] C. Maszl, J. Laimer, and H. Stori, "Observations of self-organized luminous patterns on the anode of a direct-current glow discharge at higher pressures," *IEEE Transactions on Plasma Science*, vol. 39, no. 11, pp. 2118–2119, 2011.

[150] R. L. Merlino, "Understanding langmuir probe current-voltage characteristics," *American Journal of Physics*, vol. 75, no. 12, pp. 1078–1085, 2007.

[151] B. Song, N. d'Angelo, and R. Merlino, "On anode spots, double layers and plasma contactors," *Journal of Physics D: Applied Physics*, vol. 24, no. 10, p. 1789, 1991.

[152] B. Scheiner, E. V. Barnat, S. D. Baalrud, M. M. Hopkins, and B. T. Yee, "Theory and simulation of anode spots in low pressure plasmas," *Physics of Plasmas*, vol. 24, no. 11, p. 113520, 2017.

[153] B. Scheiner, E. V. Barnat, S. D. Baalrud, M. M. Hopkins, and B. T. Yee, "Measurements of fireball onset," *Physics of Plasmas*, vol. 25, no. 4, p. 043513, 2018.

[154] S. Chauhan, T. Barman, M. Bhatnagar, M. Ranjan, and S. Mukherjee, "Plasma fireball: A unique tool to fabricate patterned nanodots," *Review of Scientific Instruments*, vol. 88, no. 6, p. 063507, 2017.

[155] V. Pachchigar, B. Satpati, K. Sooraj, S. Augustine, S. Hans, M. Ranjan, *et al.*, "Plasma fireball-mediated ion implantation for nonvolatile memory application," *Applied Surface Science*, vol. 607, p. 154999, 2023.

[156] V. Stranak, R. Bogdanowicz, S. Drache, M. Cada, Z. Hubicka, and R. Hippler, "Dynamic study of dual high-power impulse magnetron sputtering discharge by optical emission imaging," *IEEE Transactions on Plasma Science*, vol. 39, no. 11, pp. 2454–2455, 2011.

[157] K. Muraoka and A. Kono, "Laser thomson scattering for low-temperature plasmas," *Journal of Physics D: Applied Physics*, vol. 44, no. 4, p. 043001, 2011.

[158] S. Prunty, "A primer on the theory of thomson scattering for high-temperature fusion plasmas," *Physica Scripta*, vol. 89, no. 12, p. 128001, 2014.

[159] J. J. Thomson, *The corpuscular theory of matter*. A. Constable & Company, Limited, 1907.

[160] N. Peacock, D. Robinson, M. Forrest, P. Wilcock, and V. Sannikov, "Measurement of the electron temperature by thomson scattering in tokamak t3," *Nature*, vol. 224, no. 5218, pp. 488–490, 1969.

[161] J. Clark, M. Bowden, and R. Scannell, "Low temperature thomson scattering on mast-u," *Review of Scientific Instruments*, vol. 92, no. 4, p. 043545, 2021.

[162] A. J. Gross and T. R. Herrmann, "History of lasers," *World journal of urology*, vol. 25, no. 3, pp. 217–220, 2007.

[163] T. Sakoda, S. Momii, K. Uchino, K. Muraoka, M. Bowden, M. Maeda, Y. Manabe, M. Kitagawa, and T. Kimura, "Thomson scattering diagnostics of an ecr processing plasma," *Japanese journal of applied physics*, vol. 30, no. 8A, p. L1425, 1991.

[164] J. De Regt, R. Engeln, F. De Groote, J. Van der Mullen, and D. Schram, "Thomson scattering experiments on a 100 mhz inductively coupled plasma calibrated by raman scattering," *Review of scientific instruments*, vol. 66, no. 5, pp. 3228–3233, 1995.

[165] M. Bowden, M. Kogano, Y. Suetome, T. Hori, K. Uchino, and K. Muraoka, "Comparison of electron property measurements in an inductively coupled plasma made

by langmuir probe and laser thomson scattering techniques," *Journal of Vacuum Science & Technology A: Vacuum, Surfaces, and Films*, vol. 17, no. 2, pp. 493–499, 1999.

[166] M. Bowden, Y. Goto, H. Yanaga, P. Howarth, K. Uchino, and K. Muraoka, "A thomson scattering diagnostic system for measurement of electron properties of processing plasmas," *Plasma Sources Science and Technology*, vol. 8, no. 2, p. 203, 1999.

[167] K. Muraoka, K. Uchino, and M. Bowden, "Diagnostics of low-density glow discharge plasmas using thomson scattering," *Plasma physics and controlled fusion*, vol. 40, no. 7, p. 1221, 1998.

[168] E. Carbone, S. Hübner, J. Palomares, and J. Van Der Mullen, "The radial contraction of argon microwave plasmas studied by thomson scattering," *Journal of Physics D: Applied Physics*, vol. 45, no. 34, p. 345203, 2012.

[169] B. H. Seo, S. J. You, and J. H. Kim, "Analysis of uncertainty of electron density and temperature using laser thomson scattering in helicon plasmas," *Japanese Journal of Applied Physics*, vol. 54, no. 8, p. 086102, 2015.

[170] A. Van Gessel, E. Carbone, P. Bruggeman, and J. Van der Mullen, "Laser scattering on an atmospheric pressure plasma jet: disentangling rayleigh, raman and thomson scattering," *Plasma Sources Science and Technology*, vol. 21, no. 1, p. 015003, 2012.

[171] E. Slikboer and J. L. Walsh, "Characterization of a khz sinusoidal argon plasma jet impinging on water using thomson scattering and fast imaging," *Journal of Physics D: Applied Physics*, vol. 54, no. 32, p. 325201, 2021.

[172] E. Carbone and S. Nijdam, "Thomson scattering on non-equilibrium low density plasmas: principles, practice and challenges," *Plasma Physics and Controlled Fusion*, vol. 57, no. 1, p. 014026, 2014.

[173] M. D. Bowden, Y. Goto, T. Uchino, K. Muraoka, and M. Noguchi, "Detection limit of laser thomson scattering for low density discharge plasmas," *Japanese journal of applied physics*, vol. 38, no. 6R, p. 3723, 1999.

[174] M. J. V. de Sande, *Laser scattering on low temperature plasmas*. PhD thesis, Eindhoven University of technology, 2002.

[175] M. Aramaki, J. Kobayashi, A. Kono, E. Stamate, and H. Sugai, "Development of high-efficiency laser thomson scattering measurement system for the investigation of eedf in surface wave plasma," *Thin solid films*, vol. 506, pp. 679–682, 2006.

[176] B. Vincent, S. Tsikata, S. Mazouffre, T. Minea, and J. Fils, "A compact new incoherent thomson scattering diagnostic for low-temperature plasma studies," *Plasma Sources Science and Technology*, vol. 27, p. 055002, may 2018.

[177] J. Sheehan and N. Hershkowitz, "Emissive probes," *Plasma Sources Science and Technology*, vol. 20, no. 6, p. 063001, 2011.

[178] I. Langmuir, "The pressure effect and other phenomena in gaseous discharges," *Journal of the Franklin Institute*, vol. 196, no. 6, pp. 751–762, 1923.

[179] M. Tichy, P. Kudrna, J. Behnke, C. Csambal, and S. Klagge, "Langmuir probe diagnostics for medium pressure and magnetised low-temperature plasma," *Le Journal de Physique IV*, vol. 7, no. C4, pp. C4–397, 1997.

[180] J. Sheehan, Y. Raitses, N. Hershkowitz, and M. McDonald, "Recommended practice for use of emissive probes in electric propulsion testing," *Journal of Propulsion and Power*, vol. 33, no. 3, pp. 614–637, 2017.

[181] J. Sheehan, Y. Raitses, N. Hershkowitz, I. Kaganovich, and N. J. Fisch, "A comparison of emissive probe techniques for electric potential measurements in a complex plasma," *Physics of Plasmas*, vol. 18, no. 7, p. 073501, 2011.

[182] R. F. Kemp and J. Sellen Jr, "Plasma potential measurements by electron emissive probes," *Review of Scientific Instruments*, vol. 37, no. 4, pp. 455–461, 1966.

[183] M. Ye and S. Takamura, "Effect of space-charge limited emission on measurements of plasma potential using emissive probes," *Physics of Plasmas*, vol. 7, no. 8, pp. 3457–3463, 2000.

[184] L. Schwager, "Effects of secondary and thermionic electron emission on the collector and source sheaths of a finite ion temperature plasma using kinetic theory and numerical simulation," *Physics of Fluids B: Plasma Physics*, vol. 5, no. 2, pp. 631–645, 1993.

[185] J. Smith, N. Hershkowitz, and P. Coakley, "Inflection-point method of interpreting emissive probe characteristics," *Review of Scientific Instruments*, vol. 50, no. 2, pp. 210–218, 1979.

[186] N. Mahdizadeh, F. Greiner, M. Ramisch, U. Stroth, W. Guttenfelder, C. Lechte, and K. Rahbarnia, "Comparison of langmuir and emissive probes as diagnostics for turbulence studies in the low-temperature plasma of the torsatron tj-k," *Plasma Physics and Controlled Fusion*, vol. 47, no. 4, p. 569, 2005.

[187] J. Sheffield, D. Froula, S. H. Glenzer, and N. C. Luhmann Jr, *Plasma scattering of electromagnetic radiation: theory and measurement techniques*. Academic press, 2010.

[188] P. J. Ryan, *Electron diagnostics of magnetron discharges*. PhD thesis, The University of Liverpool (United Kingdom), 2019.

[189] D. Evans and J. Katzenstein, "Laser light scattering in laboratory plasmas," *Reports on Progress in Physics*, vol. 32, no. 1, p. 207, 1969.

[190] K. Lee, K. Lee, J. Kim, and T. Lho, "High resolution thomson scattering system for steady-state linear plasma sources," *Review of Scientific Instruments*, vol. 89, no. 1, p. 013508, 2018.

[191] K. Warner and G. M. Hieftje, "Thomson scattering from analytical plasmas," *Spectrochimica Acta Part B: Atomic Spectroscopy*, vol. 57, no. 2, pp. 201–241, 2002.

[192] H.-J. Kunze, "The laser as a tool for plasma diagnostics," in *Plasma Diagnostics* (W. Lochte-Holtgreven, ed.), ch. 9, North-Holland Publishing Company, 1968.

[193] M. N. Shneider, "Ponderomotive perturbations of low density low-temperature plasma under laser thomson scattering diagnostics," *Physics of Plasmas*, vol. 24, no. 10, p. 100701, 2017.

[194] A. T. Powis and M. N. Shneider, "Particle-in-cell modeling of laser thomson scattering in low-density plasmas at elevated laser intensities," *Physics of Plasmas*, vol. 25, no. 5, p. 053513, 2018.

[195] M. Aymar and M. Crance, "Theory of two-and three-photon ionisation of metastable helium atoms," *Journal of Physics B: Atomic and Molecular Physics (1968-1987)*, vol. 13, no. 13, p. 2527, 1980.

[196] A. Kramida, Yu. Ralchenko, J. Reader, and and NIST ASD Team. NIST Atomic Spectra Database (ver. 5.9), [Online]. Available: `https://physics.nist.gov/asd` [2022, September 5]. National Institute of Standards and Technology, Gaithersburg, MD., 2021.

[197] U. Fantz, "Basics of plasma spectroscopy," *Plasma sources science and technology*, vol. 15, no. 4, p. S137, 2006.

[198] M. Smith, *Complex Magnetized Plasmas*. PhD thesis, The University of Liverpool (United Kingdom), 2022.

[199] H. Fujita and S. Yagura, "Measurements of fast time evolutions of plasma potential using emissive probe," *Japanese Journal of Applied Physics*, vol. 22, no. 1R, p. 148, 1983.

[200] J. Bradley, S. Karkari, and A. Vetushka, "A study of the transient plasma potential in a pulsed bi-polar dc magnetron discharge," *Plasma Sources Science and Technology*, vol. 13, no. 2, p. 189, 2004.

[201] B. Liebig, *Invasive and non-invasive diagnostics of high power impulse magnetron sputtering (HiPIMS) discharges*. PhD thesis, University of Liverpool, 2013.

[202] T. Kozák and J. Lazar, "Gas rarefaction in high power impulse magnetron sputtering: comparison of a particle simulation and volume-averaged models," *Plasma Sources Science and Technology*, vol. 27, no. 11, p. 115012, 2018.

[203] J. Hnilica, P. Klein, P. Vašina, R. Snyders, and N. Britun, "Revisiting particle dynamics in hipims discharges. i. general effects," *Journal of Applied Physics*, vol. 128, no. 4, p. 043303, 2020.

[204] L. de Poucques, J.-C. Imbert, C. Boisse-Laporte, J. Bretagne, M. Ganciu, L. Teulé-Gay, and M. Touzeau, "Study of the transport of titanium neutrals and ions in the post-discharge of a high power pulsed magnetron sputtering device," *Plasma Sources Science and Technology*, vol. 15, no. 4, p. 661, 2006.

[205] A. Ehiasarian, A. Vetushka, A. Hecimovic, and S. Konstantinidis, "Ion composition produced by high power impulse magnetron sputtering discharges near the substrate," *Journal of Applied Physics*, vol. 104, no. 8, 2008.

[206] X. Yang and A. Hassanein, "Atomic scale calculations of tungsten surface binding energy and beryllium-induced tungsten sputtering," *Applied Surface Science*, vol. 293, pp. 187–190, 2 2014.

[207] S. Shermukhamedov and M. Probst, "Modelling the impact of argon atoms on a tungsten surface," *The European Physical Journal D*, vol. 76, no. 9, p. 169, 2022.

[208] L. Spitzer, "Physics of fully ionized gases (new york: Interscience publ.)," 1956.

[209] S. Buckman and B. Lohmann, "Low-energy total cross section measurements for electron scattering from helium and argon," *Journal of Physics B: Atomic and Molecular Physics*, vol. 19, no. 16, p. 2547, 1986.

[210] S. Rossnagel and H. Kaufman, "Induced drift currents in circular planar magnetrons," *Journal of Vacuum Science & Technology A: Vacuum, Surfaces, and Films*, vol. 5, no. 1, pp. 88–91, 1987.

[211] N. Brenning, R. Merlino, D. Lundin, M. A. Raadu, and U. Helmersson, "Faster-than-bohm cross-b electron transport in strongly pulsed plasmas," *Physical review letters*, vol. 103, no. 22, p. 225003, 2009.

[212] F. Avino, D. Fonnesu, T. Koettig, M. Bonura, C. Senatore, A. P. Fontenla, A. Sublet, and M. Taborelli, "Improved film density for coatings at grazing angle of incidence in high power impulse magnetron sputtering with positive pulse," *Thin Solid Films*, vol. 706, p. 138058, 2020.

[213] V. Pachchigar, M. Ranjan, and S. Mukherjee, "Role of hierarchical protrusions in water repellent superhydrophobic ptfe surface produced by low energy ion beam irradiation," *Scientific reports*, vol. 9, no. 1, pp. 1–10, 2019.

[214] S. Ashok, H. Kräutle, and H. Beneking, "Effect of argon ion implantation dose on silicon schottky barrier characteristics," *Applied physics letters*, vol. 45, no. 4, pp. 431–433, 1984.